

Challenges in Scientific Data Communication from Low-Mass Interstellar Probes*

DAVID G MESSERSCHMITT,¹ PHILIP LUBIN,² AND IAN MORRISON^{3,4}

¹University of California at Berkeley, Department of Electrical Engineering and Computer Sciences, USA

²University of California at Santa Barbara, Department of Physics, USA

³Swinburne University of Technology, Centre for Astrophysics and Supercomputing, Australia

⁴Now with Curtin University, International Centre for Radio Astronomy Research, Australia

(Received February 2020)

Submitted to ApJ

ABSTRACT

A downlink for the return of scientific data from space probes at interstellar distances is studied. The context is probes moving at relativistic speed using a terrestrial directed-energy beam for propulsion, necessitating very-low mass probes. Achieving simultaneous communication from a swarm of probes launched at regular intervals to a target at the distance of Proxima Centauri is addressed. The analysis focuses on fundamental physical and statistical communication limitations on downlink performance rather than a concrete implementation. Transmission time/distance and probe mass are chosen to achieve the best data latency vs volume tradeoff. Challenges in targeting multiple probe trajectories with a single receiver are addressed, including multiplexing, parallax, and target star proper motion. Relevant sources of background radiation, including cosmic, atmospheric, and receiver dark count are identified and estimated. Direct detection enables high photon efficiency and incoherent aperture combining. A novel burst pulse-position modulation (BPPM) beneficially expands the optical bandwidth and ameliorates receiver dark counts. A canonical receive optical collector combines minimum transmit power with constrained swarm-probe coverage. Theoretical limits on reliable data recovery and sensitivity to the various BPPM model parameters are applied, including a wide range of total collector areas. Significant near-term technological obstacles are identified. Enabling innovations include a high peak-to-average power ratio, a large source extinguishing factor, the shortest atmosphere-transparent wavelength to minimize target star interference, adaptive optics for atmospheric turbulence, very selective bandpass filtering (possibly with multiple passbands), very low dark-count single-photon superconducting detectors, and very accurate attitude control and pointing mechanisms.

Keywords: interstellar space probes, interstellar communication, background radiation

NOMENCLATURE

$X^{\{T,S,R,TR\}}$	Design values of parameter “ X ” at T =transmitter, S =receiver aperture, R =entire receive collector, or TR =end-to-end. S and R correspond to the canonical receive collector defined in §5.
$Y_{\{A,P,N,I,D\}}$	Values of performance metric “ Y ” corresponding to A =average power, P =peak power, N =noise, I =interference, or D =dark counts.
Others	See Tbls.1, 2, 3, and 4 and Tbl.8

1. INTRODUCTION

Since exoplanets are commonplace, interest in and concrete efforts toward the scientific exploration of exo-

planets are growing. This paper addresses the technology development challenges behind the goal of launching low-mass interstellar space probes to the vicinity of the nearest star system (Alpha Centauri) and returning the acquired scientific data before the end of the 21st century. Prominent among the myriad challenges are propulsion and communication. Here we address the communication of scientific data from a probe at interstellar distances and traveling at a relativistic speed.

First proposed by Robert Forward in 1962 (Forward 1962), a low-mass probe with a sail propelled by directed energy from earth is the only known technological option for close exploration of nearby stars that may be accessible with available or near-term technology, and which completes its mission in a matter of decades. This has led to concrete efforts to validate the concept and

* Copyright©2020.

its supporting technology in the context of the NASA StarLight and Breakthrough StarShot programs (Lubin 2016; Kulkarni et al. 2018; Lubin 2020; Parkin 2018).

Such a probe achieves minimum mass (and hence highest velocity) by carrying only a sail for propulsion, scientific instrumentation, a downlink communications system, photon thrusters for attitude control, and an electrical power generator. Coupled with very high power directed energy beaming from earth and a sail that captures the momentum from that beam, it can reach 10-20% of light speed. Following a flyby (likely of Proxima Centauri or other targets within our stellar neighborhood), the probe would transmit the scientific data collected back to a receiver on the earth’s surface, which would consist of a large set of optical apertures with incoherent combining. Location on the earth’s surface (rather than on a space-based platform) is motivated by the large dimensions of the directed-energy and receive infrastructures, and the large energy requirements for the former.

The focus here is on the probe-to-earth communication downlink design with the expectation that any earth-to-probe uplink communication is short-lived and benefits from relative proximity to earth. Relying heavily on a reusable fixed propulsion and communication infrastructure confined to the earth’s surface, a swarm of multiple probes can be launched with a diversity of scientific instruments capturing images, magnetic field strengths, spectroscopy, etc.

We quantify the tradeoff between probe mass, speed and data rate, with the goal of minimizing the data latency, defined as the time from probe launch to the completion of the data download. As the total data volume is increased, the probe mass and latency necessarily increase, and speed decreases. Later numerical results focus on the lowest-mass “wafer scale” version.

Today most interest in interstellar exploration by space probes resides in the astronomy and astrophysics communities, but some essential knowledge and experience lies with the communications sciences. With the goal of informing all these communities and uniting them around this challenge, we are careful to define terminology and emphasize intuitive explanation rather than detailed derivation of theoretical results.

1.1. Goals

As of this writing it is early in the conception of the interstellar mission based on low-mass probes. Our goal *is* to address the physical and statistical communication limitations on a scientific data downlink, as well as their implications for the requisite technological capabilities. Our goal is *not* to propose a concrete and fully specified design for such a communication downlink, nor to address the numerous engineering challenges that will be encountered, as there are too many uncertainties, interactions between launch and downlink communication, and questions about the technologies that

may be available in the timeframe of the first operational downlink. An initial conclusion is that wavelengths in the visible optical regime are appropriate due to the severe probe electrical power and mass restrictions. We propose an architecture that meets operational requirements. Within that architecture we study and quantify the inevitable dependencies and tradeoffs among the different components, and in general attempt to gauge the feasibility of the endeavor.

Because we can use higher power or larger apertures, the laws of physics do not limit the achievable distances or data rates. Rather, practical limitations are due to low probe mass and available technologies and their performance characteristics. Because probes will be launched in a couple decades at the earliest, and the beginning of downlink operation will be delayed for at least five decades (see §2.5), we don’t consider currently available technology to be limiting. Rather we identify the areas of greatest technological challenge, and identify new capabilities that are needed. This mission can leverage general technology advances over the coming decades, but may also require specific technological innovation and development. We also identify and discuss tradeoffs among technologies, and assume that greater advancement in some areas can offset slower advancement in others.

Thus we can identify the specific goals of this paper as:

- Identify the physical limitations on such a mission, especially those related to the space environment (such as unwanted sources of noise and interference).
- Propose a system architecture, within which we identify the system components and quantify needed capabilities.
- Understand the interactions and tradeoffs among those components.
- Identify components where currently available technology is inadequate and estimate the necessary future capabilities. A more concise summary of these technology inadequacies is available (Messerschmitt et al. 2019).
- Generally assess the feasibility of the endeavor in the envisioned timeframe.

Implementation and practice always brings some bad news. While we attempt to anticipate the greatest challenges that will be encountered, we do not attempt to accurately predict an actual deployed system performance. Thus, the results here always fall on the idealistic side. One of the goals of any subsequent technology development will be to come as close to these ideals as possible.

1.2. Related work

Most effort and publication devoted to low-mass probes has emphasized the challenges of propulsion by directed energy and light-sail (Hoang et al. 2017; Heller & Hippke 2017; Heller et al. 2017; Hoang & Loeb 2017; Heller 2017) and (Hoang 2017; Gros 2017; Forgan et al. 2017; Atwater et al. 2018).

In some ways this challenge mirrors the extensively studied requirements for interplanetary spacecraft communication within our solar system (Hemmati 2009). The substantial differences include the severe limitations on the probe’s available electrical power, processing, and transmit optics, as well as the much greater propagation loss, different sources of background radiation, ground-based reception with many issues related to atmospheric turbulence, scattering and weather, and the expectation of a swarm of probe downlinks operating concurrently.

Space communication applications have stimulated extensive research and engineering into long-distance free space optical communication. Results most relevant to the present challenge come from JPL’s interplanetary network (IPN) (Dolinar et al. 2012b). This includes an encouraging laboratory demonstration of high photon efficiency in a communication link with insignificant background radiation (Farr et al. 2013).

Interstellar communication differs from terrestrial communication in its emphasis on energy efficiency rather than spectral efficiency. At radio wavelengths, energy-efficient interstellar communication has been studied in the context of METI/SETI (Messerschmitt 2013, 2015). What is different about space probes is the feasibility of transmitter-receiver coordination in the interest of achieving high photon efficiencies to help overcome power/size/mass limitations.

The germane sources of optical-wavelength background radiation for interstellar communication are a current area of research (Lubin 2020). These background calculations have been independently quantified in (Hippke 2019), which quantifies the ultimate quantum limits on communication. The present paper addresses what is achievable in practice with existing or foreseeable technologies.

Here we explore a probe-swarm or single-probe receiver that achieves the minimum transmit power-area product in the interest of minimizing probe mass by operating near the physical limits of the received-signal noise floor. We also explore the implications of varying collector area over a wide range. A recent paper (Parkin 2019) addresses the same application but addresses only the single probe case (requiring complete receiver duplication for each probe in a swarm) and focuses on minimizing receive collector area rather than probe mass (see §10.5.1).

2. SCIENTIFIC MISSION

The low-mass probe mission comprises the science objectives and how they are achieved by a swarm of low-

Table 1. Scientific mission parameters

	Description	Value
\mathcal{R}_0	Nominal data rate for scientific data immediately following encounter during non-outage periods (b/s)	1.
R_a	R_0 reduced to account for outages (b/s)	0.432
\mathcal{V}	Volume of total data (Mb)	28.9
L	Volume of data segment (Mb)	1.0
P_c	Probability of correct segment recovery	0.99
T_L	Latency of total data return (yr)	28.
J_p	Probes transmitting concurrently	26

mass probes, each supporting an individual downlink to return scientific data by that probe to earth.

2.1. Numerical parameters

The set of parameters directly related to the science mission are listed in Tbl.1. Assumed numerical parameters in this and the subsequent parameter and performance metric tables are merely reference points and do *not* carry the weight of design objectives. This would be premature, as there are many design and technology issues and interactions among various system components that will weigh heavily on the final design. Consonant with our goals (see §1.1) these choices serve to gauge the realism (or lack thereof) of the system design using an idealized model that ignores many practical challenges that will undoubtedly arise. More importantly, scaling relationships that follow from varying these parameters are studied (both theoretically and numerically) to appreciate the implications of changing assumptions (see §10).

2.2. Scientific objective

Each individual low-mass probe carries one or more scientific instruments to gather relevant scientific information in the vicinity of the target star. Given the severe mass-power objective, each probe may carry only a single instrument.

Individual probes may carry different types of scientific instrumentation, subject to severe mass limitations. The primary relevance of the scientific objective to the downlink design is the total data volume \mathcal{V} to be downloaded¹ and the reliability with which that data is recovered. These two parameters are certainly related to the type of instrumentation carried by a probe. Early missions are likely to emphasize imaging, so this is the application addressed in our examples. An additional parameter of importance to scientists is the data latency T_L , which is the time elapsed from probe launch to the return of data volume \mathcal{V} in its entirety.

¹ We measure \mathcal{V} in bits (b) rather than bytes (B). For example, 10^6 bits (1 Mb) equals 125 kilobytes (125 kB).

For purposes of reliability, scientific data can be divided into *segments*, each with volume L . It is the reliability of recovery of each segment at the receiver that is of greatest interest. For example, for an imaging mission a segment would be one image (2-D representation in terms of matrix of pixels), and we assume $L = 1$ Mb.² A segment is either recovered correctly in its entirety or corrupted in some fashion due to one or more bit errors.³ P_c is the probability that each individual segment is recovered correctly in its entirety.

2.3. Scientific data rate

The volume \mathcal{V} and latency T_L in Tbl.1 are indirectly related to the scientific data rate \mathcal{R} . \mathcal{R} actually decreases as the square of distance (see §10.3), so \mathcal{R}_0 is the initial (highest) value of \mathcal{R} immediately following encounter. In addition, outages due to atmospheric effects reduce the effective data rate to $\mathcal{R}_a < \mathcal{R}_0$ (see §11.4), and \mathcal{R}_a is used in calculating \mathcal{V} .

2.4. A swarm of probes

The project budget will be heavily concentrated in the terrestrial launch and communication infrastructure. The incremental cost of each probe launch is insignificant in comparison (Parkin 2018), suggesting the repeated launching of probes. Such a swarm of probes can increase the scientific return by following different trajectories near the target star, providing redundancy to account for navigational errors or other sources of failure on individual probes, and enabling a diversity of scientific instruments while accommodating a tight power/mass budget.

Because the cost of the receiver system is likely to be large, our primary analysis focuses on a single receiver that is shared among all the concurrent downlinks. Thus the relevant parameter is not the total number of probes launched, but rather the number of probes J_p for which downlink data transmission is concurrent from the receiver perspective. The specific values of J_p and T_L illustrated are based on the minimization of T_L from each probe for a given \mathcal{V} and a specific launch schedule (see §7).

Concurrent data reception causes serious complications in the design and operation of the terrestrial receiver infrastructure and is a major concern addressed in the following (see §4.1). To minimize this challenge, we don't expect the downlinks to operate during the transit period. Dedication of a receiver to a single downlink (or multiple receivers, one for each downlink as in (Parkin 2019)) is a special case that falls within the scope of our analysis.

² This will accommodate a 1000×1000 set of pixels at one bit per pixel following compression.

³ After compression, even a single bit in error often propagates across the image and thus has serious consequences.

Table 2. Probe transmitter parameters

	Description	Value
ζ	Probe mass ratio	1.
u_0	Probe speed (c)	0.2
$D_{\{0,1\}}$	{Start,end} of downlink propagation distance (ly)	{4.24,4.66}
A_e^T	Effective transmit aperture area (cm ²)	100
F_x	Optical source extinction ratio	10 ⁻⁷

2.5. Timeline

Some significant technology advances are needed to approach the performance metrics envisioned in §10. It is fortunate that there is considerable time available to benefit from the ongoing evolution of technology. There is also the opportunity to target certain technologies for faster advances targeted on the needs of this application and interstellar exploration more generally. Transmitter technologies must be finalized before the first launch (perhaps 1-3 decades). While an operational receiver deployed not long thereafter could have benefits, delaying the download of scientific data until 25+ years following the first launch is an option. Thus for the receiver we have available at least 4-5 decades of technology advancement and development, although there should be a high confidence in the technical feasibility and budget availability prior to the first probe launch.

3. PROBE TRANSMITTER

The communications transmitter is integrally related to other functional units in the probe, such as electric power generation and navigation and pointing control. We assume transmitter parameters as listed in Tbl.2.

3.1. Launch and propulsion

The data latency T_L is the sum of the transit time to the target star, the duration of the downlink transmission, and the signal propagation time from the farthest reaches of transmission (see §C). Minimizing T_L subject to a constraint on \mathcal{V} is a principled approach to determining the best choice of probe mass (see §7). The smallest mass option ($\zeta=1$) is assumed, with increases in transmit power and transmit aperture area possible when ζ is increased (see §7).

The goal of acquiring scientific data from instrumentation in proximity to even nearby stars within the 21st century requires a probe speed u_0 that is a significant fraction of the speed of light c (Manchester & Loeb 2017; Parkin 2018). For example, the distance to the nearest star (Proxima Centauri) is 4.24 ly, and the probe transit time at $u_0=0.2c$ is 21.2 yr. If a probe transmits data beginning immediately after encounter with that star and its exoplanets, the data would begin to reach earth 25.44 years after launch.

Other transmit parameters include the propagation distance $D_{\{0,1\}}$, which is determined by the probe speed u_0 , the data volume \mathcal{V} , and the initial scientific data rate \mathcal{R}_0 . The transmit aperture effective area A_e is a measure of the transmission power-to-flux efficiency (see §B), and equals the geometric area in the diffraction limit. The transmit aperture is assumed to be standalone and relatively small in deference to the low mass requirement. Other proposals assume the much larger probe sail area is exploited as a transmit aperture (Parkin 2019). Finally the extinction ratio F_x is a measure of the spurious power from the transmit laser in its “off” state relative to its “on” state (see §10.7).

3.2. Optical modulation

Scientific payload data is embedded in the transmitted optical signal power vs. time by the modulation. We propose *burst pulse-position modulation* (BPPM), which can achieve the required efficiency while compatible with the imposed constraints (see §6.2).

In BPPM a semiconductor laser in the transmitter generates short pulses of light intensity with a duration on the order of 0.1 to 1 μ s with a repetition rate of about 1-2 Hz. Scientific data is supplemented by error-correction redundancy and then imposed on the pulses by adjusting their timing (see §6.2 and §14). The average power is P_A^T , on the order of 1–100 mW, with a peak transmitted power P_P^T that is about 10^6 larger.⁴ The intensity-modulated light is emitted in the direction of earth by a transmit aperture with effective area A_e^T (see §B). Accurate attitude control based on photon thrusters is necessary to ensure that the earth-based receive collector is illuminated with the maximum power (see §12.6).

The probe incorporates processing to compress scientific data and perform the coding side of error-correction coding (ECC, see §14.3). In addition, it performs data interleaving and adds additional redundancy to counter outages resulting from daylight and weather events (and possibly other sources) at the earth-side receiver (see §14.4).

The probe-to-earth distance increases up to 10% during the operation of the downlink, which may last from 2–9 yr (see §7). Accommodation of increasing propagation distance requires the data rate \mathcal{R} to be reduced by slowing the rate of transmitted pulses and increasing the peak transmitted power (by a maximum of about 20%) to maintain fixed average power.

4. TERRESTRIAL RECEIVER

A terrestrial receiver is assumed, with the parameters chosen for receiver operation as listed in Tbl.3 for two cases: a swarm of probes and a single probe. The choice

⁴ This description is oversimplified, as achieving a P_P^T this large will require a more complicated optical arrangement (see §13.1).

Table 3. Terrestrial receiver parameters

Description		Swarm	Single
λ_0^R	Received optical wavelength (nm)	400	
Ω_A	Coverage solid angle (arcsec ²)	10.	0.01
A_e^S	Effective aperture area (cm ²)	6.8	6807.
P_W	Probability of weather outage	0.1	
P_D	Probability of daylight outage	0.52	
η	Optical detector efficiency	1.0	
BPP	Non-outage photon efficiency (b/ph)	10.9	
SBR	Average signal to average background photons during non-outage PPM frames	4	
F_c	Coronagraph rejection	0.01	

of a visible optical wavelength λ_0^R is based on aperture area considerations (see §8), and is chosen close to the shortest wavelength for which the atmosphere is transparent because this minimizes radiation from the target star (see §10.9.3).

4.1. Trajectories and coverage

The role of a receive optical collector is to convert incident optical power to photon detection events. It can be thought of as a single-pixel optical telescope which does not attempt to image the swarm of probes (since their trajectories are similar) but rather captures a superposition of their signals as they reach the earth.

The coverage of a collector is defined as the solid angle Ω_A over which transmitted probe signals are recovered with nearly equal sensitivity.⁵ To accommodate a swarm of probes with a single receiver, Ω_A has to be considerably larger than it would be for a single probe. The collector is composed of a large number of individual apertures whose photon detections are combined incoherently. The coverage of the collector equals the coverage of the apertures and is related to the effective area A_e^S of the collector’s constituent apertures (see §5). An increase in Ω_A results in an inevitable decrease in receiver sensitivity, which is quantified by a decrease in A_e^S (see §5).

The trajectories of different probes in a swarm are illustrated in a simplified schematic 2-D form in Fig.1. There are five phases to each individual probe mission: launch of the probe, transit to the neighborhood of the target star, encounter with that star (observations and scientific data collection), downlink operation (transmission of that scientific data to earth), and finally permanent probe silence.

⁵ Coverage is similar to the field-of-view of a single-pixel optical telescope, or the resolution of a single pixel in a multiple-pixel imaging telescope. In contrast to optical telescopes, the coverage that results from the beamforming of an optical phased array can be non-circular in shape.

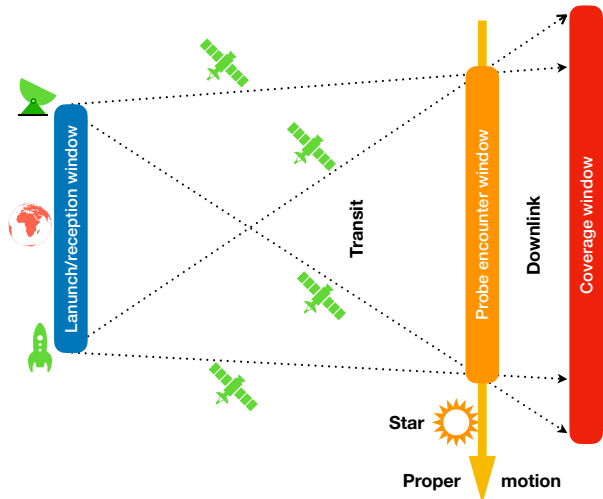


Figure 1. A 2-D schematic representation of the 4 most extreme probe trajectories as viewed from earth. The launch/reception window captures the seasonal variation in earth’s position, and the probe encounter window captures the proper motion of the target star. As shown all encounters are assumed to fall on the same side of the target star, which moves away from the encounter positions. Downlink operation follows encounter. Receiver coverage is assumed to cover all concurrently-transmitting probes, and a coronagraph function takes advantage of spatial separation to reject a portion of the target star’s radiation.

Shown specifically are four probe trajectories at the most extreme angles, taking into account orbital differences between launch and reception coordinates as well as the proper motion of the target star (both of which are exaggerated in scale). Of greatest concern for receiver design are the relative variations in the positions of the different probes and the target star, which determine the required spatial coverage of the receiver and the coronagraph rejection (see §5.2). There are two primary influences:

- A single probe’s apparent position varies due to the parallax effect of the earth’s orbital motion.
- The target star’s proper motion (movement in relation to the galactic background) implies that different probe encounters are spatially separated (Parkin 2019). These probe encounter positions trail behind the moving star, resembling the tail of a comet.

4.2. Source of electric power

A probe launched with directed energy and cruising at constant speed following launch requires no propulsion. Electrical power is nevertheless necessary for probe attitude control, scientific instruments, and downlink com-

munications (Landis 2019). Examples of power sources include a radioisotope thermoelectric generator (RTG) or forward-edge ISM proton-impact conversion during the cruise phase (before and after encounter) with the possible addition of photovoltaic power from the target star during the encounter. At relativistic speeds the latter will be short-lived (on the order of hours), but may be valuable for scientific instruments, as well as the processing for data compression, outage mitigation (see §14.4) and error-control coding (see §14.3).

The available electrical power limits the available transmit optical power. Here we make no prior assumption about transmit power, but rather characterize the minimum transmit power necessary subject to the other constraints, and emphasize the tradeoff between transmit power and total area of the transmit aperture and receive collector.

4.3. Heterodyne vs direct detection

There are two common ways to detect the optical signal from a probe in the receiver. *Heterodyne* mixes that optical signal with a local oscillator (LO), and optical square-law detection results in components of sum and difference frequencies as well as amplification. The difference-frequency component can fall at a microwave wavelength. Here we adopt (for reasons explained in §4.5) the alternative of *direct detection*, which eliminates the LO and relies on single-photon counting detectors. A significant advantage is the reliance of direct detection on intensity (and not phase) modulation at the source, obviating any need for coherence across the apertures comprising the collector (see §5.1).

Heterodyne would offer some compelling advantages. In addition to signal amplification as a part of optical detection, channel separation and bandpass filtering can be performed using available microwave technologies. It also opens up a wider class of modulation schemes based on the phase as well as magnitude of the incident wavefront.

At optical wavelengths (where the energy per photon is significantly higher) individual photons can be directly detected, although due to quantum effects the number of photons detected per unit time is only stochastically related to the receive power. The result is signal self-noise (sometimes called *shot noise* or *quantum noise*).

4.4. Background radiation

Photon counts originating from sources other than shot noise are lumped into the category of background radiation. For a given transmit power and transmit/receive apertures, the initial data rate \mathcal{R}_0 that can be achieved consonant with a sufficiently high signal-to-background ratio (SBR) is limited by the sources of background radiation. No matter how large SBR, signal shot noise remains as a limitation on the reliability with which the scientific data can be recovered (see §14).

Four distinct types of background radiation can be identified.⁶

- Imperfect *laser extinction* at the transmitter during intervals where zero power is sought will result in unwanted photon counts at the receiver (see §13.1).
- *Noise* is radiation that cannot be separated from the data signal because of its time, wavelength, and spatial overlap. In the current application such radiation is broadband, and must be reduced by limiting the optical bandwidth. Significant sources of noise are the cosmic background radiation, the deep star field, zodiacal radiation, and scattered sunlight and moonlight from the earth's atmosphere.
- *Interference* is unwanted radiation which is distinguishable from the data signal in one or more physical parameters (time, wavelength, or spatial) and can therefore be partially or wholly rejected by technological means. The major interference considered here is radiation from the target star, which is spatially separated from the probes, but which may be challenging to reject because of its close proximity to the probe trajectories. The coronagraph function in the receiver can partially reject this interference due to its spatial separation. We assume the rejection factor is F_c relative to the signal originating from the probe.
- *Dark counts* mimic detection of photons originating from sky or cosmic sources, but originate within the receiver and would be present even if all incident light radiation were blocked from the receiver.

Incomplete extinguishment and dark counts generally cannot be limited by bandpass filtering (with the exception of black body radiation in the optics). Numerical calculations suggest that operation during periods of sunlight is not feasible, and with that assumption interference, scattered moonlight, and dark counts are the limiting factors placing a lower bound on the probe's transmit power (see §10.9).

4.5. High photon efficiency

One motivation for adopting direct detection is the higher photon efficiency that can be achieved, which results in a reduction in the total collector area. This is of practical significance because a collector will likely be kilometer-scale. If the rate at which data is reliably recovered is \mathcal{R}_0 b/s and the signal average photon rate is

Λ_A^R ph/s, photon efficiency BPP (in b/ph) is defined by

$$\mathcal{R}_0 = \text{BPP} \cdot \Lambda_A^R. \quad (1)$$

Due to excess shot-noise introduced by the high-power LO, heterodyne cannot achieve a comparable BPP to direct detection. The theoretical limit is $\text{BPP} < \eta / \log 2 = 1.44\eta$ b/ph for detector quantum efficiency η consistent with reliable data recovery (Gordon 1962), while direct detection imposes no theoretical limit. The assumption in Tbl.3 is $\text{BPP}=10.9$ b/ph. This is consistent with a laboratory demonstration of $\text{BPP} = 13$ b/ph (Farr et al. 2013). The significant photon efficiency advantage of direct detection makes it worthwhile to overcome the technological challenges it introduces, which is our focus here.

4.6. Signal-to-background ratio (SBR)

SBR at the receive collector output is $\Lambda_A^R / \Lambda_B^R$, where Λ_A^R is the average rate of signal photons and Λ_B^R is the accumulated average photon rate for all sources of background radiation. Our goal is to achieve an SBR sufficiently large that background radiation has limited impact on data reliability. The impact of SBR is measured by the theoretical effect on BPP (see §E). With the goal of limiting background to a minor impact we choose $\text{SBR}=4$ in Tbl.3. This results in a 5% reduction in the theoretically obtainable BPP as compared to $\text{SBR}=\infty$. Achieving a specific SBR places a lower limit $\Lambda_A^R > \Lambda_B^R \cdot \text{SBR}$ on the received signal average photon rate Λ_A^R , and hence a lower bound on average transmit power P_A^T .

5. RECEIVER PHOTON COLLECTION

The major element of the receiver is the collector, which is similar to a single-pixel optical telescope. It consists of a large number of apertures, each with a dedicated optical detector that responds to individual photons from the incident radiation (background as well as signal) and introduces spurious dark counts as well (see §5.1). Thus no coordination or optical phasing of apertures is necessary. It would be advantageous to share optical detectors over multiple apertures if optical interference can be avoided (see §5.4). In contrast to an optical telescope, the optical path includes a highly selective optical bandpass filter that eliminates most out-of-band background radiation (see §13.2), and may serve to separate the signals from the individual probes as well (see §12.2.2). Photon detection events are logged at the individual apertures, accumulated over a network, and a post-processing stage interprets the totality of photon events to reliably recover the scientific data. This canonical receive collector is now described in greater detail.

5.1. Canonical receive collector

The receive collector in a direct-detection receiver includes the optics and photonics necessary to capture the

⁶ These are terms commonly used in the communications literature. We adopt them here because (a) they are descriptive of these types of impairments and (b) because design techniques are adopted from the communication literature.

power of an incoming electromagnetic wave and convert it to a digital representation of individual photon detection events. The receive collector will be quite large, and is thus a major capital and operational cost.

The receive collector must meet some challenging requirements:

- Accurate pointing toward the target star and swarm of probes has to be maintained in the face of earth orbital dynamics and atmospheric refraction.
- Both the total geometric size (physical dimensions) and total collection area are large as required to achieve a receiver sensitivity that accommodates severe limitations on the probe due to its mass restriction; namely, transmit power and transmit aperture size. A distinction between size and area is needed because the receive collector is not likely to be a single filled optical aperture.
- Achieve a coverage solid angle Ω_A which is relatively large (but no larger than necessary) and has an atypical elongated shape in the direction of the target star's proper motion (see §4.1).
- It will likely incorporate adaptive optics to compensate for atmospheric seeing conditions (see §11).
- Separation of signals from different probes in the optical domain is required for some approaches to multiplexing signals from different probes, such as WDM (see §12.2.2).
- Whatever means possible should limit the background radiation. This includes optical bandpass filtering (see §13.2), rejection of interference with coronagraph functionality (see §12.7), and modulation design to limit dark counts (see §6.2).

5.2. Apertures

A large size (kilometer scale) of the receive optical collector as a whole is required to achieve low transmit power with adequate signal level to counter shot noise. If such a collector were single mode (a single optical detector) and diffraction-limited, not only would its coverage solid angle Ω_A be too small to cover a swarm of probes, but adequate pointing accuracy to track a single probe would be practically unrealizable.

These challenges and the principles of antenna design suggest a canonical receive optical collector architecture illustrated in Fig.2. The entire collector must be decomposed into a large number N^S of smaller apertures. Each aperture is required to achieve all the objectives of the receive array as a whole except a sufficient photon rate to support the desired data rate. In particular, the aperture accurately points at the coverage window as pictured in Fig.1, achieves the desired Ω_A , and

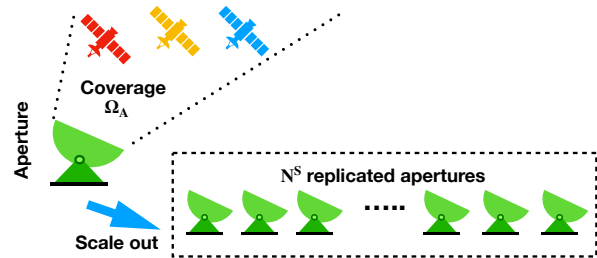


Figure 2. The receive optical collector is composed as an N^S -way replication (called scaling out) of the aperture. An individual aperture focuses on achieving the maximum and uniform sensitivity to the signals from all probes in a swarm across a coverage solid angle Ω_A , and has effective area A_e^S . It is also responsible for achieving a sufficiently large SBR to achieve the target BPP, and may also be responsible for separating the signals from different probes. The N^S apertures independently capture and log photon detection events, with their only coordination a common clock for time stamps. The resulting incoherent accumulation of the incident optical power across the entire collector achieves a sufficient average photon detection rate Λ_A^R to recover the scientific data at rate \mathcal{R} , while influencing neither the coverage nor SBR.

achieves a required SBR. Alternatives to this architecture can be explored, such as abandoning the single-mode diffraction-limited constraint on an aperture. For example, with a conventional optical telescope, photons in individual pixels containing probe trajectories can be counted.

Photon counts accumulate incoherently across apertures. Since photon counts for both the probe signal and the various sources of background accumulate by a factor of N^S , SBR remains fixed independent of N^S . The value of N^S is chosen to achieve the desired signal photon rate commensurate with the desired rate \mathcal{R}_0 commensurate with (1). Aperture replication by N^S is called a *scale out* because the photon counts increase linearly with N^S .⁷

Each aperture (which may or may not be further decomposed into a phased array of elements as described shortly) may have a dedicated optical detector responsible for generating a single stream of photon detection events in response to the incident electromagnetic radiation.

Aperture sensitivity is quantified by its equivalent area A_e^S (defined as the ratio of the intensity of an incident plane wave to detected power). This determines the required transmit power in the probe and the order N^S

⁷ ‘Scale out’ is an engineering term referring to an $N^S \times$ replication with a performance that increases proportionally to N^S . In this case ‘performance’ is measured by the overall sensitivity of the receiver while maintaining fixed coverage and SBR.

of scale-out. Although we like a larger A_e^S , in fact it is predetermined by the relationship between A_e^S and coverage Ω_A .⁸ In §B this relationship is determined in (B6) to be $A_e^S \propto \Omega_A^{-1}$. Larger coverage, as dictated by our requirement to service a swarm of probes with a common receiver, implies reduced sensitivity.

Each aperture is responsible for limiting noise and interference via an optical bandpass filter (see §13.2) and coronagraph functionality (see §12.7). Accounting for a non-ideal filter, define the *effective bandwidth* W_e of a bandpass filter as the ratio of output power to input power spectral density (assumed to be constant). If the transfer function is $H(f)$, then

$$W_e = \int_0^\infty |H(f)|^2 df, \quad (2)$$

in which case $W_e = W$ for an ideal bandpass filter with bandwidth W . More generally $P \cdot W_e$ is the filter output power for a constant spectral density input P . The dark count rate for its optical detector should be as small as technology allows (see §13.3). The coronagraph partially rejects interference from the target star by exploiting its small angular separation from the probe trajectories.

Within the context of a specific aperture design, including particularly sensitivity, coverage, coronagraph rejection, and dark count rates, the probes are responsible for a sufficiently large power-area metric $\xi_A^T = P_A^T A_e^T$ and pointing accuracy to achieve the desired SBR (see §10.1). There is thus a tradeoff between P_A^T and transmit aperture effective area A_e^T .

5.2.1. Aperture scale out

Since the receive optical collector as a whole has $N^S \gg 1$ apertures that are incoherently combined, it is not an antenna in the sense of §B and thus the concept of effective area A_e^R does not apply. Instead we use *total effective area* metric $N^S A_e^S$. This metric gives us a sense of the total geometric area of the entire collector.

While the numerical values of N^S are large, the total collector area $A_e^S N^S$ is a more significant indicator of capital costs. For example it would be attractive to combine apertures into larger assemblages with joint fabrication. Optics similar to that used in smart phone technology can be fabricated in substantial assemblies, and it may also be possible to share a single optical detector over multiple apertures (if optical interference, which would modify the coverage, can be avoided, see §5.4).

⁸ Each aperture qualifies as an ‘antenna’ that is subject to the theory of §B assuming it is single mode (has a single optical detector) and diffraction-limited. This sensitivity-coverage relationship is based on the simplifying assumption (which can be approximated in practice) that the sensitivity is uniform over solid angle Ω_A and zero elsewhere.

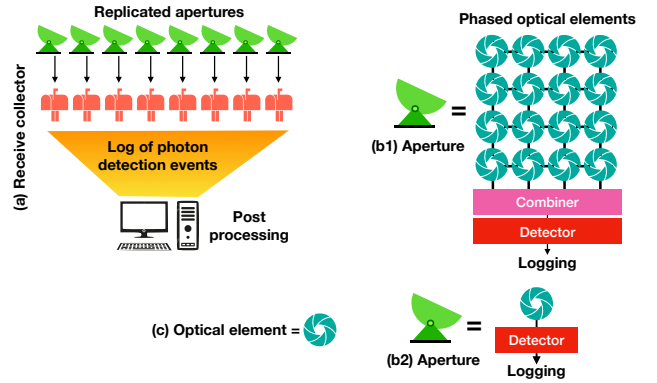


Figure 3. A schematic of a two-level receive optical collector decomposition. (a) The replicated apertures independently log photon detection events, and in a post-processing stage the aggregate events are processed to recover the scientific data originating from multiple probes. (b1) Each aperture is composed of a set of phased elements with a combiner including precision phase shifts feeding a single optical detector. (b2) A degenerate case is an aperture comprised of a single element. (c) Each element is an optical element (composed of lenses, reflectors or thin films).

5.3. Post processing

A more detailed picture of scale out as well as aperture decomposition into smaller elements is shown in Fig.3. Each aperture not only detects individual photons, but it logs those photon-detection events as a time-stamp and, if the aperture performs de-multiplexing, a probe identifier. There being no need for real-time processing of these events, they can be shared in a common post-processing stage in which timing recovery is performed followed by scientific data extraction from the photon events. A permanent stored log of photon events (probe-number and time-stamps) also constitutes the permanent scientific record of a swarm of probe missions.

The collection of apertures operate independently. There is no attempt to align the phases among individual apertures; indeed, the apertures each have their own optical detector which captures the power of the incident radiation to that aperture, so all phase information has been deliberately discarded. This arrangement is colloquially called ‘photon buckets’. The relative placement of apertures is somewhat flexible, allowing for geographic distribution and relative placement for the convenience of construction or maintenance. Atmospheric turbulence is not an issue except at the aperture level (see §11.3). Placement of apertures divided among a set of one or more independent space platforms is also an intriguing possibility.

The apertures all connect to a communication network for distribution of target coordinates (which change at a slow rate), consolidation of photon events for process-

ing, and status updates. The total number of events to be logged across all apertures is of order 0.1 per second per probe for the parameters of Tbl.2 and Tbl.3, so the storage and communication requirements are readily achieved.

The synchronization of time stamps across apertures must be maintained, and this requires a common time reference (Messerschmitt 2017). Synchrony with the multiple probe clocks must also be maintained, all this with an accuracy related to the time-slot T_s (see §12.3).

5.4. Shared optical detectors

One troublesome feature of Fig.3 is the N^S -way duplication of optical detectors, which multiplies the dark count rate by the same factor and imposes a very strict requirement on individual detector dark counts. Sharing of a single optical detector over multiple apertures would reduce the overall dark count rate, as well as reduce the cost and complexity of the scale-out function. However to avoid any impact on the coverage pattern of the overall receive array, any interference in the optical domain among aperture signals would have to be avoided (see §13.3).

5.5. Summary

The two-level hierarchy of apertures combined with scale out to a full aperture is required to *simultaneously* achieve a desired (non-zero) coverage Ω_A , a desired SBR, and a desired sensitivity (signal photon rate Λ_A^R).⁹ The consequence of covering multiple probes with a single receiver is inevitably a larger Ω_A and hence a higher $P_A^T A_e^T$ product for each probe. A desirable feature of the canonical receive aperture is that the difficult technological challenges are confined to the aperture realization, while the large number N^S of apertures is primarily a budgetary and operational issue.

5.6. Phased elements

The canonical receive aperture of Fig.3 anticipates that the apertures are themselves composed of phased elements. Each element is envisioned as an (ideally) diffraction-limited monolithic optical element, which may be constructed from a lens or reflector. Following a combiner, these elements share an optical detector. Within the combiner the magnitude and phase for each element optical signal as it arrives at the detector must be precisely controlled. The relatively small effective area A_e^S of the aperture make this technically feasible, and indeed for the values in Tbl.3 it may not even be necessary. Depending on the aperture dimensions an adaptive-optics component to compensate for atmospheric turbulence may be needed (see §11).

⁹ If as in (Parkin 2019) there were a single probe and pointing accuracy is not a consideration, the coverage could be as small as needed to achieve sufficient sensitivity.

Table 4. Burst-mode pulse-position modulation parameters

	Description	Value
m	Bits per PPM frame	12
$M = 2^m$	Slots per PPM frame	4096
T_s	PPM slot duration (μ s)	0.1
W_e	Effective optical bandwidth (MHz)	10.
T_F	PPM frame duration (ms)	0.41
T_I	Inter-PPM-frame interval (s)	2.2
δ	BPPM duty cycle	$1.9 \cdot 10^{-4}$
PAR	Peak-to-average ratio	4096.

There are several requirements that suggest the use of a phased element: A coverage pattern with solid angle Ω_A that may be non-circular in shape, a coronagraph function which realizes a null in the overall sensitivity pattern at the angle of the interfering target star, and adaptive optics.

6. TRANSMIT MODULATION AND RECEIVE OPTICAL PROCESSING

The optical modulation and associated receive processing are now described. A specific modulation coding technique called burst-mode pulse-position (BPPM) modulation technique is adopted. The parameters of this technique are listed in Tbl.4.

6.1. High photon efficiency and peak power

There are two impairments that limit the photon efficiency BPP that can be achieved. The first is background radiation, the impact of which is limited by placing a theoretical lower bound on SBR (see §E). The quantum efficiency η of the entire optical path reduces signal, noise, and interference equally, but does not affect the rate of dark counts. Thus its effect on SBR is only through the dark count component of background, and $\eta < 1$ renders dark counts relatively more important. Because the η achievable decades from now is uncertain, our nominal assumption is $\eta=1$ together with a sensitivity analysis.

Once background radiation is rendered insignificant, signal shot noise determines a theoretical upper bound on BPP. High BPP with reliable data recovery is achieved by judicious choice of the mapping from scientific data to light intensity vs time in the transmitter (see §6.2) and error-correction coding (see §14.3). Regardless of how these are structured, there is a theoretical limit on the shot-noise-limited BPP that can be achieved in conjunction with reliable recovery of the scientific data. For large SBR this limit is

$$\text{BPP} < \log_2 \text{PAR}, \quad (3)$$

where PAR is the peak-to-average power ratio (see §E). Thus to achieve BPP=10.9 in Tbl.3 we must have, at minimum, $\text{PAR} > 2^{10.9} = 1911$.

High PAR is beneficial to photon efficiency, but it does have implications for the peak transmit power P_P^T required in the transmitter (see §13.1). A high peak power also requires short-term energy storage and possibly voltage conversion in the probe, since electric power is likely to be generated continuously (see §4.2).

PAR and optical bandwidth W_e are related in a subtle but significant way. A larger PAR is inevitably associated with a larger W_e , since it requires relatively high-energy pulses with short duration and low duty cycle. A larger W_e is beneficial in reducing the required selectivity of the receive optical bandpass filters. A larger W_e would also appear to admit more background SBR, thereby decreasing SBR. This is not entirely the case as now shown.

6.2. Burst pulse-position modulation (BPPM)

The modulation has a major influence on photon efficiency. For the purposes of our design exploration we have chosen a novel burst pulse-position modulation (BPPM). The structure of the intensity-modulated signal is defined in Fig.4. The signal is divided into *PPM frames*, each with *frame duration* T_F . Frames are typically interspersed with *blank intervals*, during which no optical power is transmitted. The total time interval between the beginning of successive frames is the *frame interval time* T_I .

Within each frame, the signal is structured as exactly one pulse of light, which may occur in one of $M = 2^m$ short time intervals called *slots*, each with *slot duration* T_s , so that $T_F = MT_s$. This internal frame structure is called *pulse-position modulation* (PPM). PPM is commonly used in optical communications because it trades greater bandwidth (often an ample resource) for improved energy efficiency. However, it is typically used in the conventional PPM configuration in which blank intervals are omitted. Slot time T_s is substantially reduced in BPPM without changing M or T_I and thus without any effect on data rate.

The disadvantage of BPPM over conventional PPM is an increase in peak transmit power (due to the reduction in T_s) P_P^T .¹⁰ However, this is offset by some significant advantages:

- Optical dark counts originating as blackbody radiation in the optical path and in the optical detector are a major issue due to the potentially large number N^S of optical subsystems and optical detectors. The impact of dark counts in the receiver can be reduced to any degree desired by reducing slot time T_s . (see §10.8).

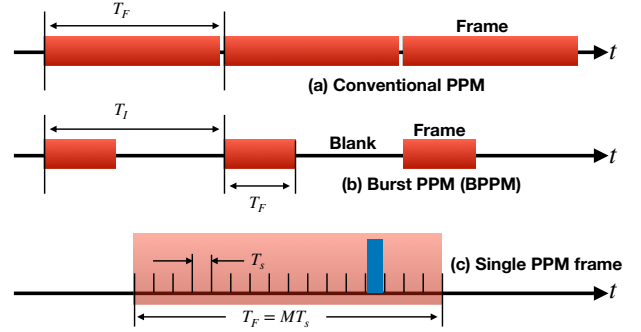


Figure 4. An illustration of two forms of pulse-position modulation (PPM). (a) In conventional PPM the time axis is filled with PPM frames, or $T_F = T_I$. (b) In burst-PPM (BPPM) the PPM frame duration T_F is decoupled from the inter-frame interval T_I by choosing a very small value for T_s , allowing for blank intervals between frames. (c) The internal structure of each PPM frame consists of M time slots, each with duration equal to the slot time T_s .

- As the propagation distance D from the probe increases, the data rate \mathcal{R} has to decrease (starting at \mathcal{R}_0 at the beginning of transmission following the completion of scientific data collection) to accommodate the decreasing signal power reaching the receiver. Similarly probes with different masses or more advanced technology may have greater electrical power available, allowing for an increase in \mathcal{R} . In PPM it is cumbersome to modify \mathcal{R} , but with BPPM changes in rate are trivially accomplished by changing the blank interval time while keeping frame interval T_F constant. This is a major theoretical and practical simplification of the design, because no adjustment in optical bandwidth, ECC or other aspect of the design is required (see §10.3).
- It is difficult to achieve the desired selectivity in a receiver optical bandpass filter with current technology, and adjustment of bandwidth to a changing data rate is also a challenge. With BPPM the optical bandwidth can be increased to any degree desired, relaxing the selectivity requirement, and can be held fixed across time, distance, and probes with different masses. This accrues without penalty in background radiation since the increased bandwidth is compensated by the longer blank intervals (see §10.8).

¹⁰ In the dark-count dominated regime BPPM doesn't actually increase P_P^T , because it increases PAR by reducing average power rather than increasing peak power (see Fig.21).

The receiver, as part of the post-processing, must synchronize its timing with frames and slots, a function-

ality called *timing recovery*.¹¹ With knowledge of the frame and slot timing, there are three possibilities for how many photons are detected:

- One or more photons are detected within the slot populated at the transmitter, but none in the other slots nor the blanking interval.
- No photons are detected within the entire frame, which is declared a *frame erasure*.
- One or more photons are detected within two or more slots, which is declared a *recognized frame error*.
- One or more photons are detected within exactly one slot not populated at the transmitter. This is an *unrecognized frame error*.

Erasures are a manifestation of signal shot noise and frame errors are attributable to background radiation.

Knowledge of erasures and recognized frame errors is preserved for subsequent processing. We find that to achieve high photon efficiency BPP the rate of erasures must be 80-90%, but the inclusion of substantial error-correction redundancy can overcome these erasures and yield acceptably low error rates in the recovery of the scientific data (see §14).

In the conventional PPM shown in Fig.4a the blank intervals are eliminated, but in the BPPM shown in Fig.4b blank intervals between frames are allowed (conventional PPM is a special case). In this case the *duty cycle* $\delta = T_F/T_I$ is defined. We can think of BPPM as a higher-data-rate transmission scheme operating with a low duty cycle $\delta \ll 1$. It is important to note that $m/T_I \gg \mathcal{R}$ where m/T_I is the “raw” data rate carried by BPPM frames and \mathcal{R} is the rate of reliable recovery of scientific data. This disparity is attributable to the added redundant data associated with error-correction coding (see §14.3).

7. PROBE MASS TRADEOFFS

A feature of a directed-energy launcher is that, for a fixed launcher infrastructure, a variety of probe versions with different masses can be launched.¹² The probe speed u_0 and initial data rate \mathcal{R}_0 in Tbl.2 are used in the numerical examples here. These are estimates for a lowest-mass “wafer scale” version. The question is, on what basis do we choose a probe mass?

In terms of scientific outcomes the \mathcal{R}_0 is of only indirect interest. In terms of the scientific mission the

¹¹ Timing recovery is a standard function of all digital communication systems, and will not be addressed further. This is one of the post-processing functions included in Fig.3.

¹² The many uses of a launcher, its deployment, as well as the benefits and issues of various mass missions are discussed in (Lubin 2020).

Table 5. Data latency/volume for planetary missions^a

Target Mission	Neptune Voyager 2	Pluto New Horizons
Data rate \mathcal{R}	~ 1 kbps	~ 1 kbps
Data latency T_L	12 yr	10.5 yr
Data volume \mathcal{V}	18 Gb	50 Gb

^a 9000 images were returned from Neptune (Smith et al. 1989) at 2 Mb per image (Ludwig & Taylor 2016). The data rate was programmable and variable. The Pluto scientific data return was 50 Gb (Fountain et al. 2009).

performance metrics of direct interest are the total data volume \mathcal{V} returned, the data latency T_L , and the reliability with which the data is recovered (see §2.2). We now show that there is an optimum mass m such that T_L is minimized for a given \mathcal{V} , or \mathcal{V} is maximized for a given T_L . Thus a principled way to choose the mass is to incorporate any constraints on T_L or \mathcal{V} . For comparison, estimates of these metrics for two outer-planetary missions are listed in Tbl.5.

7.1. Mass scaling approximations

The mass m strongly influences the probe speed u_0 and the initial scientific data rate \mathcal{R}_0 , which in turn determine T_L and \mathcal{V} . We define a set of scaling laws,

$$m(\zeta) = \zeta \cdot m(1)$$

$$u_0(\zeta) = \zeta^{-1/4} \cdot u_0(1), \quad \mathcal{R}_0(\zeta) = \zeta^2 \cdot \mathcal{R}_0(1). \quad (4)$$

The mass ratio $\zeta \geq 1$ is the factor by which mass is increased. Transmission starts at the target star distance $D = D_0$ and ends at distance $D_1 > D_0$. The data rate starts at \mathcal{R}_0 and decreases with D in accordance with (11). The scaling of \mathcal{R}_0 in (4) assumes that $\{P_A^T, P_P^T, A_e^T\} \propto \zeta$ (the detailed scaling depends on the specifics of the probe design). It is shown later (see (6) and (1)) that in this case \mathcal{R}_0 follows (4), with one factor of ζ due to increased P_A^T and another factor of ζ due to increased A_e^T . The scaling ratio for u_0 follows from the launch dynamics, assuming a fixed launch infrastructure (Lubin 2020).

7.2. Latency-volume tradeoff

The relationship between \mathcal{V} and T_L parameterized by ζ is determined in §C and plotted in Fig.5 for five values of ζ . The volume scales as $\mathcal{V} \propto \mathcal{R}_0(1)$, so a change in $\mathcal{R}_0(1)$ would shift all curves horizontally. There are three components of T_L : transit time, transmission time, and propagation time. The minimum T_L increases with ζ due to the greater transit time. Eventually T_L increases rapidly with \mathcal{V} due to the decreasing \mathcal{R} with D .

For each \mathcal{V} there is an optimum choice of ζ that minimizes T_L . The resulting minimum T_L vs \mathcal{V} is plotted as the dashed curve in Fig.5 and is also plotted in Fig.6. The latter plot shows the decomposition of T_L into its

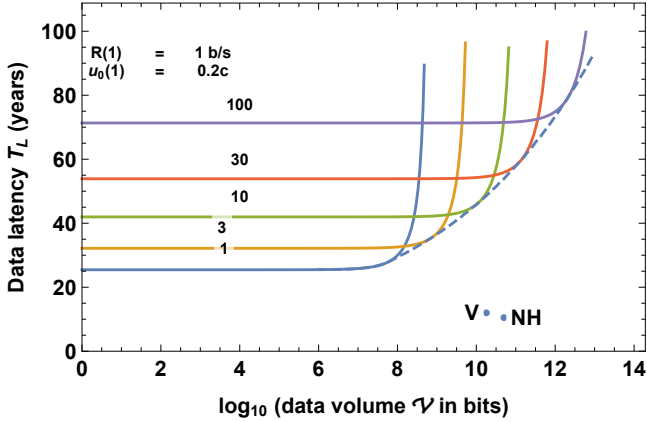


Figure 5. Plot of the data latency T_L in yr vs the logarithm of the total data volume \mathcal{V} in bits for different values of the mass ratio ζ (the curves are labeled with ζ). For example $\log_{10} \mathcal{V} = 9$ corresponds to 10^9 bits or 1 Gb. The dashed line is, for each value of \mathcal{V} , the minimum T_L achievable by the optimum choice of ζ . It is assumed that for $\zeta = 1$ (the lowest-mass probe), the speed is $u_0(1) = 0.2c$, and the initial transmit data rate is $\mathcal{R}_0(1) = 1$ b/s. The Voyager (V) and New Horizons (NH) points are obtained from Tbl.5.

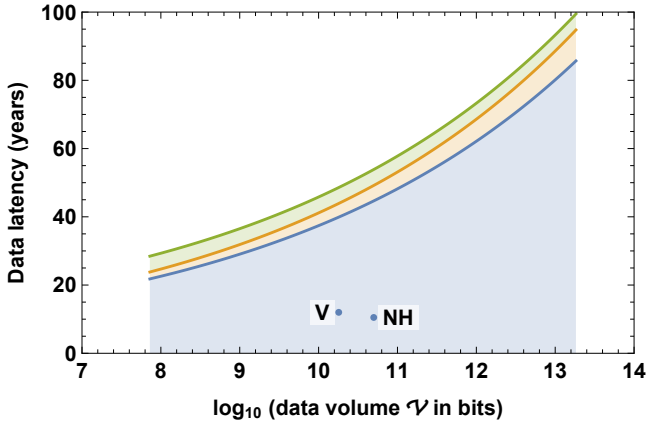


Figure 6. A plot of the data latency T_L vs data volume \mathcal{V} , where for each value of \mathcal{V} the latency-minimizing mass ratio ζ is chosen. This ranges about 28 to 100 years, where larger \mathcal{V} is associated with a larger ζ and a larger T_L . T_L is decomposed into its three components, from bottom to top: Transit time to the star, the transmission time, and the return signal propagation time, all measured by an earth clock. Latency is dominated by the transit time.

three components. The latency-minimizing value of ζ , the resulting transmission time, and the distance D_1 at the end of transmission are plotted in Fig.7.

If \mathcal{V} is increased, both the optimum ζ and T_L increase. For the optimum ζ the transmission time is always much shorter than the transit time. Obtaining a larger \mathcal{V} requires increased transmission time, but the distance traveled during transmission remains relatively constant

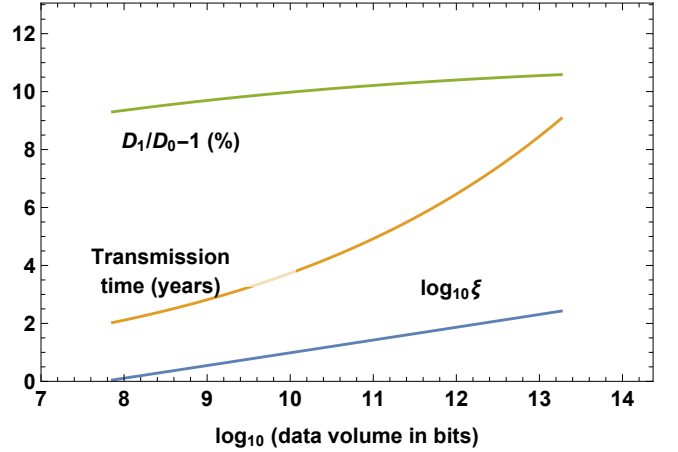


Figure 7. Three quantities of particular interest are plotted as a function of data volume \mathcal{V} . First is the log of the optimum mass ratio ζ that minimizes the data latency T_L . A plot of T_L vs \mathcal{V} for this optimum ζ is shown in Fig.6. Second is the transmission time component of T_L , which varies in the range of two to nine years. Third is the distance increase $(D_1/D_0 - 1)$ expressed as a percentage. The space probe travels a fairly consistent 9% to 10% farther than the target star during downlink transmission.

since the probe's speed is lower. For the range of parameters shown, the minimum T_L falls in the 30 to 80 year range for a data volume in the 100 Mb to Tb range. Volumes \mathcal{V} comparable to the planetary missions are feasible with the assumed $\mathcal{R}_0(1)$, but only with $\zeta \sim 20$ and $T_L \sim 50$ yr. The \mathcal{V} and T_L parameters of Tbl.2 assume that downlink operation is 10% of the probe transit time.

8. CHOICE OF WAVELENGTH

The two spectrum ranges offering atmospheric transparency for a terrestrial receiver are millimeter wave radio and visible optical. This choice affects nearly every aspect of the design. We study the optical case in this paper, but the radio possibility should also be considered.

8.1. Propagation loss

As compared to the outer planets, the propagation losses from the nearest stars approach a factor of $>10^8$. This obstacle is overcome by an adjustment to other parameters in Tbls.1, 2, 3, and 4, including prominently wavelength, data rate, and receive aperture size.

The appropriate signal level at the receiver is measured differently at radio and optical wavelengths. For radio wavelengths it is the average power $P_A^R = N^S P_A^S$, while for optical (assuming direct detection) it is the average rate of detected photons $\Lambda_A^R = N^S \Lambda_A^S$. These metrics are affected by the propagation loss and atmospheric effects, with the latter more significant at optical wavelengths (see §11). Neglecting atmospheric absorp-

Table 6. For equivalent SNR, scaling of the NH radio downlink to a low mass probe illustrating the impractically large receive aperture size that may be needed.

Parameter	NH	Low mass
Distance D_0	4.5 lh	4.24 ly
Wavelength λ_0	3.6 cm	10 mm
Transmit power P_A^T	24 W	0.1 W
Transmit aperture diameter $\sqrt{4A_e^T/\pi}$	2.1 m	10 cm
Receive aperture diameter $\sqrt{4A_e^R/\pi}$	70 m	1652 km
Data rate \mathcal{R}	1 kb/s	1 b/s

tion and turbulence, these metrics are determined by the average transmitted power P_A^T through a link budget,

$$P_A^S = \eta \cdot \frac{A_e^T A_e^S}{\lambda_0^2 D_0^2} \cdot P_A^T \quad (5)$$

$$\Lambda_A^S = \frac{\lambda_0}{hc} \cdot P_A^S = \eta \cdot \frac{A_e^T A_e^S}{hc \lambda_0 D_0^2} \cdot P_A^T \quad (6)$$

(see §B.4.2 and (B8)). The factor λ_0/hc in (6) converts from power to photons per second.

The *efficiency factor* $0 < \eta \leq 1$ in (6) accounts for non-propagation losses, such as aperture pointing error (see §12.6), as well as attenuation and the quantum efficiency in the receiver. A Doppler red shift in wavelength from transmitter to receiver has also been neglected in (6) by setting $\lambda_0^R = \lambda_0^T = \lambda_0$ (for $u_0 = 0.2c$ this shift is about 20%). Relativistic aberration has also been neglected.

8.2. Radio

Although radio is used for deep space missions today, the primary objection to radio at interstellar distances is the large aperture sizes (or alternatively large transmit power). As an order-of-magnitude estimate, factors affecting the link budget for the New Horizons (NH) mission are scaled to accommodate interstellar distances in Tbl.6. Although it would be desirable if transmit power and aperture size could be increased to compensate for the greater distance, they will likely be substantially *decreased* for low-mass probes. In principle these adverse elements can be compensated by a lower data rate, a substantially larger receive aperture area, and/or shorter wavelength. The shortest radio wavelength that consistently penetrates the atmosphere is chosen.

An appropriate link budget for radio is (5). Assuming that there is one single-mode diffraction-limited aperture which receives signal power P_A^S , the parameters contributing to this received power P_A^S are listed in Tbl.6, with reasonable assumptions for the transmit power and aperture size. When substituted into (5) the received power is found to be a factor of 10^3 smaller for the low-mass probe. This results in an equivalent signal-to-noise ratio SNR at the receiver for two reasons. First

the major noise impairments are isotropic cosmic background radiation and receiver thermal noise, which have the same white power spectral density independent of receive aperture area (see §B.4.3) and assuming equivalent receiver noise factor. Second for an equivalent modulation and coding scheme the receiver bandwidth can be reduced by a factor of 10^3 in the low-mass case due to the lower data rate, thereby reducing the noise component of SNR by the same factor.

The receive aperture is impractically large, especially considering that it is assumed to be diffraction limited. Such an aperture would also require an impractical pointing accuracy, although this requirement could in principle be relaxed by implementing a phased array with equivalent total collection area.¹³ A larger transmit aperture (with associated greater pointing accuracy), higher transmit power, or lower data rate would allow the receive aperture area to be reduced.

8.3. Optical

Relative to radio, choosing an optical wavelength yields a factor of 10^4 to 10^5 in the link budget of (6) (depending on the two wavelengths being compared). This is a considerable advantage, but optical wavelengths also pose substantial challenges. One is atmospheric effects (see §11), with the resulting scintillation (fading in communication terms) and weather-based outages.

One challenge in optical communication with direct detection (see §4.3) is a ‘mode shift’ in photon efficiency BPP vs SBR at low values of SBR. This is observed in the theoretical limit on feasible photon efficiency BPP, which is essentially independent of SBR (for fixed peak-to-average ratio PAR) for large values of SBR, but deteriorates rapidly for small SBR (see Fig.29). Intuitively this is due to the effect of modulation and detection based on signal power (photon count), and the effects of square-law detection on background radiation. The case is made in (Toyoshima et al. 2007; Moision & Farr 2014) that a probe receding in distance from earth will suffer a deterioration in SBR due in part to a reduction in data rate and signal power in the face of a fixed (or even growing) background radiation, and as a result the link budget switches dependency from D^2 to D^4 . However, these papers make specific technological assumptions as to modulation and parameter scaling relations with D

¹³ The incoherent accumulation of power as in Fig.3 is not acceptable since the NH modulation and coding scheme strongly exploits both signal amplitude and phase. Accurate phasing across constituent apertures is necessary.

(such as holding optical bandwidth fixed even as the signal bandwidth decreases).¹⁴

A desirable D^{-2} behavior can be achieved at deteriorating SBR by replacing PPM by a more nuanced modulation and coding (Jarzyna et al. 2019), although this is unproven in practice. Here we use a simpler approach of simply constraining SBR to be relatively large. Fortunately for a space mission and its presumed maximum propagation distance $D = D_1$ this challenge is circumvented by ensuring that SBR is relatively large at distance D_1 . We constrain SBR to a relatively large value at this distance (in our case $\text{SBR}=4$), with a correspondingly large average transmit power P_A^T . This is assisted by BPPM (see §6.2), which allows us to hold optical bandwidth W_e fixed (subject to any technological limitations on bandpass filtering) without penalty in SBR as D increases, although a price is paid in a correspondingly growing peak transmit power P_P^T .

Our numerical results in §10.9 subject to these assumptions do strongly suggest that communication with low-mass probes at optical wavelengths is not feasible given the current state of technology. We identify here some key technologies that must advance to empower optical communication in this application. These are: achieving relatively high peak powers at the optical detector through pulse compression or other means (see §13.1); more selective optical bandpass filtering (see §13.2); attenuation of interference by a coronagraph function (see §12.7); receiver optics (including superconducting optical detectors) with very low dark counts (see §13.3); and highly accurate probe attitude control and aperture pointing.

Since the relative advances in these technologies cannot be anticipated with any degree of certainty, BPPM is chosen as a modulation technique that offers greater freedom in trading off advances in some of these technologies (see §6.2). Achieving a relatively large and constrained SBR at the greatest distance D_1 is aided by the minimal increase in distance (about 10%) during transmission (see Fig.7). The requirements for these four technologies and related tradeoffs are studied by numerical modeling in §10.9.

8.4. Space-based receiver

Although not considered further here, a space-based receiver would be advantageous for the elimination of atmospheric effects and also the possibility of going to ultraviolet (UV) wavelengths (10 to 400 nm). UV would further moderate aperture sizes and substantially reduce

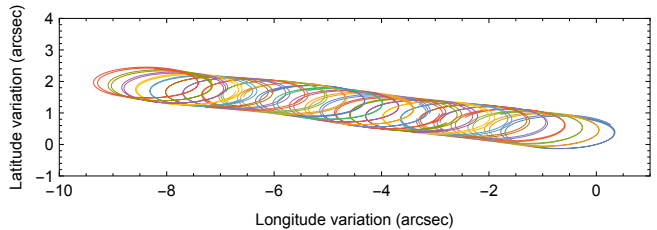


Figure 8. The variation in probe coordinates as viewed by a common terrestrial receive aperture. The variation in the longitude and latitude (in arcsec in an ecliptic coordinate system) for 26 probes launched at 30-day intervals is shown. The origin corresponds to the angle of Proxima Centauri when viewed from the initial launch site. Each elliptical trajectory is due to the parallax effect of the receiver orbit about the sun over a period of 2.21 yr, which corresponds to a probe’s travel 10% farther than the star. The general drift of the probe positions is due to the star’s proper motion, presenting a moving target for the various probes.

the star interference (see §10.9 and (Lubin 2020)). While UV laser communications is not currently technologically advanced (due primarily to its inability to penetrate the atmosphere) it is an option to consider for the future.

9. TRAJECTORIES AND COVERAGE

The coverage Ω_A of each aperture determines the effective area A_e^S , which in turn influences the transmit power-area product $P_A^T A_e^T$ necessary to achieve the desired SBR at the receiver. The parameters affecting coverage are (beyond our control) parallax and the star’s proper motion and (under our control) the swarm launch schedule and sophistication of the aperture beamforming.

9.1. Concurrent swarm probe communication

The probe trajectories as viewed from Earth are shown in Fig.8 for a specific launch schedule.¹⁵ The chosen parameters, including duration of transmission and interval between launches, results in 26 probes transmitting concurrently Tbl.1, each one operating a downlink for 2.21 yr in Tbl.2 (see §7.2). For the position of Proxima Centauri relative to the earth’s orbit, the overall longitudinal parallax angular variation (~ 2 as) is about twice as great as the latitudinal (~ 1 as).

The star’s proper motion determines the relative position of probes launched at different times. For Proxima Centauri this motion is 368 mas/yr and -3775 mas/yr

¹⁴ There is also one error in (Moision & Farr 2014), with the assumption that isotropic sources of noise increase as the effective area and directivity of the receive aperture is increased to compensate for greater distances. Actually noise due to unresolved sources is independent of directivity because the greater gain of a larger aperture is exactly offset by its smaller coverage (see §B.4.3).

¹⁵ The variation in angle due to parallax does not depend on the chosen coordinate system. To readily capture the earth’s orbit, a heliocentric ecliptic XYZ coordinate system is used. The earth orbit and a fixed star position were obtained from Mathematica® `StarData["Heliocoordinates"]` and `PlanetData["Heliocoordinates"]` followed by transformation to spherical coordinates.

in declination and right ascension respectively.¹⁶ Fortuitously, the largest component of proper motion is aligned with the largest overall parallax (longitude and right ascension). The trajectories of consecutively launched probes will sometimes coincide (unless the inter-launch interval is greater than about eight months) and thus their signals could not be consistently separated spatially.

The coverage implications depend on the refinement in beamforming in each aperture. Minimizing coverage (maximizing sensitivity) requires beamforming the precise location of each probe, while the simplest beamforming simply captures the full variation in parallax shown in Fig.8 for each probe and also across the relative positions of successive probe launches. The numerical results in §10.9 address these disparate cases by considering a range of Ω_A values.

At longitude l and latitude b the solid angle of coverage is, for small Δl and Δb ,

$$\Omega_A \sim \cos(b) \cdot \Delta b \Delta l \quad (7)$$

Based on Fig.8 for the simplest beamforming we have $\Delta b \approx 1$ as, and for Proxima Centauri $\cos(b) = 0.71$. Δl is dominated by proper motion and is $\Delta l \sim 10$ as for the assumptions in Fig.8, and thus $\Omega_A \approx 7.1$ as². To account for the practicalities of sidelobes we assume that $\Omega_A = 10$ as² in Tbl.3.

The coverage can be manipulated by the launch schedule. For example Ω_A could be reduced by moving toward a *burst-mode launch schedule*, in which a sub-swarm of probes are launched at closely spaced times interspersed with launch-inactive time periods greater than the individual-downlink operation time (on the order of two years for the parameters of Tbl.2 and Fig.7).

9.2. Single-probe communication

At the other extreme, if a receive aperture is dedicated to a single probe and can dynamically compensate for parallax and atmospheric refraction of the signal path, the smallest coverage solid angle Ω_A will be determined by the aperture pointing accuracy. If we assume that with adaptive optics the pointing accuracy of the apertures is ≈ 0.1 as, then the coverage can be no smaller than $\Omega_A \approx 0.01$ as² (this the value assumed in Tbl.3).¹⁷ Our goal in the numerical results is to consider this entire range of possibilities.

10. MODEL AND NUMERICAL RESULTS

Before discussing the key enabling technologies, it is helpful to appreciate the trade-offs available through the

¹⁶ Obtained from Mathematica® StarData["ProperMotion"].

¹⁷ The $A_e^S = 707$ m² assumption in (Parkin 2019) implies $\Omega_A = 9.4 \cdot 10^{-5}$ and hence an aperture pointing accuracy on the order of 0.01 arcsec or better. The aperture sensitivity and the target star interference calculations are strongly dependent on this assumption.

Table 7. Receive aperture design equations with BPPM

Parameters:	
Data reliability:	SBR, BPP, \mathcal{R}_0 , W_e , K_s^R , m
Geometric:	b , Δb , Δl , Ω_A , λ^R , D_0
Physical:	η , F_c , F_x , T_s , $\Lambda_{N,I,D}^S$
Transmitter:	
$T_F = MT_s$	$W_e T_s > 1$
$P_P^T T_s = P_A^T T_I$	$T_I \mathcal{R}_0 = K_s^R \cdot \text{BPP}$
$\text{BPP} = \frac{1 - e^{-K_s^R}}{K_s^R} \cdot m$	$M = 2^m$
Receive aperture:	
	$\Lambda_P^S = \frac{P_P^T A_e^T A_e^S}{hc \lambda^R D_0^2}$
$K_s^S = \eta \Lambda_P^S T_s$	$K_X^S = \eta F_x \Lambda_P^S T_F$
$K_N^S = \eta \Lambda_N^S W_e T_F$	$K_I^S = \eta F_c \Lambda_I^S W_e A_e^S T_F$
$K_D^S = \Lambda_D^S T_F$	$\text{SBR} = \frac{K_s^S}{K_X^S + K_N^S + K_I^S + K_D^S}$
$A_e^S \cdot \Omega_A = (\lambda^R)^2$	$\Omega_A = \cos(b) \cdot \Delta b \Delta l$
Receive collector:	
	$N^S = K_s^R / K_s^S$
Metrics:	
	A_e^S, P_A^T, P_P^T, N^S

choice of parameters of BPPM. BPPM is specifically designed to permit a greater advancement of one technology to offset a lesser advancement of another. This is reflected in the modeling equations for BPPM in Tbl.7, which are now described and then used in an extended numerical example.

from the choice of parameters listed in Tbls.1, 2, 3, and 4 are listed in Tbl.8, along with a few additional chosen parameters and Excel® implementations of Tbl.7 are available for self-exploration of the parameter space (Messerschmitt 2020). This is our nominal design, and in the following the scaling of performance with changes to chosen parameters is described.

Although the values of N^S are quite large, the possibility of multiple-aperture assemblages addresses some concerns (see §5.2.1). For example $N^S = 5.9 \cdot 10^7$ can be accommodated by 5900 assemblages, each accommodating a 100×100 array of apertures. The total area metric $A_e^S N^S$ may be a more accurate indicator of collector capital cost.

10.1. Metrics and methodology

Achieving a gram-scale probe mass limit is challenging. For this purpose a useful metric for a design is the product of the transmit {average, peak} power and aperture effective area $\xi_{\{A,P\}}^T = P_{\{A,P\}}^T A_e^T$, which should be monotonically related to probe mass due to their impacts on electrical power generation and the transmit aperture size (see §7.1). Fixing a value for $\xi_{\{A,P\}}^T$ admits a tradeoff between transmit power and aperture area without affecting the signal level as seen by the receiver.

Table 8. Transmitter and receiver performance metrics

Description		Swarm	Single
P_A^T	Avg. transmit power (mW)	29.4	0.8
P_P^T	Peak transmit power (kW)	638.	17.4
K_s	Average detected photons per slot	0.2	
ρ_M	Reduction in moonlight irradiance relative to full moon	1	
Λ_D^S	Avg. rate of dark counts referenced to each receive aperture (ph/yr)	32.0	
SXR	Signal-to-extinction ratio	2441.	
SIR	Signal-to-interference ratio	152.	4.15
SNR	Signal-to-noise ratio	8.3	226.
SDR	Signal-to-dark count ratio	8.2	223.
N^S	Number of receive apertures	$5.9 \cdot 10^7$	$2.2 \cdot 10^6$
$A_e^S N^S$	Total effective aperture area (km ²)	0.04	1.47

Our design methodology is to minimize the average-power-area metric ξ_A^T subject to reliable recovery of scientific data, constraints on receiver coverage accommodating probe-swarm trajectories, and the physical limitations imposed by background radiation and self-noise in the receiver. This minimization is achieved by operating at the lowest SBR consistent with reliable data recovery, operating near the theoretical limits of photon efficiency, and subject to the fundamental physical constraints on a receive aperture imposed by the desired coverage. A major component of receiver cost is the receive aperture. A metric relating to that cost is the receive aperture total effective area $A_e^S N^S$. We do not choose or constrain N^S , but rather ascertain the value required to achieve reliable data recovery subject to that minimum ξ_A^T . Subsequently we consider the implications of varying N^S about this unconstrained choice.

Recognizing a tradeoff between $\xi_{\{A,P\}}^T$ and receive aperture area, another useful metric for a design is the *end-to-end* power-area-area metric

$$\xi_{\{A,P\}}^{TR} = P_{\{A,P\}}^T A_e^T \cdot A_e^S N^S = \xi_{\{A,P\}}^T \cdot A_e^S N^S.$$

We now display the dependence of $\xi_{\{A,P\}}^{TR}$ on other parameters, which offers considerable insight.

10.2. Transmitter/receiver tradeoffs

There is a practically significant tradeoff between the transmitter power-area metric and the required number of receive apertures. As now established, increased transmitter resources (power and aperture area) can be traded for a reduced receiver burden (number of apertures).

10.2.1. End-to-end metrics

The design equations in Tbl.7 determine the end-to-end metrics $\xi_{\{A,P\}}^{TR}$ defined in §10.1 as

$$\xi_A^{TR} = \xi_A^T \cdot A_e^S N^S = \frac{hc\lambda_0^R D^2}{\eta} \cdot \frac{\mathcal{R}}{\text{BPP}} \quad (8)$$

$$\xi_P^{TR} = \xi_P^T \cdot A_e^S N^S = \frac{hc\lambda_0^R D^2}{\eta} \cdot \frac{K_s^R}{T_s}. \quad (9)$$

ξ_A^{TR} in (8) is a reformulation of the single-aperture link budget (6) for the canonical receive collector of Fig.3. Expressed in terms of coverage solid angle Ω_A , (8) and (9) become

$$\xi_{\{A,P\}}^T = \frac{hcD^2}{\lambda_0^R \eta} \cdot \frac{\Omega_A}{N^S} \cdot \left\{ \frac{\mathcal{R}}{\text{BPP}}, \frac{K_s^R}{T_s} \right\}. \quad (10)$$

Thus for fixed coverage we have that $\xi_{\{A,P\}}^T \propto (N^S)^{-1}$, so that if desired N^S can be reduced at the expense of added transmit power or aperture area or both (see §10.5.1). This tradeoff is actually exercised by manipulating the hidden parameter SBR. Increasing $\xi_{\{A,P\}}^T$ results in a higher SBR at each receiver aperture (because of a larger signal rather than lower background radiation), and this in turn allows an adequate signal level at the optical detector with a smaller number of apertures.

With respect to average power, ξ_A^T in (10) quantifies the adverse effect of achieving a smaller BPP and/or smaller quantum efficiency η , and establishes a linear dependence of average power on scientific data rate \mathcal{R} . It also shows that for fixed coverage Ω_A , a longer wavelength is advantageous, although this fails to account for an important effect of wavelength on background radiation. Because it is blind to SBR, (10) also fails to capture a reduction in background radiation that follows from reducing BPP (see §10.5.2).

With respect to peak power, (10) shows an invariance of ξ_P^{TR} to \mathcal{R} and BPP, but rather a dependence on parameters T_s and K_s^R .

10.2.2. Parameter consistency issues

For any set of *consistent* parameter choices, (10) is satisfied. However, (10) is not satisfied for any *arbitrary* choice of the data reliability parameters $\{\text{SBR}, m, K_s\}$, because BPP depends strongly on these parameters and (10) assumes that a photon efficiency BPP is actually achieved. We must chose $\{\text{SBR}, m, K_s\}$ and then determine the resulting BPP before invoking (10). The average power-area tradeoff is strongly influenced by BPP, and this imparts a strong motivation to increase BPP.

Parameter K_s^R , the average number of detected signal photons for each PPM slot, has a major influence on data reliability since it determines the shot-noise induced rate of PPM frame erasures. To achieve a large

BPP, which beneficially reduces ξ_A^{TR} , it is perhaps surprising that K_s^R must be very small, resulting in a high probability of frame erasure (see §14.3). A nearly optimum choice across a range of conditions is $K_s^R \approx 0.2$ (see §14.3.2). This is termed *photon starvation* of the PPM frames, and small K_s^R beneficially reduces ξ_P^{TR} as well. On the other hand, the equivalent parameter K_s^S at an aperture output is determined by SBR, and is not directly related to BPP or data reliability. The purpose of the scale-out of apertures by the factor $N^S = K_s^R/K_s^S$ is to multiply the value of K_s by incoherently accumulating received photons.

The signal-to-background ratio SBR must also be large enough to support the assumed photon efficiency BPP (see §E). Since the background radiation is determined by the aperture, the minimum SBR requirement imposes a lower bound on the average signal power at each aperture, and thus places a lower bound on $\xi_{\{A,P\}}^T$ (see §10.5).

10.3. Changes with increasing propagation distance

The downlink propagation distance D ranges over $D_0 < D < D_1$, where D_0 is the distance to the target star (corresponding to scientific data acquisition) and D_1 is the distance at which transmission is completed. As D increases in this range, a goal is to hold constant both the average transmit power (which is determined by the electrical generation capacity) and the reliability of scientific data recovery. It follows that the only parameters in the end-to-end metrics that can change are data rate \mathcal{R} and peak transmit power P_P^T . Assuming (8) remains fixed, we must have $\mathcal{R} \propto D^{-2}$. If the initial data rate at $D = D_0$ is \mathcal{R}_0 then

$$\mathcal{R}(D) = \mathcal{R}_0 \cdot \left(\frac{D_0}{D}\right)^2. \quad (11)$$

For fixed data reliability we choose to keep $\{M, T_s, T_F, K_s\}$ fixed with D . Based on Tbl.7, \mathcal{R} can be changed simply by adjusting the frame interval $T_I \propto \mathcal{R}^{-1}$. In addition, based on (9) the peak transmit power has to be increased as $P_P^T \propto D^2$.

In summary, as D increases \mathcal{R} is adjusted downward by increasing T_I , and P_P^T is increased to maintain a fixed reliability and also a fixed P_A^T . All ECC parameters and algorithms remain fixed, which is one of the desirable features of BPPM.

10.4. Coverage

The sensitivity of the aperture is determined by A_e^S , as seen in the relation for Λ_P^S , and thus coverage and sensitivity are inversely related. That is, a swarm of probes received concurrently by a single receive aperture, to the extent that this necessitates a larger Ω_A , increases the required $P_{\{A,P\}}^T$ for each probe (see Tbl.8 for a specific example).

10.5. Power-area tradeoff

It is useful to numerically characterize the transmitter/receiver tradeoffs described analytically in §10.2. The tradeoff between receive collector total area and transmit average and peak transmit powers (for a fixed transmit aperture area A_e^T) is shown in Fig.9 and Fig.10 for the swarm and single probe coverage cases respectively, holding the transmit aperture A_e^T fixed. The range in powers and areas is very large, with impractically large powers on the left (corresponding to a single collector aperture) and impractically large receive collector areas on the right (corresponding to the minimum photon efficiency). As expected, the transmit powers are smaller in the single probe case of Fig.10, and as a result the received collector areas are generally larger.

10.5.1. Reducing receive collector area

Relative to the nominal design with parameters defined in Tbls.1, 2, 3, and 4, the receive collector area can be reduced by increasing SBR. Since background radiation is not affected when A_e^S is fixed, an increase in ξ_A^T is reflected by an increase in photon rates at the aperture output, an increase in SBR, and a commensurate reduction in N^S for a fixed photon efficiency BPP. The largest SBR and transmit power corresponds to a single collector aperture ($N^S=1$).¹⁸

10.5.2. Reducing transmit power

Again relative to the nominal design parameters, the transmit power can be *reduced* in the specific context of PPM or BPPM by reducing the photon efficiency BPP through a reduction in the number of slots M per frame. The primary effect of reducing BPP is to increase the N^S needed to achieve a large enough photon rate to support the assumed scientific data rate \mathcal{R} . This larger receive collector area results in lower transmit powers.

Specifically this trend is due to a reduction in background radiation, and permitting the transmit powers to be decreased while maintaining the desired SBR. In PPM, BPP is controlled by adjusting the bits per PPM slot m , with BPP $\approx 0.9m$ for the nominal value of K_s . For conventional PPM, reducing m also beneficially increases time-slot duration T_s , and thus reduces optical bandwidth W_e and thus $\Lambda_{I,N}^S$ in Tbl.9. For BPPM, holding T_s and W_e fixed imply that $\Lambda_{I,N}^S$ remains fixed, but the frame duration T_F is proportional to 2^m and thus reducing m has the effect of reducing background photon counts $K_{X,I,N,D}^S$ in Tbl.7. Reducing BPP to increase aperture area is less efficient for average power than it is for peak power due to the increase in area needed to

¹⁸ The design assumption made in (Parkin 2019) is $N^S=1$, with the goal of minimizing the received collector area. As a result the required transmit area-power metric ξ_A^T is more than eight orders of magnitude larger than the nominal design here, but of course the receive collector area is much smaller.

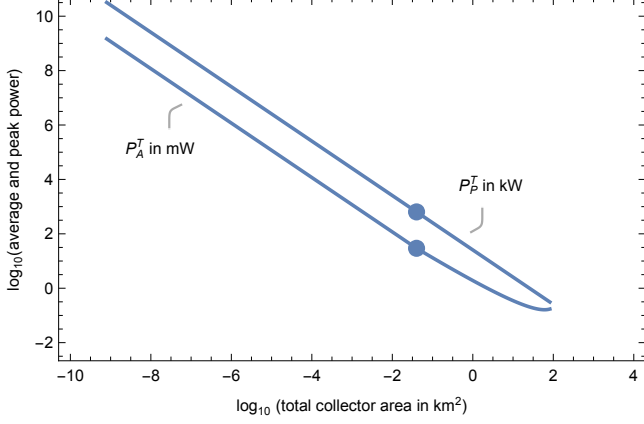


Figure 9. A log-log plot of the average transmit power P_A^T and peak transmit power P_P^T vs the total receive aperture effective area $N^S A_e^S$ with fixed coverage ($\Omega_A = 10 \text{ arcsec}^2$) corresponding to the swarm probe case. The units are milliwatts for average power and kilowatts for peak power, so there is a six order of magnitude difference between the two curves. The dots represent the nominal case for the parameters listed in Tbls.1, 2, 3, and 4. The larger powers to the left of the dots reflect a larger choice for SBR, culminating with the SBR corresponding to a single aperture ($N^S=1$). The smaller powers to the right of the dots reflect a smaller choice for BPP, culminating in BPP=1, corresponding to a PPM frame with just two slots ($M=2$).

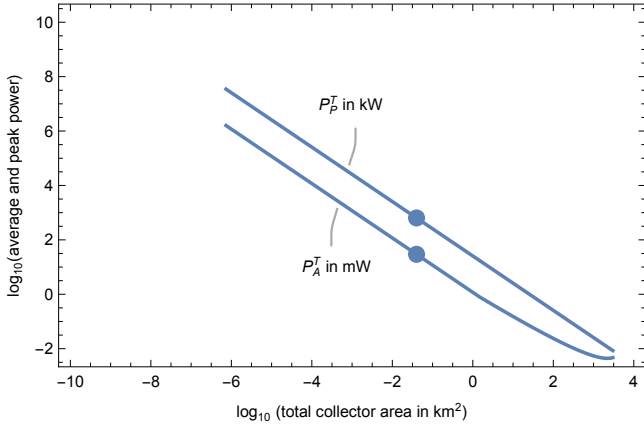


Figure 10. Fig.9 is repeated for fixed coverage ($\Omega_A = 0.01 \text{ arcsec}^2$) corresponding to the single probe case.

accommodate poorer photon efficiency, which begins to offset the beneficial reduction in background radiation at small BPP.

10.6. Background radiation

The relevant average detected photon rates at each aperture are listed in Tbl.9 for each of the four sources of background. These are related to the detected peak photon rate Λ_P^S and the three physical parameters $\Lambda_{N,I,D}$, the appropriate units for which are listed in the third col-

Table 9. Constituents of background radiation

Source	Avg. ph/s	$\Lambda_{P,N,I,D}$ units
Source extinction	$\eta F_x \Lambda_P^S$	ph/s
Unresolved noise	$\eta \Lambda_N W_e$	ph/s-Hz
Host star interference	$\eta F_c \Lambda_I A_e^S W_e$	ph/s-Hz-m ²
Detector dark counts	Λ_D^S	ph/s

umn. Like the probe signal, the three incident sources of radiation are affected by detection efficiency η , whereas the dark count rate is intrinsic to the detector and thus is not affected by η . Thus dark counts become a more significant contributor to SBR as η decreases.

Noise and interference are broadband sources of radiation, and thus as they reach the optical detector are proportional to W_e , the bandwidth of the receive optical bandpass filter which precedes that detector. The extinction ratio $F_x < 1$ determines the background following the optical bandpass filter that is related to incomplete extinction of the source.

Noise (due to unresolved sources of radiation) is considered to be isotropic over the coverage solid angle Ω_A , and thus the captured photon rate is independent of A_e^S for a single-mode diffraction limited aperture. This is because any changes to collection area are offset by the resulting change in coverage solid angle (see §B.4.3).

Interference (originating with the target star) is essentially a point source like the probe transmitter. It can be approximated as a plane wave when it reaches the aperture, and the captured photon rate is thus proportional to the aperture effective area A_e^S . Any rejection of this interference due to it falling outside the coverage angle or other coronagraph functionality is modeled by the coronagraph rejection ratio $F_c \leq 1$.

Dark counts are distinctive in being unaffected by either W_e or A_e^S .¹⁹ This presents a unique challenge because we cannot limit dark counts originating in the detector (as opposed to receive optics) by optical bandpass filtering.

10.7. Conditions on extinction ratio

Returning to Tbl.7, the average photon counts per frame for signal (K_s^S) and for incomplete extinction (K_X^S) are related to the peak signal power Λ_P^S . This implies an upper limit on the permissible extinction ratio F_x that is related to the desired SBR. Eliminating Λ_X^S from the equations,

$$K_s^S = \frac{\text{SBR}(K_N^S + K_I^S + K_D^S)}{1 - M F_x \cdot \text{SBR}}. \quad (12)$$

¹⁹ This may not be true of dark counts originating as blackbody radiation from the optics preceding the optical bandpass filtering (see §13.3).

Thus incomplete extinction ($F_x > 0$) results in a compensating increase in the required K_s^S , which in turn requires an increase in P_P^T . This increase is unrelated to other sources of background, and since it is not a function of T_I is also unrelated to the benefits of BPPM (see §10.8). Based on (12), a feasible design requires

$$F_x < (M \cdot \text{SBR})^{-1}. \quad (13)$$

This conclusion also follows directly from $\text{SBR} < \text{SXR}$ (since incomplete extinction is one component of SBR) and $\text{SXR} = 1/MF_x$.

10.8. Opportunities afforded by BPPM

The slot time T_s plays a central role in Tbl.7. First, choosing a smaller T_s assists in achieving the targeted SBR by reducing all three of $K_{\{N,I,D\}}^S$. This boost in SBR results from ignoring all photon detection events that occur during the blank intervals in Fig.4. The price paid for smaller T_s is an increase in peak transmitted power P_P^T .

The reduction in dark counts arising from smaller T_s is especially advantageous, since dark counts originating in the detector (as opposed to receive optics) are unabated by bandlimiting. This is significant because the numerical results in §10.9 suggest that dark counts are typically a very significant contributor to overall background radiation for larger coverages Ω_A . This parallels radio telescopes, where thermal noise introduced in the receiver electronics typically dominates cosmic sources of noise.

Another important parameter in Tbl.7 that relates to technology issues is the optical bandwidth W_e imposed at the receiver, since this determines the level of noise and interference reaching the optical detector. The minimum bandwidth is determined by $W_e T_s \sim 1$, and it is natural to keep T_s fixed as distance D increases as well as across different probes (even if they have differing masses and data rates). As a result, the optical bandwidth does not require agility or configurability.

The total noise and interference is always proportional to $W_e T_s$, and thus remains fixed if W_e is coordinated with T_s . Thus BPPM does not help (or hurt) with respect to total noise and interference at the optical detector. A reduction in T_s to minimize dark counts also increases the optical bandwidth W_e without increasing background radiation. In terms of optical bandpass filter technology this is desirable since it relaxes the required selectivity. In effect BPPM trades off background suppression (except for dark counts) between the frequency and time domains. Time-domain suppression is technologically preferable because it is simpler to implement and more precise. Thus all considerations (other than peak power) argue in favor of making T_s smaller.

10.9. Parameter-metric sensitivity

We now justify the choice of parameters in Tbls.1, 2, 3, and 4, followed by a study of the sensitivity of these parameters to changing assumptions.

10.9.1. Choice of nominal parameters

The choice of $\mathcal{R}_0 = 1$ b/s is a convenient (but rather arbitrary) choice. This is the scientific data rate during periods of non-outage, but for the chosen daylight and weather outage probabilities the net scientific data rate is $\mathcal{R}_a = 0.432$ b/s (see §14.4). For fixed coverage and also holding $\{K_s^R, T_s\}$ fixed, based on (10) reducing \mathcal{R}_0 is a way to either reduce the transmitter average power-area metric ξ_A^T (which has no effect on peak power P_P^T) or alternatively reduce the number of receive apertures N^S (which has the adverse effect of increasing the required peak power-area metric ξ_P^T). Surprisingly reducing ξ_P^T requires us to *increase* \mathcal{R}_0 and $N^S \propto \mathcal{R}_0$. Alternatively ξ_P^T can be reduced by increasing PPM slot time T_s , but this increases susceptibility to dark counts.

The reliability parameters in Tbl.3 must be self-consistent based on available theoretical bounds on the achievable BPP consistent with reliable recovery of scientific data. First, neglecting background radiation (that is $\text{SBR} = \infty$), the choice $m=12$ places an upper bound $\text{BPP} < 12$ b/ph based on (3). This is true of any possible modulation coding scheme. For the specific case of PPM, the theoretical upper bound is $\text{BPP} < 10.9$ b/ph for the chosen m and K_s based on (18). Second, taking into account background radiation, for this value of $\text{PAR} = M$, the choice $\text{SBR} = 4$ results in the theoretical bound $\text{BPP} \leq 11.1$ b/ph for any photon-counting detector (see §E). Thus all available theoretical bounds are consistent with the assumption $\text{BPP} = 10.9$ in Tbl.3. Concrete ECC methods are not expected to quite achieve these theoretical bounds, so this BPP can be considered mildly optimistic.

A rather arbitrary choice is the dark count rate $\Lambda_D^S = 32 \text{ yr}^{-1}$, because we don't know what value may be feasible in the future. Assuming nighttime-only operation of the downlink (see §10.9.4), the two most significant sources of background (for the shorter wavelength) are moonlight and dark counts. The value Λ_D^S is chosen so that these two sources are about equal ($\text{SNR} \approx \text{SDR}$) at the largest coverage ($\Omega_A = 10 \text{ as}^2$). Thus, a larger (or smaller) Λ_D^S will render dark counts (or moonlight) the dominant source of background radiation under these specific conditions.

The choice of transmit aperture effective area A_e^T is also rather arbitrary, choosing an area that seems consistent with a low-mass probe. Both the transmit powers $P_{\{A,P\}}^T$ are inversely proportional to A_e^T , so increasing this area is directly beneficial in terms of power.

From (13) $F_x < 6 \times 10^{-5}$ for the parameters in Tbls.1, 2, 3, and 4. A 77 dB extinction ratio ($F_x = 2 \times 10^{-8}$) has been achieved in bench testing (Farr et al. 2013). The

$F_x=10^{-7}$ value in Tbl.2 thus appears feasible today, and renders incomplete extinction a relatively minor contributor to the background.

The effect of changes to wavelength λ_0^R are multifaceted. If the coverage Ω_A is held fixed, effective area A_e^S is proportional to $(\lambda_0^R)^2$ and thus the signal power increases in proportion to λ_0^R in (6), the interference increases in proportion to $(\lambda_0^R)^2$ from Tbl.9, and hence overall there is increased interference. For a red-dwarf star such as Proxima Centauri the interference is magnified further because of the wavelength-dependence of the star black body radiation (see Tbl.10). Increasing the wavelength to $\lambda^R=1 \mu\text{m}$ in Tbl.3 causes interference to replace moonlight and dark counts as the dominant component of background radiation, and results in a substantial increase in transmit power (to $P_A^T=562 \text{ mW}$ and $P_P^T=12.2 \text{ MW}$) for the swarm case in Tbl.8. This larger interference could be mitigated by a larger coronagraph rejection (smaller F_c).

Reduction in Ω_A from the swarm to single-probe case in Tbl.3 beneficially reduces the transmit powers due to the larger effective area A_e^S of the aperture, but increases the total receive aperture area $A_e^S N_S$. Thus, reducing Ω_A yields the expected tradeoff between a larger receive aperture and reduced transmit powers. Similarly a larger transmit aperture effective area A_e^T can be directly traded for smaller transmit powers.

Unfortunately it appears that the required P_P^T cannot be achieved by available semiconductor lasers. Some ideas for potentially circumventing this issue, none of them currently qualified, are discussed §13.1.

Each PPM frame in BPPM represents $K_s^R \cdot \text{BPP}$ bits of scientific data on average, and since this equals the number of scientific data bits $T_I \mathcal{R}_0$ in each frame, it follows that $T_I \propto K_s^R$. This implies that in the photon starvation regime where $K_s \ll 1$ the rate at which frames are transmitted T_I^{-1} is relatively large. For example, for the parameters in Tbls.1, 2, 3, and 4 we have $T_I = 2.2 \text{ s/frame}$, and only 2.2 scientific data bits are represented by each frame on average. When $m=12$ each PPM frame actually represents 12 bits, which we infer represents 2.2 scientific data bits and 9.8 bits of redundancy. This redundancy is exploited by ECC to achieve reliability in the face of a high rate of frame erasures (see §14.3). ECC achieves reliable data recovery by simultaneously mapping a large number of scientific data bits into a large number of PPM frames, thereby statistically averaging over the random frame erasures (see §14.3).

We now give an extended numerical example based on the design relations in Tbl.7 with the goal of more fully appreciating the tradeoffs inherent in a BPPM design. This numerical tradeoff is idealized, neglecting some material degradations in performance from other factors such as transmit aperture and aperture pointing

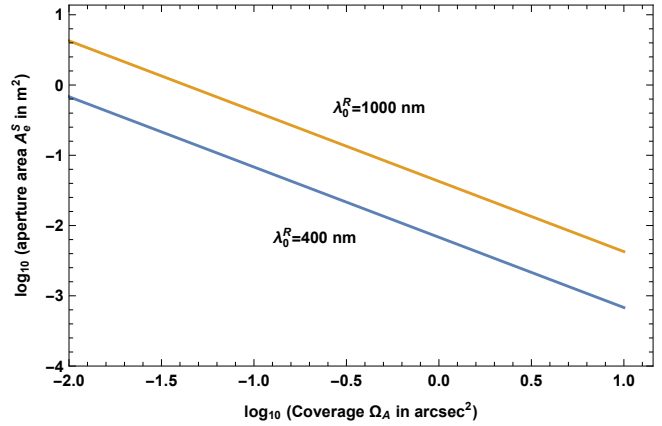


Figure 11. A log plot of the effective area A_e^S of an aperture vs coverage solid angle Ω_A . This assumes an idealized aperture that achieves a uniform sensitivity over Ω_A .

Table 10. Assumed numerical values for background photon rates following a single-mode diffraction-limited aperture.

Radiation source	Units	400 nm	1.0 μm
Point-source interference			
Proxima Centauri Λ_I	ph/s-m ² -Hz	$8.0 \cdot 10^{-10}$	$2.0 \cdot 10^{-7}$
Unresolved sky noise			
Zodiacal light $\Lambda_{N,zodi}$	ph/s-Hz		
90 degrees to ecliptic		$2.0 \cdot 10^{-16}$	$1.0 \cdot 10^{-14}$
Faint-star light $\Lambda_{N,star}$	ph/s-Hz	$2.0 \cdot 10^{-16}$	$1.0 \cdot 10^{-14}$
Atmospheric scattering			
Daylight $\Lambda_{N,sun}$	ph/s-Hz	$4.1 \cdot 10^{-8}$	$5.0 \cdot 10^{-7}$
Fullmoon $\Lambda_{N,moon}$	ph/s-Hz	$1.0 \cdot 10^{-13}$	$1.3 \cdot 10^{-12}$

inaccuracy and atmospheric effects (refraction and turbulence).

10.9.2. Aperture effective area

The area $\log_{10} A_e^S$ is plotted in Fig.11 for two wavelengths of interest as a function of the coverage solid angle Ω_A over the range bracketed by the swarm and single-probe cases in Tbl.3. This tradeoff is straightforward as it does not involve other factors such as background radiation. Choosing a shorter wavelength reduces A_e^S (and therefore aperture sensitivity) for fixed coverage. Increased coverage also reduces aperture sensitivity at a fixed wavelength.

10.9.3. Background radiation

The physical parameters characterizing the noise and interference used in the following numerical calculations are listed in Tbl.10.²⁰ The values given apply to a *sin-*

²⁰ Zodiacal noise is adopted from (Hauser et al. 1998) and the sky noise and star interference are adopted from (Lubin 2020). The atmospheric scattering values are justified in §11.1.

gle aperture in the canonical receive collector of Fig.3, since each aperture has a single optical detector and thus qualifies as a single-mode ‘antenna’ in the sense of §B.21. The units in Tbl.10 are consistent with Tbl.9.

Two wavelengths are compared in Tbl.10, 1 μm (near infrared) and 400 nm (blue visible). The latter is of interest because of the substantially smaller interference from Proxima Centauri, which as a red dwarf star with a power spectrum weighted toward the red. The values in Tbl.10 are typical, but Proxima Centauri is a flare star which exhibits short-term large increases in radiation. These flares will likely contribute to outages (see §11.4), unless the coronagraph factor F_c is considerably smaller than considered here.

The total noise contribution to background radiation during nighttime operation is

$$\Lambda_N = \Lambda_{N,zodi} + \Lambda_{N,stars} + \rho_{moon} \cdot \Lambda_{N,moon}.$$

While $\Lambda_{N,moon}$ assumes a full moon, the factor $0 \leq \rho_{moon} \leq 1$ can adjust for the lower radiance during other phases of the moon. Generally $\Lambda_{N,moon}$ is the dominant sky noise source. Note that assuming $\rho_{moon} < 1$ implies that some nighttime periods (with a brighter moon) are considered outages, and the actual scientific data rate R_a will be correspondingly lower.²²

10.9.4. Daylight outage assumption

As is evident from Tbl.10, daylight would have a major impact on background radiation. For the swarm case in Tbl.3 the transmit power would be impractically large to achieve daylight operation ($P_A^T = 5.8$ kW and $P_P^T = 126$ GW). For this reason, the metrics in Tbl.8 and the following calculations assume nighttime (fullmoon) sky radiance. The value $\rho_{moon} = 1$ in Tbl.3 and the following numerical calculations assume the entire nighttime is a non-outage condition, barring weather events. Since the receiver is aware of day-night and weather conditions, it can force complete erasures during daytime and weather events, and these become outage conditions in the sense of §14.4. Knowledge of the receiver’s day-night or weather conditions is fortunately not necessary at the probe transmitter.

10.9.5. Average transmit power

The average transmit power P_A^T is plotted in Fig.12 as a function of coverage solid angle Ω_A . This shows that the shorter wavelength is quite advantageous, es-

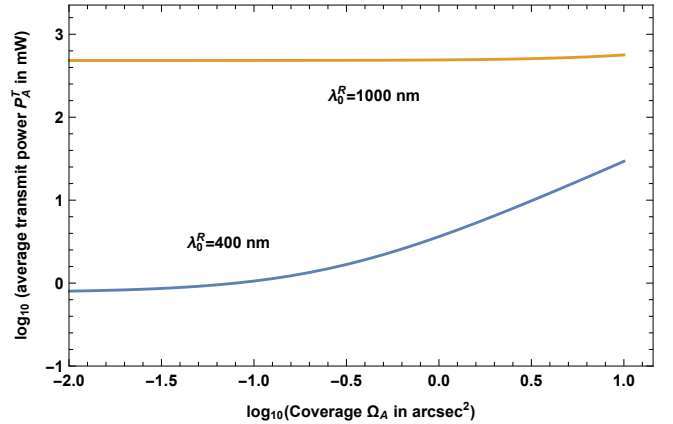


Figure 12. A log plot of the average transmit power P_A^T in mW against the coverage solid angle Ω_A , with all other parameters taken from Tbls.1, 2, 3, and 4. Two wavelengths are plotted, and for small Ω_A the required transmit power is much larger at the longer wavelength due to the greater relative aperture sensitivity to interference and additionally the larger irradiance of a red-dwarf star.

pecially so at smaller coverages (where interference is more significant).

The differing behavior at the two wavelengths can be better understood by comparing three components of SBR: Interference (SIR), noise (SNR), and dark counts (SDR). The smallest component is the dominant source of background radiation. At the shorter wavelength (see Fig.13) Λ_D^S was chosen so that noise and dark counts are equal contributors to background radiation, and hence $\text{SNR} \approx \text{SDR}$ for all coverages (since neither noise nor dark counts are dependent on aperture effective area). Interference is an insignificant contributor compared to moonlight and dark counts at the larger coverages.

At the longer wavelength (see Fig.14) interference becomes the dominant contributor to SBR at all coverages. As a result, the dark count target could be considerably relaxed without a substantial impact on overall performance metrics, but of course that performance would be considerably degraded relative to the shorter wavelength.

10.9.6. Number of apertures

SBR is determined by the design of the aperture and the choice of P_A^T , and remains fixed during the scale-out to the entire receive collector. The purpose of aperture replication in scale-out is to increase the average detected photons per slot K_s^R to the value needed to achieve reliable recovery of scientific data in the face of shot noise. The value of K_s^R and hence the number of apertures N^S does not depend on the data rate \mathcal{R}_0 . The resulting N^S is very large, as plotted in Fig.15.

²¹ This applies even if an optical detector is shared among multiple apertures as described in §5.4 as long as optical interference among apertures is avoided.

²² Strictly speaking when $\rho_{moon} = 0$ there will be some black body atmospheric radiation, but this is neglected since this irradiance is dominated by Zodiacal radiation $\Lambda_{N,zodi}$ from the solar system. This case is also uninteresting since there would be 100% outages.

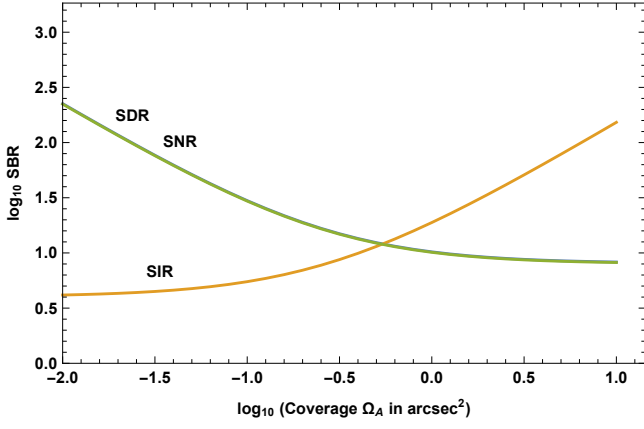


Figure 13. As an aid to understanding the small-coverage behavior exhibited in Fig.12, the log of the three components of $SBR=4$ are plotted vs coverage solid angle Ω_A for $\lambda = 400$ nm. For small coverages SIR is the smallest, and hence interference is the dominant source of background radiation.

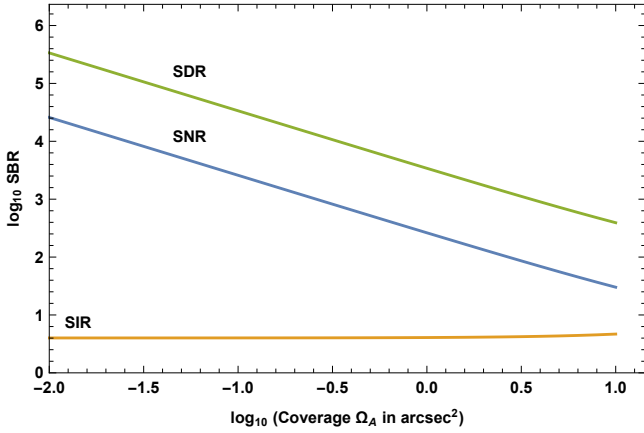


Figure 14. Fig.13 is repeated for $\lambda = 1 \mu\text{m}$. The interference becomes dominant for all coverages.

The metric $N^S A_e^S$, which is a measure of the total effective area across all apertures,²³ is plotted in Fig.16. It is significantly larger at the shorter wavelength, with the compensating benefit that the probe's average transmit power is lower (see Fig.12).

10.9.7. Dark counts

To see the effect of changing dark-count rates, P_A^T is plotted in Fig.17 and Fig.18 as a function of dark counts, coverage angle, and wavelength. This quantifies the obvious conclusion that the shorter wavelength and a very low rate of dark counts are advantageous in achieving

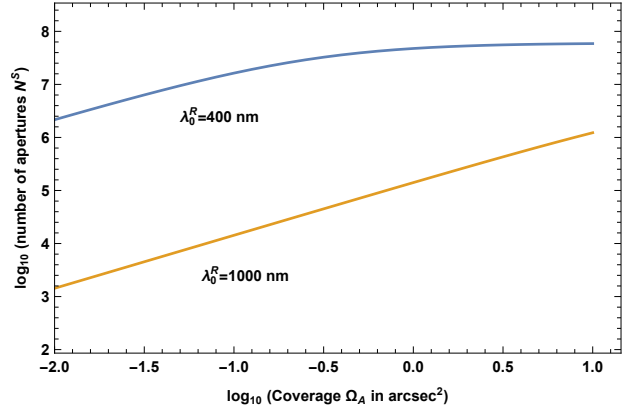


Figure 15. A log plot of the number N^S of apertures under the same conditions as Fig.12. It is significantly larger at the shorter wavelength, which is due to (a) the smaller-area aperture and (b) the smaller peak transmit power P_P^T .

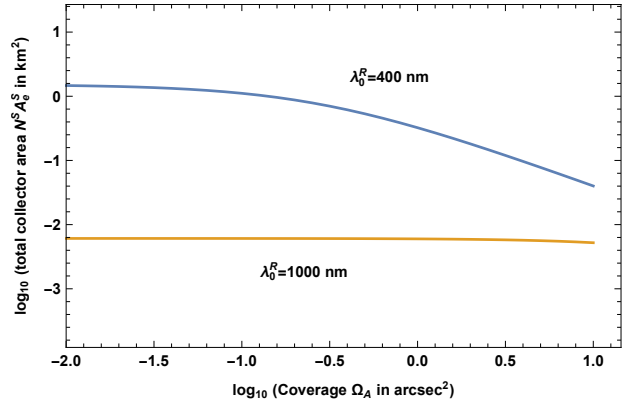


Figure 16. Based on the aperture effective area A_e^S in Fig.11 and the number N^S of apertures in Fig.15, a log-plot of their product $N^S A_e^S$ in km^2 as a function of the coverage. Generally it is less than a km^2 under these ideal conditions, except for very small coverages.

low average transmit power. Reducing the solid angle of coverage is also advantageous.

10.9.8. Coronagraph

The effect of changing the coronagraph rejection is illustrated in Fig.19. The value of F_c makes a substantial difference at low dark count rates because that is where interference dominates.

²³ This is not the effective area of the receive aperture as a whole, which is not defined since the receive aperture is not single-mode and not diffraction-limited.

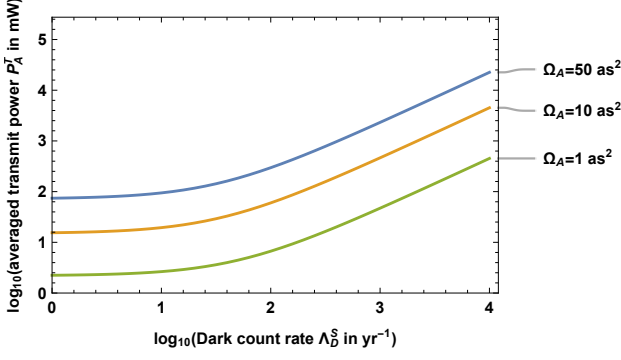


Figure 17. A log-log plot of the average transmit power P_A^T for $\lambda = 400$ nm vs the average dark counts Λ_D^S per year (when referenced to individual aperture optical detectors). Sharing optical detectors across multiple apertures may be helpful in reducing Λ_D^S (see §5.4). Idealized performance is assumed for other physical characteristics like quantum efficiency, pointing accuracy, and atmospheric refraction and turbulence. The different curves illustrate the benefit of reducing the coverage angle. The highest dark count rate $\Lambda_D = 10^4$ yr $^{-1}$ corresponds to 1.14 hr $^{-1}$.

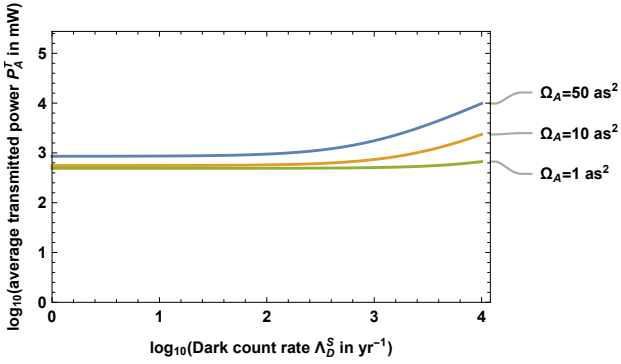


Figure 18. Fig.17 is repeated for $\lambda = 1$ μ m. A floor in transmit power appears because interference becomes the dominant contributor to SBR for small dark count rate Λ_D^S . (see Fig.12 and Fig.14).

10.9.9. Slot time and average transmit power

In BPPM reducing the slot duration parameter T_s reduces the effective dark count rate (by reducing the duty cycle δ). The resulting benefit of T_s on reducing average transmit power P_A^T is illustrated in Fig.20. There is, however, a point of diminishing returns as interference becomes the dominant source of background radiation.

10.9.10. Slot time and peak transmit power

As seen in (9), the peak transmit power P_P^T is not dependent on \mathcal{R}_0 or BPP, but rather is determined by the BPPM parameter T_s and data reliability parameter K_s^R . The effect of T_s on peak transmit power P_P^T is shown in Fig.21. Increasing T_s reduces P_P^T because the pulse energy $P_P^T T_s$ remains relatively fixed. This effect saturates

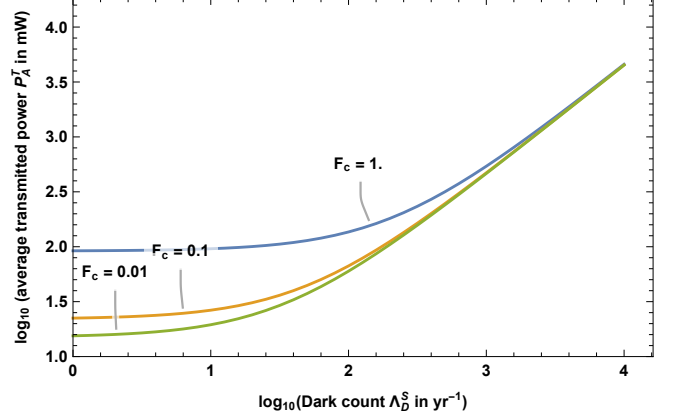


Figure 19. Fig.17 is repeated with three different values for the coronagraph rejection F_c . At low dark count rates the interference becomes the dominant source of background radiation.

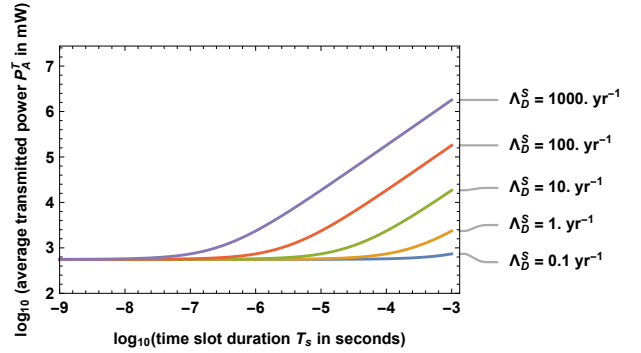


Figure 20. A log-log plot of the average transmit power P_A^T vs slot time T_s (between 1 ns and 1 ms) and different values of dark count rate Λ_D^S in yr $^{-1}$. The largest feasible value (at $\delta=1$) is $T_s=0.98$ ms. Reducing T_s also reduces P_A^T due to its beneficial limiting of dark counts. However, the benefit saturates at small T_s as interference dominates there.

at larger T_s because the increase in P_A^T seen in Fig.20 indirectly offsets any reduction in P_P^T . The peak power increases for smaller T_s (where dark counts have been largely suppressed) because the average power is relatively constant in this interference-dominated regime.

For the other parameters chosen in Fig.21, the best choice of slot time is $T_s \sim 1$ μ s. Any smaller T_s than this and P_P^T increases, and any larger T_s results in an increase in P_A^T . However this tradeoff is influenced by the assumed dark count rate Λ_D^S .

10.9.11. Moonlight variation

The assumed outage probability assumes that the downlink operates during all moon phases. There is an opportunity to reduce the transmit powers if operation is restricted to reduced moonlight by choosing $\rho_{moon} < 1$, but of course the outage probability will also increase. This effect on transmit power is quantified in Fig.22.

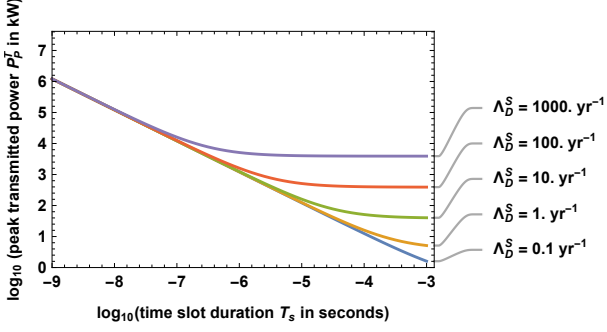


Figure 21. Fig.20 repeated for peak transmitted power P_P^T .

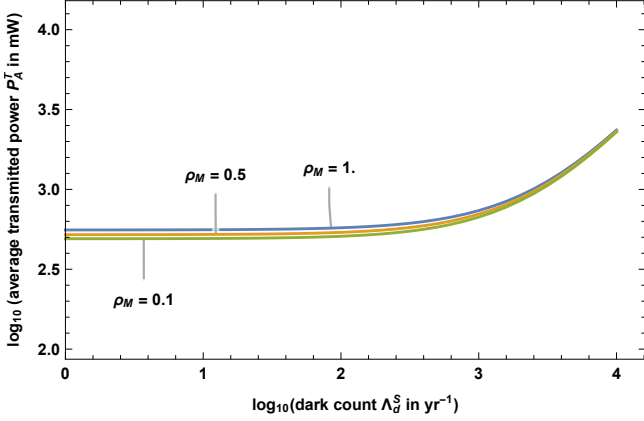


Figure 22. Fig.17 is repeated with all parameters held constant except the maximum moonlight irradiance parameter ρ_{moon} . Note that reducing ρ_{moon} implies a larger outage probability and hence a lower post-outage data rate \mathcal{R}_a . For larger Λ_D^S a smaller ρ_{moon} has little benefit since dark counts are the dominant source of background radiation.

10.9.12. Excess optical bandwidth

If it is necessary for some reason to chose a W_e that is significantly larger than the minimum value T_s^{-1} , the noise and interference (but not dark count) contributions to background at the optical detector are increased. In this event probe transmit power has to be increased to maintain the desired SBR, and dark counts become relatively less important. The effect of increasing W_e on average transmit power P_A^T is plotted in Fig.23.

10.9.13. Quantum efficiency

The preceding results assume ideal quantum efficiency $\eta = 1$. A quantum efficiency $\eta < 1$ has two effects. First it will always increase N^S (and hence total receive aperture size) to achieve the required average photon rate Λ_A^R . Second, it will increase the relative importance of dark counts to SBR, and require an increase in transmit average power P_A^T in the regime of large dark count rates. This latter effect is illustrated in Fig.24.

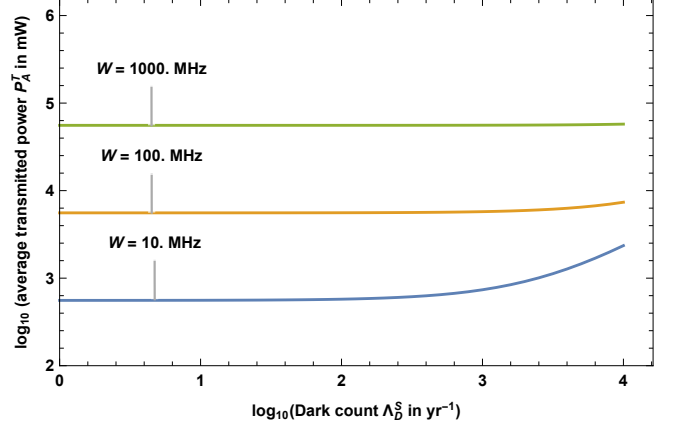


Figure 23. Fig.17 is repeated while varying the receive optical bandpass filter bandwidth W_e and keeping T_s fixed. The minimum is $W_e=10$ MHz corresponds to $W_e T_s = 1$. In the interference-dominated regime the average transmit power is increased (in proportion to W_e), and in principle this could be compensated by a higher coronagraph rejection ratio.

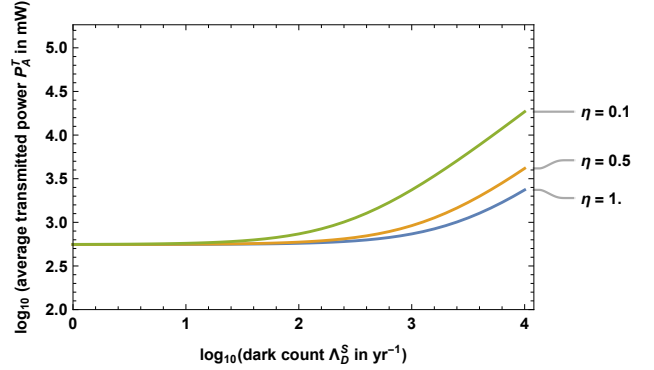


Figure 24. Fig.17 is repeated with all parameters held constant except the optical efficiency η . The average transmit power P_A^T has to be increased to maintain a fixed SBR at higher dark count rates Λ_D^S since received power is reduced but Λ_D^S is unaffected. The adverse impact of η on P_A^T is reduced for very small Λ_D^S since in that regime noise and interference (as well as signal) are reduced and thus SBR is relatively unaffected.

11. ATMOSPHERIC EFFECTS

For a receive aperture located on the earth's surface, the interaction between signal and the earth's atmosphere at optical wavelength introduces several significant impairments (Biswas & Piazzolla 2006). Nighttime sky irradiance is a contributor to the total background radiation, and was incorporated into the numerical results of §10.9. The other significant atmospheric impact is a contribution to outage time due to daytime solar scattering and weather, which together reduce the rate of reliable scientific data recovery (see §10.2 and §14.4).

11.1. Daytime sky irradiance

During the daytime, sunlight scattered through the atmosphere into the receive aperture is a source of background radiation that can be considered isotropic within the coverage of a highly directive aperture. In Tbl.10 the sky irradiance at the aperture can be inferred from Fig.8.16 in (Biswas & Piazzolla 2006):

$$P_N^S = 3 \times 10^{-3} \text{ W}/(\text{cm}^2\text{-sr-}\mu\text{m}) @ \lambda_0^R = 1 \mu\text{m}$$

$$\Lambda_N^S = P_N^S \cdot \frac{\lambda_0^R}{hc} \cdot \frac{W_e(\lambda_0^R)^2}{c} \cdot (\lambda_0^R)^2 \text{ ph/s-Hz}.$$

The factors in the conversion from P_N^S to Λ_N^S are (1) the power to photon rate conversion, (2) the bandwidth expressed in terms of frequency rather than wavelength, and (3) the $A_e \Omega_A$ product given by (B5). The value of P_N^S is about $8 \times$ larger at $\lambda_0 = 400 \text{ nm}$ and a factor of 4×10^5 smaller for a full moon as compared to daylight.

This irradiance decreases with greater angular separation from the sun itself, and it helps that there is a large minimum angular separation between Alpha Centauri and the sun.²⁴ Although the solar radiance is maximum at 475 nm (corresponding to black body radiation at 5800 K), the sky irradiance is smaller at 400 nm than at 1 μ largely due to the smaller value of $A_e \Omega_A$. The resulting numerical values are listed in Tbl.10.

Unfortunately the full daylight sky irradiance in Tbl.10 is more than four orders of magnitude larger than the other sources of noise background. The significance of this depends on the relative intensity of interference and dark counts, but generally operation during daylight hours would require significantly higher probe transmit peak power. Thus in Tbl.3 (as discussed in §10.9.4) we assume that daylight is an outage situation.

11.2. Nighttime sky radiance

If daylight is considered an outage, the sky radiance during nighttime is a limiting factor on the downlink. At night the reflected light from the moon is an indirect source of solar background radiation (except for a new moon or the moon below the horizon). A full moon has a 4×10^5 smaller radiance than the sun. In the absence of moonlight, the primary source of irradiance is thermal emissions from the atmosphere, but this will be considerably smaller than cosmic zodiacal radiation for the wavelengths of interest as long as strong emission lines (such as OH or O₂) are avoided in the choice of wavelength. Thus, the total night sky irradiance as a fraction ρ_{moon} of the full moon value (as determined by the moon's phase) is the approximation employed earlier.

²⁴ In heliocentric coordinates the latitudinal separation is approximately fixed at 44.7 degrees and the longitudinal separation varies through the year.

11.3. Turbulence

Atmospheric turbulence causes a short-term fluctuation in received signal power which is manifested as a scintillation (random variation in signal strength) as well as signal incoherence (wavefront phase aberration across the aperture area). As the geometric size of an aperture increases, the variation in signal power due to scintillation decreases, while the power loss due to spatial incoherence increases (Biswas & Piazzolla 2006).

As the aperture geometry is determined by coverage considerations, scintillation manifests itself as a variation in erasure probability that can only be compensated by considering high erasure probability as an outage, which is mitigated using interleaving and ECC (see §14.4) rather than adjustment of the aperture design.

Spatial incoherence is a less severe impairment during nighttime operation, and under some conditions may be deemed an outage. It can in principle be compensated by adaptive optics (the details are discussed in Sec.3.34 of (Biswas & Piazzolla 2006)). As to whether adaptive optics will be necessary depends on the detailed consideration of elevation, declination, and the geometric size of the aperture (rather than its area), all of which is beyond the scope of this paper. Fortunately, for the larger coverages necessary in the probe-swarm case the aperture is smaller and thus less susceptible to atmospheric turbulence.

11.4. Outages

Periods during which virtually all PPM frames suffer an erasure are considered outages. Generally the transmitter will have no knowledge of when outages occur, but when there is no “fuel” saving from avoiding transmission during outages this has no consequences. The outage mitigation design can assume a worst-case outage probability P_E , with the consequence that the data rate is reduced by a factor of $(1 - P_E)$ (see §14.4).

There are two main sources of atmospheric-origin outages are daylight and weather. Weather, including water vapor, clouds, and storms attenuate or block reception at random times. The statistics of weather outages is highly site-dependent. The receiver is aware of either of these conditions and can enforce (and label) outages by arbitrarily enforcing 100% erasures during these periods.

For any point on earth, nighttime lasts for half the hours averaged over one year (actually slightly less due to refraction of sunlight near the horizon). Near the Antarctic Circle nighttime persists for 48% of the total hours in a year (Wikipedia contributors 2019). Thus treating daylight as an outage would reduce the scientific data rate by 52% at this location.

The siting of the receiver will introduce another source of outages if its latitude results in the target star disappearing below the horizon. In the case of Proxima Cen-

tauri, continuous view is possible if the receiver is sited at a sufficiently southerly latitude²⁵.

A cosmic source of outages will be flares of the target star, but these are short-lived and will be insignificant in terms of outage probability.

12. OTHER CHALLENGING DESIGN ISSUES

BPPM addresses principally the technology limitations of optical bandpass filters and detectors. Other issues relating to the design of the physical layer arise that impose profound technological challenges.

12.1. Probe motion effects

A low-mass probe is assumed to be traveling (relative to the receiver frame) at relativistic speed, and the receiver is also in motion due to earth rotation and orbit. When referred to baseband, due to the short optical wavelength the resulting Doppler shifts must be accounted for in the design (see §A.1).

12.1.1. Uncertainty in probe velocity

At a speed of $u = 0.2c$ the combined Doppler shift (about 20%) and effect of time dilation (about 2%) is about 22%. Since the sources of noise and interference do not experience this shift, the shifted wavelength determines the atmospheric effects and interference from the target star. The transmit wavelength can be adjusted toward a shorter wavelength to compensate for the Doppler shift.

Since the swarm of probes will encompass slightly different speed perturbations, the result is relatively large frequency offsets affecting WDM (see §12.2) and TDM (since a common receive wavelength is assumed). If we allow a perturbation du in speed u , the resulting perturbation $d\nu_R$ in received frequency ν_R is

$$\frac{d\nu_R}{\nu_R} = -\frac{u/c}{1 - (u/c)^2} \cdot \frac{du}{u} = -0.208 \cdot \frac{du}{u} \quad (14)$$

for $u = 0.2c$ (see §A.2). Thus there is a Doppler shift of ± 1.6 THz for each $\pm 1\%$ variation in probe velocity at $\lambda_0 = 400$ nm.

Achieving a precision in probe velocity that limits the Doppler shift to the order of $\sim W_e$ seems unlikely. If probe speed cannot be controlled tightly enough, it will be necessary to compensate for variations in probe speed by a coordinated configuration of transmit wavelength following launch. There are at least two possible options:

- Since the transmission of scientific data follows encounter, transmit wavelength configuration can follow encounter and precede downlink operation. Autonomous configuration of transmit wavelength could be based on a sufficiently precise measurement of time to reach the target star, combined with knowledge of target star position. All probes in a swarm will be affected equally by imprecision in knowledge of this position.
- If there is an earth-to-probe communication uplink for a short period following launch (see §12.5), the received wavelength can be measured at the receiver and used to configure the transmit wavelength.

12.1.2. Earth motion and Doppler

The maximum speed of the earth relative to a heliocentric frame due to its orbit about the sun (or revolution about its axis) is 30 km/s (or 1670 km/h at the equator). The Doppler shift is thus bounded by ± 30 GHz (or ± 464 MHz) at $\lambda = 1$ μm . While this Doppler can be very significant, it is essentially the same for all probes in a swarm and thus does not appreciably affect their relative wavelengths. Accurate positioning of the receiver's optical bandpass filtering does require correction based on accurate knowledge of this motion, and any remaining uncertainty should be accounted for by an increase in bandwidth W_e with the resulting increase in cosmic sources of background radiation (see §10.9.12).

12.1.3. Gravitational red shift

During flyby of the target star, the stronger gravitational field will result in incremental red shift of the probe's signal. While this effect can be significant for a close-in encounter, it is largely avoided with post-encounter commencement of downlink transmission. In any case downlink operation during encounter is unlikely due to conflicting demands on scientific instrument electrical power and probe attitude adjustment to accommodate scientific observations. While gravitational effects are likely insignificant in communications downlink design, they offer a scientific opportunity for sensitive measurement of gravitational potentials (see §A.3).

12.1.4. Influence on data rate

Due to the increasing propagation delay and time dilation in the transmitter clock relative to the receiver, the data rate observed by the receiver is smaller by about 22% than the data rate generated at the transmitter. Due to the methodology adopted in §C, which concentrates on the earth's rest frame, the data volumes and latency plotted in Fig.5 account for this.

²⁵ The declination of Proxima Centauri is -62.67 degrees, so a continuous view is achieved by choosing a receiver site with a latitude more southerly than $(90 - 62.67) = 27.33$ degrees south. However, to avoid significant degradations in link quality when Proxima Centauri is low on the horizon due to increased atmospheric degradation effects, the receiver site should be more southerly than approximately 35 degrees south.

12.1.5. Relativistic aberration

The high speed of the transmitter moving away from the receiver will have a relativistic effect on the transmit beam and affect the link budget of (6). This small incremental effect is not accounted for in this paper.

12.2. Multiplexing options

Multiplexing is the function of separating the concurrent signals originating from different probes. Whether there is a single shared receiver or multiple receivers, this function is challenging due to environmental factors like extremely low received power and frequency shifts due to probe motion.

These challenges are magnified as the number J_p of concurrent transmitting probes increases, yielding strong motivation to minimize J_p . Available measures include, for each probe, limiting transmission during transit and limiting the downlink operating time. We find in §7 that (for a specific set of scaling laws) the optimum downlink time ranges from 2-9 years. For weekly probe launches this results in $J_p \sim 100$ to 500.

There are some alternative multiplexing approaches. The multiplexing method affects many other aspects of the downlink design, so it should be established early.

12.2.1. Spatial-division multiplexing (SDM)

SDM takes advantages of angular differences between probe trajectories to separate the signals from the probes. For probes launched at different times of the year, the parallax variation combined with a drift in the launch targets due to proper motion of the target star will spatially separate trajectories save for short-lived periods of exact coincidence (see §9). This opens up the possibility of choosing a receive aperture coverage to attenuate all probe signals save one of interest, with any coincidences treated as an outage (see §14.4). Proper motion of the target star is particularly helpful for spatial separation, as it opens up the possibility of combining SDM with another scheme for separating the signals from probes with nearby launch dates.

An extreme case is to use a separate receive aperture for each downlink, each with a very small coverage solid angle Ω_A (as implicitly assumed in (Parkin 2019)). Although extravagant in terms of ground-system cost, an important benefit is the reduction in the required transmitter power-area product $\xi_A^T = P_A^T A_e^T$ if N^S is chosen to minimize this value. However, this smaller ξ_A^T may come at the expense of a considerably larger total effective area $N^S A_e^S$ as seen in Fig.16.

An intermediate case would be a more sophisticated single-aperture design that employs time-dependent beamforming to separate probe signals. In effect each aperture would constitute a multiple-pixel receive optical system, with one pixel dedicated to each probe.

12.2.2. Wavelength-division multiplexing (WDM)

In WDM each probe is assigned a different wavelength at the receiver, with an optical bandpass filter and dedicated optical detector servicing each probe. WDM requires precise transmitter wavelength control, which is a challenge complicated by Doppler shifts (see §12.1.1 and §12.1.2) and implementation of a serial bank of optical bandpass filters to separate signal from different probes (see §13.2).

12.2.3. Time-division multiplexing (TDM)

In TDM probe transmissions are assumed to not overlap one another in time at the receiver. Ideally those transmissions are at a common received wavelength, allowing for a single optical bandpass filter and detector. TDM requires precise transmitter knowledge of time of arrival of its signal at earth, which requires in turn a very precise clock and precise knowledge of its own trajectory (see §12.4).

12.2.4. Random-access multiplexing

This is a variation on TDM in which transmissions have a low duty cycle and are randomized so that the probability of overlapping receptions in the receiver is small (Abramson 1994). This may be natural in combination with BPPM, which trades higher peak power for low duty cycle (see §6.2). Collisions at the receiver could be treated in a similar way to outages (see §14.4), although they would complicate the ECC by causing frame errors rather than erasures.

12.2.5. Code-division multiplexing (CDM)

In CDM probes are assigned mutually orthogonal spreading sequences, which allows their signals to be separated (by cross-correlation with the spreading sequences) in spite of both wavelength- and time-overlap. It is useful to think of CDM as maintaining orthogonality using a different orthogonal basis for signals, where the basis functions do not align with either time or frequency (see §13.1.3).

For equivalent per-probe data rates \mathcal{R} , to first order WDM, TDM, and CDM all expand the *total* optical bandwidth by a factor of J_p . In the case of TDM this is because each probe has to transmit at rate $J_p \mathcal{R}$ during its assigned time slot, and for CDM the spreading sequence expands the bandwidth of each probe's signal by a factor of J_p . In practice the bandwidth is larger after accounting for guard bands (WDM) and guard times (TDM) due to imprecise knowledge of wavelength and time at the probes. As illustrated by BPPM, any form of TDM will also increase the peak transmitted power requirement commensurate with J_p .

12.3. Clock accuracy and stability

Particularly at high photon efficiencies, data representation by accurate timing and/or accurate wavelength

will be essential. This represents a significant challenge in a system distributed over interstellar distances where relativistic speeds are involved (see §12.1), and one in which atomic-clock frequency and time standards are not likely to be practical in a low-mass probe transmitter. Along with the generation of high peak-power pulses (see §13.1), the resulting short- and longer-term clock inaccuracies will limit the timing accuracy (as represented by slot time T_s in BPPM) that can be obtained, and thereby will limit the photon efficiency.

There are two related issues of clock synchronization: between probe and receiver, and among aperture clocks which provide timestamps attached to photon-detection events. While apertures co-located on a common site can share a common clock source with atomic accuracy and stability, the probe clock will have relaxed crystal-oscillator accuracy and stability and will be affected by uncertainties in probe speed (see §12.1.1). It will be necessary for the receiver to estimate and track the transmit timing. Fortunately this need not be real-time, but rather can be delegated to a post-processing phase based on the entire record of photon-detection events gathered over the entire mission. The probe can assist in the process by transmitting deterministic sequences of pulses interleaved with the random encoded scientific data. The accuracy of this tracking will be limited by the accuracy with which individual photon detections are time-stamped, and in particular the relative phases of a common clock appearance at each of the apertures.

That relative offset is largely determined by temperature variations, and is on the order of 3 to 10 ns when using the Global Positioning System (GPS) for time-transfer, with larger absolute diurnal and seasonal variations (Lewandowski et al. 1999). It may be possible to track these absolute variations in the post processing, similarly to the probe clock, although the latter is much easier due to its reliance on aggregate (as opposed to per-aperture) photon counts. Greater accuracy and stability may be feasible through a sub-terrainian temperature-controlled optical distribution of clocks not relying on GPS. An absolute accuracy taking into account all sources of variation on the order of 1% of the slot time T_s will be required, placing a lower bound on T_s (and hence dark count rejection). While longer-term stability of the probe clock is less critical, shorter term instabilities will be difficult to track at the receiver due to the low photon-detection rate (even in the aggregate).

12.4. Probe navigation

Relative to an (approximate) inertial frame defined by the Solar System and target star, the probe needs to be self-aware of the time and position for both the probe itself and for earth, for a couple of purposes. First the scientific instrumentation and interpretation of its data requires knowledge of the probe trajectory, hopefully with an accuracy less than a fraction of an AU. Second, accurate pointing of the transmit aperture so

that the maximum signal power reaches the terrestrial receive aperture requires accurate knowledge of the angle and distance of the earth at the later time of arrival (see §12.6).

For these purposes the probe trajectory is parameterized by the probe elapsed time, the observed probe speed, and the observed angle of the sun's and the target star's position. There at least a couple of sources of imprecision in these estimates. First, after 30 yr the variation in elapsed time measured by a probe clock is 16 min for each one part in 10^{-6} variation in oscillator frequency.²⁶ Second, at 4 ly and a nominal speed of $0.2c$ the variation in propagation time is ± 72 days for each $\pm 1\%$ variation in probe speed. Thus a speed variation is generally a much bigger issue in accurate pointing toward an orbiting earth than is clock accuracy. Thus a Xtal oscillator without temperature compensation aboard the probe may suffice for onboard estimate of elapsed time, and whatever method is used for speed measurement and compensation for Doppler shifts (see §12.1.1) also applies to estimating propagation time.

12.5. Feedback Doppler compensation

The multiplexing techniques described in §12.2 require control of the relative wavelength differences among probes in a swarm to an accuracy on the order of the signal optical bandwidth W_e . This is especially true of TDM, since rejection of background radiation puts a premium on minimizing the bandwidth of a receive optical system that is shared among probe downlinks. Since W_e is relatively small, this strongly suggests the use of feedback to control the relative received wavelengths across probe downlinks.

Either the speed of each probe or the transmit wavelength in each probe can be configured using feedback. In both cases a downlink monochromatic beacon can be transmitted during the launch or for a short period following the launch, with its observed Doppler shift on the ground providing an accurate estimate of probe speed. Accurately controlling the final probe speed would require an adjustment to the time window for the directed energy beam. This may also be necessary (or at least helpful) for navigation purposes. Accurately configuring the transmit wavelength to compensate for the actual probe speed following launch would require a telemetry uplink. The latter approach has the disadvantage that the probe requires a communications receiver, although its implications would be minimized by the large available transmit power and the small amount of configuration data required.

²⁶ Relative to terrestrial events the time elapsed on the probe is about 2% shorter than on earth, but this relativistic effect is known accurately and readily compensated.

12.6. Probe attitude control

Attitude control of the probe is required for the scientific mission (orientation of instruments) and for communication (aiming the transmit beam back to its terrestrial communication receiver). The pointing accuracy required for the transmission downlink is undoubtedly the most critical requirement. A three-axis closed-loop correction by photon thrusters driven by the probe electrical power source has been proposed (Lubin 2016).

12.6.1. Probe pointing accuracy

Assumptions as to receive aperture size are predicated on precise aiming of the probe's transmit beam to achieve the maximum power transfer. This is a major issue in solar system probes, and will be here as well. Pointing can be based on probe attitude control or beam angle configuration relative to the probe, or some combination of the two methods.

The angular spreading of the beam is a fraction of the Airy disk, and is thus proportional to λ/d where d is the radius of a circular aperture. Since the target must fall within this beam, indeed near the center, the pointing accuracy is not penalized by the great distance to the earth. The short wavelength λ^R in Tbl.3 reduces the permitted pointing error, while the relative small size of the transmit aperture is helpful. For example, for the parameters in Tbl.3 this ratio $\lambda/d=0.8$ arcsec is much more stringent than 58. arcmin for New Horizons (see Tbl.6) due to the shorter wavelength.

A significant issue is what reference can be used for pointing. Obvious candidates are the sun and the target star (which will fall in nearly the same direction). If the beam were to illuminate the entire solar system, centering it on or near the sun would suffice. However, for the aperture in Tbl.3 the Airy radius becomes 3.27 au at 4.24 ly distance and $\lambda_R = 1 \mu\text{m}$ decreasing to 1.2 au at $\lambda_R = 400 \text{ nm}$. Thus, more specific aim at the position of earth is necessary. One tradeoff would be to reduce A_e^T and increase P_A^T , keeping ξ_A^T constant, thereby reducing the required pointing accuracy at the expense of transmit power. Conversely, a larger transmit aperture (such as that assumed in (Parkin 2019)) would increase the required pointing accuracy accordingly.

It appears likely that the beam must be aimed at the moving position of earth within its orbit at the future date/time of signal arrival, rather than the solar system with the sun near its center. For this purpose a second axis of reference, such as another nearby star, would be necessary. Acquiring the direction of a pair of guide stars requires image sensing with an attitude control loop. Generally the resolution of this sensing has to be finer than the transmit beam width, implying a sensing aperture larger than the transmit aperture. This suggests sharing a single aperture on the probe between transmission and sensing, with a larger portion

of that aperture used for guide star tracking than for transmission.

12.6.2. Attitude control operation

Fortunately a low-mass probe has no moving mechanical parts or fluids that contribute to attitude misalignment, so there are only three identifiable sources of attitude misalignment: motion of electrons within the probe electronics, the momentum recoil from the transmit beam, and (likely most significantly) collisions with interstellar particles. This suggests that attitude adjustment and transmission should *not* occur concurrently, for several reasons:

- If attitude misalignment is infrequent the duty cycle of attitude adjustment may be low.
- The sharing of a common aperture between sensing and transmission is a mass-saving measure that is easier if the two functions are not concurrent.
- Each function can utilize the entire available electrical power, maximizing the data rate and minimizing the time consumed by attitude adjustment.
- During periods of misalignment the data transmission is likely to be unreliable so this becomes an outage condition, whether the probe is transmitting or not.
- Any effect of transmission beam momentum interfering with attitude adjustment is minimized. If thrusters and communications utilize the same electrical source, then downlink transmission exerts an equivalent recoil force on the probe. If transmission occurs only during periods when the attitude is within a tight tolerance, since the probe trajectory is nearly rectilinear the only significant effect is a tiny increase in probe speed.²⁷
- Although the suspension of transmission during periods of attitude adjustment slightly reduces the average data rate, the greater electrical energy available during each transmission can compensate for this with a higher nominal data rate.

12.7. Coronagraph function

The coronagraph function provides extra attenuation for interference originating at the target star (see §10.9.8). Each receive aperture shared over all probe downlinks in a swarm will have a coverage that includes probes just completing their target star encounter, and thus will have limited or no attenuation of the target star radiation. A requirement on the order of $F_c=10^{-2}$

²⁷ The trajectory curvature due to the target star gravitation will introduce a small momentum component transverse to the trajectory that needs to be accounted for.

to 10^{-4} follows (see §10.9.8), necessitating coronagraph-specific measures other than limiting the coverage angle. There are various approaches, some of which are:

- Delay download transmission following encounter long enough for proper motion of the star to separate probe trajectories from the star (Parkin 2019).
- Arrange for an aperture coverage to be limited to a single probe at a time (as assumed in (Parkin 2019)). This is accomplished by duplicating apertures. Or with some forms of TDM, the coverage of a single aperture can be switched to the single probe whose signal is currently being received.
- For a common aperture implemented as a phased array of elements, implement multiple beams directed at the different probes.²⁸ To avoid a reduction in SBR this would have to be accomplished with high quantum efficiency and without amplification.
- Use techniques similar to those being pursued in the direct imaging of exoplanets, which also requires rejection of target-star radiation. These techniques include coronagraphs and interferometers (Traub & Oppenheimer 2010) and external occulters (also known as starshades) (Cash 2011). For example, a notch (high rejection) permanently located at the target star location might be added to the aperture by adjusting the phase/magnitude in the combiner, thus creating a spatial filtering function.

The phase and magnitude in a phased-array combiner has to be implemented extremely accurately. Phases also have to be dynamically adjustable to account for parallax and the proper motion of the star (see §9).

A promising direction draws on advances in direct exoplanet imaging. However, some differences inherent to the downlink design challenge should be noted:

- For a ground-based observation platform, dynamic pointing of the aperture due to atmospheric refraction and turbulence are issues.
- The optical bandwidth is narrow and the wavelength can be chosen to minimize the target star interference (see §10.9.3).
- A single probe downlink will typically operate for years (see §7) and a swarm of probes correspondingly longer.

²⁸ Such an approach is being explored at millimeter wavelengths for application to 5G cellular (Roh et al. 2014).

13. CRITICAL TECHNOLOGIES

The tradeoffs quantified in §10.9 identify three technologies whose stringent requirements play a significant role in success or failure. These are the transmit light source, the receiver optical bandpass filtering, and the photon-counting optical detectors. It is clear that the current state of source and detector technologies is not consistent with the low-mass probe downlink application. Fortunately they can be expected to advance in the application timeframe (see §2.5), but this introduces considerable uncertainty. Fortunately we have not identified any limiting physical principles that impede future advances. Also, the configurable duty cycle δ in BPPM beneficially offers a tradeoff among all three technologies, permitting some flexibility in their relative advancement (see §6.2).

13.1. Transmit light source

In an optical direct-detection communication system employing PPM and BPPM, high peak powers are fundamental to achieving high photon efficiency (Jarzyna et al. 2018). This is reflected in the theoretical limit of (3), which predicts a logarithmic relationship between the achievable BPP with reliable data recovery and PAR. High PAR is achieved by reducing slot time T_s and increasing peak power P_P^T to keep the pulse energy $P_P^T T_s$ constant. This relationship of PAR and BPP is discussed in practical terms in §14. However this straightforward approach results in multiple-kilowatt peak powers (see Fig.21). Optical amplification of semiconductor laser outputs can attain Watt-level peak powers, and Q-switched lasers can attain kilowatt-levels but suffer from low electrical-to-optical conversion efficiency (Banaszek & Jachura 2017).

13.1.1. Design parameter adjustment

The required peak power can be reduced by several adjustments in design parameters singly or in combination, although these unfortunately all trigger other issues. Reducing the coverage solid angle Ω_A benefits the peak power because of the higher sensitivity of a large aperture (see Fig.17), but the total receive collector area is also increased (see Fig.16). Increasing the transmit aperture area A_e^T is effective if the power-area $P_P^T A_e^T$ is fixed. Reducing the dark count rate results in lower peak power (see Fig.21), but the effect is limited by the continued presence of moonlight interference. Smaller peak power can be achieved by reducing the photon efficiency BPP and hence lower PAR (see Fig.9), but this requires very large total receive aperture area to compensate for the reduced efficiency.

13.1.2. Pulse compression

Optical interference can be used in place of emitting high powers directly from an optical source. A straightforward example of this is the ganging of multiple semi-

conductor lasers in the transmitter with an optical combiner. Unfortunately this approach is expected to be inconsistent with the low-mass objective.

Pulse compression technology is often used to generate narrow high-power optical pulses. It relies on the observation that for two pulse shapes $p_1(t)$ and $p_2(t)$ with the same bandwidth W , $p_2(t)$ can be obtained from $p_1(t)$ by a linear filter with transfer function $F(f) = P_2(f)/P_1(f)$, where $P(f)$ is the Fourier transform of $p(t)$. For example, a pulse with constant envelope $|p_1(t)| = A$ and approximate time duration $T \gg 1/W$ can be converted to a pulse p_2 with approximate time-duration $1/W$ and envelope $|p_2(t)| = A\sqrt{WT}$ if energy is conserved.²⁹ This process converts a longer lower-amplitude pulse into a narrower high-amplitude pulse with power gain equal to WT (the bandwidth-time product).

Pulse compression has to be performed in the optical domain, typically by creating targeted interference with arrangements of diffraction gratings (Treacy 1969) or prisms (Kafka & Baer 1987). This apparatus achieves wavelength-dependent group delays to align shorter- and longer-frequency components in time. A *structured receiver* approach has been proposed that uses more complex long-duration waveforms with matched filtering (Guha 2011). Due to the linearity of Maxwell's equations the pulse-compression filtering could be performed in the receiver, reducing the mass burden on the probe. However, while pulse compression works well in generating picosecond pulses, it would be difficult to generate 10 – 100 ns pulses as required in this application. This is because light travels distance of one meter in ~ 3 ns in a vacuum, and such an optical apparatus would necessarily be physically large. Of course shorter pulses could be generated, but the required reduction in pulse duration and attendant increase in peak power would be counter-productive.

13.1.3. Modulation code layer

The need for short pulses can be attributed to the choice of PPM for the modulation code layer, and it is intriguing to consider alternatives. One approach is to extend the code-division multiplexing idea described in §12.2.5 to the modulation coding layer for a single probe downlink.

Consider a set of L waveforms $\{p_i(t), 1 \leq i \leq L\}$, each bandlimited to W Hz and confined to time interval $0 \leq t \leq T$ with the property that

$$\int_{-\infty}^{\infty} p_i(t)p_j^*(t) dt = \begin{cases} A & i = j \\ 0 & i \neq j \end{cases}$$

²⁹ A function bandlimited to W cannot be strictly time-limited, and a function time-limited to T cannot be strictly bandlimited. However these conditions can be approximated if $WT \gg 1$ (Slepian & Pollak 1961). The narrow pulse $p_2(t)$ violates this condition and will be only roughly confined to time duration $1/W$.

This requirement can be approximately satisfied whenever $L \leq WT$, with increasing accuracy as $WT \rightarrow \infty$ (Slepian & Pollak 1961).

The modulation coding layer can transmit one of the L waveforms, and at the receiver a parallel set of filters (one matched to each possible waveform) can estimate which waveform was transmitted (Banaszek et al. 2019a). A PPM modulation code is a special case of this scheme with $L = M \sim W_e T$, where M is the number of slots in a PPM frame, and frequency-shift keying (FSK) is another. FSK and other options could intrinsically allow the light source to generate a waveform with constant power with duration T (rather than duration T/M as in PPM). However, there is a major disadvantage, and this is the need for L optical detectors, one for each matched filter, multiplying the total dark count rate accordingly. PPM has the unique property that a single optical photon-counting detector (with its dark counts) is needed.

Intermediate cases are possible. For example if $M = I \cdot J$ then each candidate transmitted pulse could be confined to one of I time slots (each with duration T/I) and one of J frequencies. Only $J < M$ optical detectors would be needed.

13.2. Optical bandpass filtering

Bandpass filtering in the optical domain is a critical system component with several requirements that are challenging to achieve individually and collectively. Numerical results in §10.9.9 suggest a BPPM slot time $T_s \sim 0.1 - 1 \mu\text{s}$, which implies $W_e \sim 1 - 10$ MHz. An optical bandwidth W_e larger than necessary results in larger cosmic source of background (see §10.9.12). At $\lambda = 1 \mu\text{m}$, $W_e = 1$ MHz results in a Q-factor (ratio of center frequency to bandwidth) of 3×10^8 . Such Q's are being approached with recent technology.³⁰

There are other requirements on the bandpass filtering. If WDM is used to separate the probe signals (see §12.2.2) we actually need a bank of bandpass filters with nearly adjacent passbands. To avoid signal attenuation, this filter bank has to be serial rather than parallel, with each filter splitting off the optical signal in one band while providing low insertion loss outside this designated passband. Further, the location of these passbands have to be agile to adjust to changing Doppler shift due to the earth's motion (see §12.1.2) and possibly also to adjust for variations in the probe transmit wavelengths (see §12.1.1).

13.3. Optical single-photon detectors

The numerical results point to the need for optical detectors with dark count rates that are extremely low (see §10.9.7). Superconducting detectors, which can success-

³⁰ For example cavity-based high-Q optical bandpass filters with $Q = 8 \times 10^7$ are reported in (Spencer et al. 2014, 2012).

fully detect individual photons and have intrinsically low dark count rates, will be necessary.

Dark-count rates of $\Lambda_D=10^{-4}$ Hz have been reported for a superconducting nanowire detector (Shibata et al. 2015). This is two orders of magnitude higher than the objective of Tbl.3, which translates to $\Lambda_D^S=10^{-6}$ Hz. In (Shibata et al. 2015) the black body radiation from the connecting optics is reported as the major source of dark counts, and this source is substantively different than intrinsic dark counts in the detector itself since the dark count rate is proportional to optical bandwidth in the former and independent of bandwidth in the latter. Low dark count rates were obtained by inserting a cold 100 GHz bandpass filter between optics and the nanowire. However, the signal optical bandwidth in Tbl.3 is four orders of magnitude lower than this, opening an opportunity to further reduce the optics blackbody radiation.

In fact there is an opportunity to locate all the receiver optical bandpass filtering at the output of the optics and input of the optical detector. In this case the dark count rate originating as blackbody radiation in the optics would be comparable between PPM and FSK, since the total bandwidth W_e for the two modulation schemes are nominally equal (see §13.1.3). This example illustrates the intimate relationship between the design of the modulation coding and physical constraints and characteristics.

Superconducting detectors are intrinsically free of dark counts, but material impurities and external sources of radiation (radioactive decay and cosmic rays) may be an issue. Some other measures can be taken to minimize the dark-count rate, including the following ideas:

- Cryogenic cooling of the optics and other photonic elements.
- Better shielding of optics and detectors from external radiation.
- Many intrinsic dark counts may be manifested by out-of-band (higher-energy) photons, and these events may be recognizable in the electrical pulse amplitude at the detector output.
- Share a single optical detector over multiple apertures, reducing the per-aperture dark count rate accordingly (see §5.4). For example multiple fibers might be attached to a large-area detector. These fibers may need to be optically isolated, or this may be unnecessary at the extremely low photon detection rates expected.
- It is also feasible to operate with $SBR < 1$, although the theoretical photon efficiency falls off rapidly as SBR decreases in this regime. While this would allow for greater dark count rates, all else equal, it would have other negative consequences.

14. DATA RELIABILITY

Scientific data, especially after aggressive compression, must be recovered with very high reliability to maintain the integrity of scientific conclusions and outcomes. Achieving this high reliability in the face of impairments like noise and interference, atmospheric turbulence, and outages is a challenge. In the interest of a smaller receive aperture we seek high photon efficiency BPP (see §10.5.2), and this magnifies the challenge. Even after the aforementioned impairments are tamed, signal shot noise (a feature of the laws of quantum mechanics) places theoretical limits on the BPP that can be achieved consistent with reliable data recovery. Here we discuss this issue from an intuitive perspective intended to be accessible to those not versed in communication and information theory, with technical details relegated to Appendices.

14.1. Reliability is the hard part

There is no theoretical limit on photon efficiency if reliability is not demanded. The challenge is in *actually achieving* high reliability in the recovery of scientific data in spite of high photon efficiency. This is easily illustrated using the encoding scheme of PPM, one frame of which was illustrated in Fig.4c. The reliability challenge comes about because even with K_s^R average detected photons for each occupied slot (one out of M), the actual number of photons is *random*. This is a manifestation of the signal shot noise.

Assuming no spurious photon detections from background radiation (this would be another source of randomness to overcome), let the number of detected photons Y in time interval T_s be a random variable, which quantum mechanics predicts has a Poisson distribution. If the slot in question is the one containing non-zero average power, and the average number of detected photons in this slot is $E[Y] = K_s^R$, then

$$\Pr \{Y = k\} = \frac{(K_s^R)^k e^{-K_s^R}}{k!}. \quad (15)$$

An erasure occurs in a PPM frame when no photons are detected in all M slots, and this erasure has to be mitigated by ECC. Based on (15), this event $Y = 0$ occurs with probability $\Pr \{Y = 0\} = e^{-K_s^R}$.

Since one PPM frame communicates $\log_2 M$ bits using an average of K_s^R detected photons, the photon efficiency is

$$\text{BPP} = \frac{\log_2 M}{K_s^R} = \frac{m}{K_s^R}. \quad (16)$$

Obviously $\text{BPP} \rightarrow \infty$ as $K_s^R \rightarrow 0$, so achieving a large BPP is not an issue. The problem arises when we consider reliability, since a side effect of reducing K_s^R is $\Pr \{Y = 0\} \rightarrow 1$ as $K_s^R \rightarrow 0$, and thus a large and increasing fraction of PPM frames are erased. Even $K_s^R = 1$ in the absence of ECC would result in unacceptable reliability, since in that case an erasure occurs

in 37% of PPM frames on average, which is not suitable for scientific data.³¹ A more acceptable erasure probability of $e^{-K_s^R} \approx 10^{-7}$ can be obtained with $K_s^R=16$, but this would result in $\text{BPP} < 1$ for practical values of m .

Conceptually we can achieve high BPP (albeit in an impractical way) by manipulating m . For any value of K_s^R , even a larger value like $K_s^R=16$, (16) indicates that any arbitrarily large BPP can be achieved by choosing m sufficiently large, because this conveys an increasing number of bits at the expenditure of a fixed number K_s^R average photon detections. However, this quickly becomes impractical due to a vanishing small slot duration T_s . For example, if we choose the typical values of $\text{BPP}=10$ and $K_s^R=16$, then we infer from (16) that $m=160$ is required. To achieve a data rate of $\mathcal{R}_0=1$ b/s with conventional PPM we must map 160 data bits into a PPM frame with duration 160 seconds, requiring a slot time of

$$T_s = \frac{160 \text{ s}}{2^{160}} \approx 10^{-34} \text{ ps}, \quad (17)$$

which is, needless to say, far beyond the capability of our electronics.

Although impractical, improving BPP by increasing m does uncover an important principle. Namely, a way to achieve high photon efficiency coincident with high reliability is to increase the PAR (and consequently the bandwidth) of the signal. This is suggested by the theoretical limit of (3) as well. This principle applies at both radio and optical wavelengths.³² We now illustrate how efficiency and reliability can be achieved in a practical way by greatly moderating the bandwidth requirement.

14.2. Modulation and coding architecture

The theoretical bound of (3) suggests that $\text{PAR} \sim 2^{10}$ is necessary to achieve $\text{BPP} \sim 10$ b/ph, a value dramatically lower than would ever be achievable by using a ‘raw’ PPM frame to communicate our data as in (16). A practical architecture achieving this lower PAR is shown in Fig.25. It is organized into layers, with each layer split between coordinated functionality in the transmitter and receiver. This architecture, in conjunction with specific choices for the modulation code and error-correction code (ECC) is not only theoretically solid, but $\text{BPP}=13$ has been achieved in bench testing (Farr et al. 2013).

The physical layer involves all the physical elements of the downlink, including optical source and detector and transmit and receive apertures. Its input is an intensity-

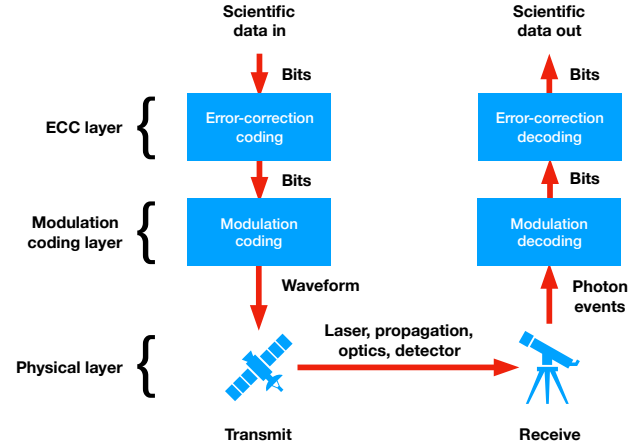


Figure 25. Coordinated transmit-receive communications architecture. Functionality is divided into three layers, with each layer divided into a transmit and receive component. Logically each layer in the transmitter is coordinated with its counterpart in the receiver.

vs-time waveform, and its output is a sequence of photon detection events.

The role of the modulation coding layer is to represent discrete data by a continuous-time intensity waveform at the transmitter, and interpret the resulting photon events observed in the receiver in terms of the transmit data (but with poor reliability). For our purposes our modulation code is described by BPPM in Fig.4, which consists of a sequence of PPM frames, each frame representing $\log_2 M$ bits of data. This simple scheme, operating in conjunction with the ECC layer, allows us to achieve high photon efficiency BPP with high reliability in data recovery.

14.3. ECC layer

In contrast to the approach taken in §14.1, the way to achieve a large BPP is to operate the modulation code layer with very poor reliability; that is, choose a small value for K_s^R (see (18)), which is a photon-starvation mode. The value $K_s^R=0.2$ chosen in Tbl.3 results in a frame erasure probability $e^{-0.2}=0.82$, so approximately 82% of frames are lost to erasures. Although this choice may seem arbitrary, it is further justified in §14.3.4.

The role of the ECC layer is to reconstruct a highly reliable replica of the scientific data. In order to dramatically improve the reliability, the ECC coding layer in the transmitter adds redundancy to the scientific data. In the receiver the ECC decoding layer makes use of this added redundancy (the precise structure of which is known to the receiver) to reconstruct a replica of the scientific data with dramatically improved reliability.

The principle behind the ECC layer can be described abstractly as follows. For $\text{BPP}=10.9$ bits/ph in Tbl.3, each scientific data bit recovery is based on an aver-

³¹ In the physics literature one occasionally sees an analysis of PPM with $Y \equiv 1$, claiming a deterministic number of detected photons and a large resulting value of BPP (see (Hippke 2017) for an example). This analysis is not valid because it neglects the stochastic nature of quantum photon detection, which at $K_s^R = 1$ results in an unacceptably large erasure probability.

³² For the radio case, where the channel model is quite different, this principle is described and quantified in (Messerschmitt 2015).

age of 0.092 photon detection events. A way (the only way) to achieve reliability in photon-starvation mode is to recover multiple data bits based on a commensurate large number of photon detections, exploiting the law of large numbers to yield less random variability in the number of photon detection events. This can still be accomplished in the context of a PPM modulation coding layer by representing the data bits by pulses with duration T_s . Thus BPP=10.9 might actually be achieved by exchanging an average of 100 detected photons for 1090 bits. At a data rate of $\mathcal{R}=1$ b/s this implies an average of 100 photon detection events within 1090 sec (18 minutes), or (almost) equivalently 100 detected pulses on average. There must be $2^{1090}(\sim 10^{328})$ distinguishable patterns of pulses, one pattern for each possible combination of 1090 bits (compare this to the $\sim 10^{80}$ atoms in the visible universe). The error-correction decoder examines the random pattern of actual detected pulses, and infers the most likely pattern, and hence the most likely combination of 1090 bits that were represented in the transmitter.

14.3.1. *Small codebook example*

More concretely, ECC in the context of a PPM modulation coding layer associates $k > 1$ bits with a group of $l > 1$ PPM frames, each having $M = 2^m$ slots. The set of 2^k frame groupings (one for each set of k inputs bits) is called a *codebook*. Since these l PPM frames could in principle represent as many as lm bits, not all the possibilities are included in the codebook as long as $k < lm$. This is what we mean by *redundancy*, which can result in dramatically improved reliability by circumventing erasures that have occurred.

This concrete description of the ECC layer can be illustrated as in Fig.26 for three very simple examples. In Fig.26(a) $k = 1$ bits (2 codewords) are represented in a codebook of $l = 1$ PPM frame with $M = 2$ slots, in (b) $k = 2$ bits (4 codewords) are represented in a codebook of $l = 2$ PPM frames with $M = 4$ slots, and in (c) $k = 4$ bits (16 codewords) are represented in a codebook of $l = 4$ PPM frames with $M = 4$ slots. The redundancy in the three cases is zero for (a) and 0.5 for (b) and (c). If the transmit energy per PPM frame remains fixed, the average detected photons per frame has the same value K_s^R for all cases. Thus, the photon efficiency has the same value ($\text{BPP} = 1/K_s^R$) for all three cases, and thus the probability of a single erasure remains the same.

In Fig.26(a) and (b) all possible erasure events are enumerated (for brevity this is omitted in (c)). In (b) the input data can be inferred even with a single erasure, and data is lost only if there are two erasures. In (c) each pair of codewords agree in at most one PPM frame but disagree in at least three, so one or two erasures (out of a possible four) result in no data loss. We can easily calculate the probability of these events, with the result that for $K_s = 12$ ($\text{BPP} = 0.083$ b/ph) the probability of data loss is 6.1×10^{-6} for (a), 3.8×10^{-11} for (b), and

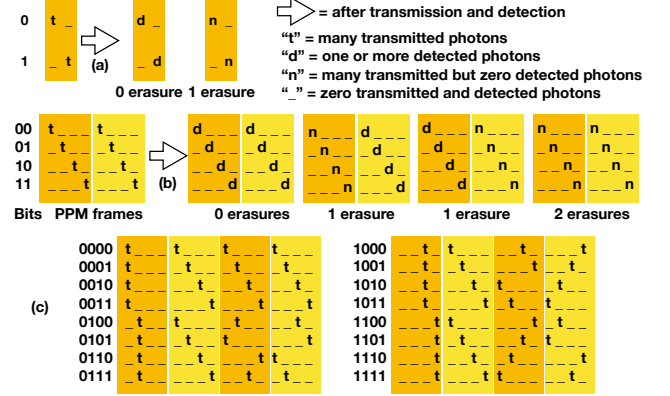


Figure 26. An example of the benefits of error-correction coding (ECC) to improve the data-recovery reliability in conjunction with pulse-position modulation (PPM). (a) One scientific data bit is mapped into a single PPM frame with $M = 2$ slots. The effect of an erasure is shown. (b) Two data bits are mapped into a pair of PPM frames, each with $M = 4$ slots. The three possible erasure scenarios are shown. (c) Four data bits are mapped into four PPM frames, each with $M = 4$ slots. Erasure scenarios are not shown. While the photon efficiency is the same in (a), (b), and (c), mapping a larger number of data bits into a larger number of frames results in improved immunity to erasures.

9.3×10^{-16} for (c). The reliability improves dramatically. Increasing the size of the codebook can be beneficial, as in this example, because without any change in BPP the data recovery becomes less susceptible to frame erasures.

14.3.2. *Theoretical constraint*

The photon efficiency for the codebooks displayed in Fig.26 are nowhere near the $\text{BPP}=10.9$ b/ph that we are seeking. One of the central results of information theory is that under certain conditions the existence of a sequence of ever-larger codebooks is guaranteed, with the desirable property that the probability of data loss decreases to zero. In particular, for the parameters BPP, K_s^R and M the condition is (see §F)

$$\text{BPP} < \frac{1 - e^{-K_s^R}}{K_s^R} \cdot \log_2 M < \log_2 M. \quad (18)$$

This is consistent with theoretical bound on (3) presented earlier.³³ This confirms the significance of photon-starvation mode, because BPP in (18) approaches (3) as $K_s^R \rightarrow 0$ and thus we must choose a very small value of K_s^R to achieve a BPP near the theoretical maximum for the chosen m .

³³ The value of BPP assumed in Tbl.7 and in the numerical calculations of §10.9 assume equality in (18). This is recognizably optimistic, but something close to this should be achievable in practice with an appropriate design of ECC accompanied by large processing resources in the receiver.

14.3.3. Role of redundancy

We are assured by (18) that photon starvation isn't detrimental to data reliability, as long as ECC overcomes the inherent unreliability at the modulation coding layer. The explanation for this is the inherent redundancy. The average rate of photon detections is \mathcal{R}/BPP , and with K_s^R average photons per PPM frame, the rate of PPM frames is $\mathcal{R}/K_s^R \cdot \text{BPP}$. Thus the "raw" bit rate at the input to the modulation coding layer is

$$\frac{m \cdot \mathcal{R}}{K_s^R \cdot \text{BPP}} = \frac{12 \cdot 1}{0.2 \cdot 10.9} = 5.5 \text{ b/s}.$$

Thus, 4.5 b/s of this "raw" bit rate is redundancy, and 1 b/s is scientific data (82 % redundancy and 18% scientific data). According to (18), this redundancy offers a sufficient opportunity to overcome the frequent erasures in PPM frames suffered in the modulation coding layer.

While the theory backing up (18) strongly suggests that a very large ECC codebook is required to obtain high BPP, we have to fall back on best practices in actually choosing such a codebook. For a high SBR, high reliability can be obtained (Farr et al. 2013) using Reed-Solomon coding (Wicker & Bhargava 1999), which is well suited to overcoming frequent erasures.³⁴ At lower values of SBR more advanced and modern coding techniques have to be adopted, a topic beyond the scope of this paper.

14.3.4. Quantum limit

The question arises as to the degree to which the architecture of Fig.25 and the specific choice of PPM for the modulation coding limits performance. Theoretical limits on photon efficiency BPP with reliable data recovery are identified in the Appendices:

- Any physical layer that makes use of electromagnetic transmission is governed by a fundamental quantum limit on reliable data recovery (see §D). This limit is expressed in terms of the photon density PPD (the average number of photons per dimension). There has been some exploration of technologies that may be able to approach this limit (Banaszek et al. 2019b).
- Any physical layer that modulates optical power in the transmitter and performs direct detection (photon counting) in the receiver has, at high SBR, a theoretical limit on BPP with reliable data recovery defined by (3) (see §E).
- The limit of (18) comes arbitrarily close to the photon-counting limit as $K_s \rightarrow 0$ (see §F).

³⁴ For a laboratory demonstration of high BPP in reliable optical communications, see (Farr et al. 2013). There are also tutorial papers (Messerschmitt 2008) and textbooks (Cover & Thomas 1991; Gallager 2008) that expand on the theoretical basis of ECC.

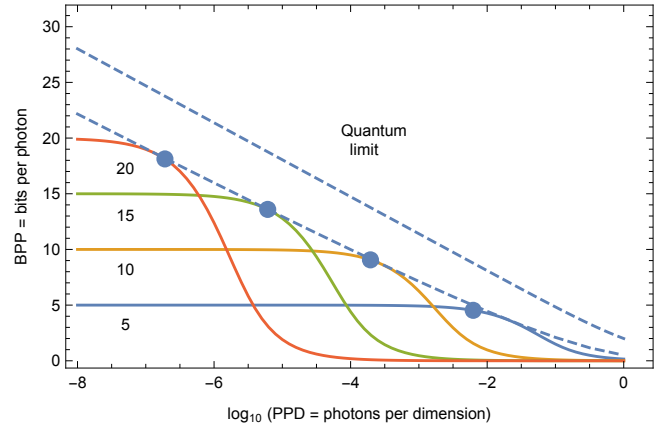


Figure 27. A plot of the photon efficiency BPP at the theoretical limit of reliable data recovery (see §F). BPP is plotted against $\log_{10}(\text{PPD})$, where PPD is the photon density (average photons per dimension). For PPM we have $\text{PPD} = K_s/M$, and PPD is manipulated by varying K_s . The different curves are for the values $m \in \{5, 10, 15, 20\}$, where the number of slots per PPM frame is $M = 2^m$. The bottom dashed curve is the largest BPP that can be achieved by PPM (by optimizing the value of m for each PPD) and the upper dashed curve is the quantum limit on reliable data recovery. The dots correspond to $K_s = 0.2$, the nominal value chosen in Tbl.3, which is nearly BPP-maximizing for the m -range of interest. This displays the gap between PPM and the quantum limit, which shrinks for larger PPD. This gap captures the maximum increase in BPP that may be feasible with future technologies that achieve a more sophisticated manipulation of quantum states.

The shortfall of PPM (and hence photon-counting more generally) to the quantum limit is plotted in Fig.27 (this applies to BPPM equally well). The quantum limit is expressed in terms of PPD, the average photons per dimension, so the BPP for PPM is plotted against the same metric for different values of m . The specific values of $\{\text{PPD}, \text{BPP}\}$ for $K_s = 0.2$ are identified by dots, which fall near the maximum BPP achievable, thus justifying this assumption in Tbl.3 and the previous numerical results.

As m increases in Fig.27, BPP increases as predicted in (3), since for PPM we have $\text{PAR} = M$. The largest BPP achievable by PPM is plotted as the lower dashed curve. Our nominal value $K_s = 0.2$ approximates this optimum choice. If a larger BPP is desired, it is preferable to increase m rather than further reduce K_s .

14.4. Outage mitigation

Outages are characterized by erasures which are not due to signal shot noise, but rather environmental factors experienced by a terrestrial-based receiver such as sunlight and weather. The data loss due to outages will inevitably reduce the rate at which scientific data is communicated reliably immediately following encounter to

$\mathcal{R}_a < \mathcal{R}_0$. A simplistic approach to overcoming outages would be to repeat the transmission of scientific data multiple times. We want \mathcal{R}_a to be as large as feasible, and fortunately there are far more efficient outage mitigation techniques based on a modification to the modulation coding and ECC layers in Fig.25. We can demonstrate theoretical upper limits on \mathcal{R}_a for a particular statistical model of fully random outages, modify the modulation coding layer to approximate this model, and choose ECC codebooks which come close to these theoretical limits.

14.4.1. *Outage characteristics*

Outages manifested as frame erasures (rather than frame errors) are simpler to deal with (see §6.2 for the distinction), and since the receiver is aware of daylight and weather conditions it can enforce outages-as-erasures by simply ignoring the received signal during periods of questionable SBR. In this case the receiver will experience daylight and weather outages as contiguous bursts of PPM frame erasures. This distinguishes outage erasures from shot-noise erasures, which are temporally completely random.

14.4.2. *Modification to modulation coding layer*

In principle the increase in erasure frequency due to outages can be overcome by choosing a more powerful form of ECC. In practice, however, it is very difficult for ECC to deal effectively with temporally highly correlated erasures. Fortunately this challenge can be overcome by adding interleaving to the modulation coding layer as shown in Fig.28a. The interleaver in the transmitter scrambles the order of the bits in the input bit stream, and the de-interleaver in the receiver reverses that operation to recover the original ordering.³⁵ The modulation-layer decoder outputs a stream of symbols with three possible values $\{0, 1, E\}$, where 'E' indicates that this bit is unknown because it experienced an erasure (it was one of m bits in an erased PPM frame). Whether this erasure was due to shot noise (with probability e^{-K_s}) or outages (with probability P_W for weather and P_D for daylight) cannot be inferred by the PPM decoder, but nevertheless the knowledge of which bits have suffered an erasure is helpful in the subsequent error-correction decoding.

The interleaver utilizes a deterministic but pseudo-random algorithm with the goal of destroying the correlation of the erasures and make them appear to occur randomly and independently (like a sequence of flips of a biased coin). This requires a 'depth' of interleaving that is larger than the correlation scale of the frame erasures, which implies longer than the longest outage period (the

³⁵ Operating the interleaving and de-interleaving at the bit-level simplifies the following analytical argument. In practice the interleaving may be performed at the PPM frame level.

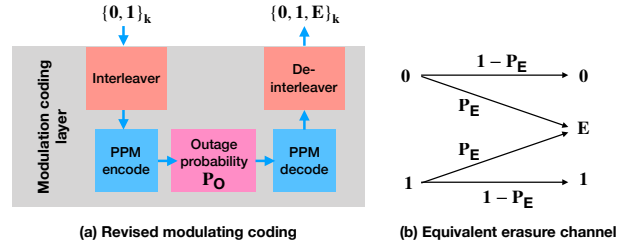


Figure 28. Modification to the PPM modulation code layer which converts it to a binary erasure channel. (a) Bit-level interleaving and coordinated de-interleaving convert grouped erasures ‘E’ (due to shot noise, daylight, weather, etc.) into an equal number of pseudo-randomly distributed erasures. The PPM coding/decoding introduces erasures due to shot noise, while the transmission introduces additional erasures due to outages with probability P_W . (b) Single bit erasure channel with erasure probability P_E , with transition probabilities P_E and $1 - P_E$. Due to interleaving we assume that successive channel uses are statistically independent.

longest credible weather-outage event). Nominally the number of erasures per error-correction codeword then obeys a binomial probability distribution which is identical for all codewords, yielding a more effective and efficient ECC.

14.4.3. *Modification to ECC layer*

It is argued in §F.1 that the detected photons per frame K_s^R and rate of PPM frames T_I^{-1} should not be changed with the addition of outages. Rather, the reliability of data recovery is theoretically preserved in the presence of outages if the input scientific data rate is reduced from its nominal \mathcal{R}_0 by a factor of $(1 - P_W)(1 - P_D)$. That is, the data rate is reduced on average by the fraction of PPM frames that are correctly decoded, which is intuitively the best we could hope for.

Since K_s should not be changed in response to outages, neither should $P_P^T A_e^T T_s$, A_e^S or N^S . Assuming that T_I is also not changed, neither is the average transmit power P_A^T . The sole effect of a reduction in data rate to $\mathcal{R}_a < \mathcal{R}_0$ is an increase in the redundancy in the ECC in order to maintain fixed data-recovery reliability in the face of the added erasures due to outages. Since the data rate is lowered without a reduction in average power, an unsurprising side effect is to reduce the photon efficiency BPP by the same factor. Fortunately this has no practical impact for a continuous electrical power source not based on fuel consumption.

If rate \mathcal{R}_a is unacceptably small, it can always be increased by choosing a larger \mathcal{R}_0 . This of course will have implications throughout the design such as increased average power, increased duty cycle with an attendant increase in the impact of dark counts, etc.

15. CONCLUSIONS

The design of a communication downlink from low-mass interstellar probes is extremely challenging. While the downlink violates no laws of physics and appears to be feasible in theory, the challenge arises when the characteristics of available technologies are taken into account. Innovation and invention in both system concepts and in the constituent technologies will be needed.

The primary areas of necessary technology development identified in this paper are:

- Low-mass light sources achieving high peak powers possibly combined with optical pulse compression technology in either transmitter or receiver.
- Low-mass transmit aperture and coordinated attitude adjustment and pointing with sufficient accuracy.
- A feasible multi-probe multiplexing scheme taking into account inaccuracies in the knowledge of time and speed and distance, including Doppler shift.
- Approaches to a near-earth uplink for configuration of transmit wavelength.
- Optical aperture possibly incorporating adaptive optics to counter atmospheric turbulence, achieving uniform sensitivity over a relatively large non-circular coverage angle, and with sufficient coronagraph rejection of target star radiation.
- Optical bandpass filters with sufficiently narrow bandwidth, and with agility and configuration capability to accommodate multi-probe multiplexing and uncertainties in Doppler shift.
- Receive optics and optical detectors with very low dark count rates, with possibly detector sharing over multiple apertures.
- Low-mass and low-power processing to realize the requisite compression and error-correction coding on board the probe.

This paper can serve as a roadmap to further investigation and research, and the ultimate outcome depends on the success of those efforts.

ACKNOWLEDGEMENTS

PML gratefully acknowledges funding from NASA NIAC NNX15AL91G and NASA NIAC NNX16AL32G for the NASA Starlight program and the NASA California Space Grant NASA NNX10AT93H, a generous gift from the Emmett and Gladys W. Technology Fund, as well as support from the Breakthrough Foundation for its Breakthrough StarShot program. More details on the NASA Starlight program can be found at www.deepspace.ucsb.edu/Starlight.

APPENDIX

A. RELATIVISTIC EFFECTS

Since a low-mass probe travels at relativistic speed, relativistic effects enter.

A.1. Transmitter and receiver motion

Assume an inertial frame S (one approximating a heliocentric coordinate system is convenient). Relative to the trajectory of a photon from probe to receiver, the probe and receiver have a longitudinal component of velocity and a small transverse component (which is neglected). Let the longitudinal components for the probe and a receiver relative to S be u_p and u_r respectively. The relationship between transmitted wavelength λ_T (observed in the rest frame of the transmitter) and received wavelength λ_R (observed in the rest frame of the

receiver) is³⁶

$$\xi = \frac{\lambda_R}{\lambda_T} = \frac{\nu_T}{\nu_R} = e(u_p, -1) \cdot e(u_r, +1) \quad (\text{A1})$$

$$e(u, \rho) = \frac{1 - \rho u/c}{\sqrt{1 - u^2/c^2}}. \quad (\text{A2})$$

Thus ξ is the product of four factors, each of which models a distinct physical effect. The two numerators account for Doppler shifts due to changing propagation delay, while the two denominators model the relativistic time dilations of the transmit and receive clocks. Nearly desired λ_R can be achieved by adjustment of λ_T to compensate for the first factor, while smaller variations in u_p and u_r have to be accounted for in other ways (see §12.1.1 and §12.1.2).

³⁶ This relation, including the product law, is derived in (Messerschmitt 2017). Note however that Eq. (17) of that reference is incorrect except at $\rho = \pm 1$, with the corrected value given by (A2).

A.1.1. Probe speed

The systematic red shift due to the nominal probe speed $u_p = 0.2c$ results in $\xi = 1.22$ (or a 22% shift). This should be compensated by an adjustment in λ_T . Since the energy of each photon is $E = hc/\lambda_R$, the energy of each photon at the receiver is lower than at the probe. Energy seen by an observer in S is conserved, including this photon energy loss and kinetic energy gains for the probe (the recoil effect) and receiver (photon absorption) (Macleod 2004). The probe transmitter thus acts as a photon engine which continually increases u_p by a tiny amount. From the perspective of the receive signal, the motion affects wavelength and not photon count, and thus has no effect on the data rate \mathcal{R} obtainable by a direct-detection receiver.

A.2. Uncertainty in probe speed

Assuming that $u_r = 0$, based on (A1), any uncertainty in probe speed u_p relates directly to an uncertainty in received frequency ν_R . Differentiating the relation $\xi\nu_R = \nu_T$ with respect to u_p , we get

$$\xi \cdot \frac{d\nu_R}{du_p} + \nu_R \cdot \frac{d\xi}{du_p} = 0. \quad (\text{A3})$$

Eq.(14) follows from substituting (A2) in (A3).

A.3. Gravitational potential effects

There are small gravitational effects on the optical communications photons due to the gravitation potential in the target stellar system as well as our solar system. Gravitational effects on the probe cause it to speed up as it approaches the target and slow down after encounter. The photons leaving the spacecraft before it passes the target undergo a gravitation redshift as it climbs out of the target system potential back to the Earth and a gravitational blueshift as they enter our solar system and are detected at the Earth or nearby (lunar base etc). For photons emitted after the target encounter there will additional effects that need to be included due to the infall and exiting of the photons as they pass the vicinity of the target system.

This potential modifies the photon energy and hence the frequency in proportion to the integrated difference in gravitational potential divided by c^2 or one-half the ratio of the Schwarzschild radius divided by distance to object (star, planet etc). With an extremely narrow linewidth (bandwidth) of the transmit laser gravitational potential may be detectable, offering an opportunity for extremely sensitive measurements of gravitational potential. For example, with a transmit laser linewidth of 10 KHz at 300 THz a fractional frequency offset $3 \cdot 10^{-11}$ may be observable. This is of course modified by the modulation and dependent on the laser technology. For comparison the Schwarzschild radius of our Sun is about 3 km and at a distance of 1 AU ($1.5 \cdot 10^8$ km) this yields a gravitational shift relative to infinity of

$1 \cdot 10^{-8}$. While small compared to the relevant Doppler shifts due to velocity effects, it is still $300 \times$ larger than the fractional laser linewidth. Even the gravitational potential of the Earth is relevant (Schwarzschild radius 9 mm with physical radius of $6.4 \cdot 10^6$ m yielding shift $8 \cdot 10^{-10}$).

B. ANTENNAS

Certain fundamental principles of antennas or apertures for electromagnetic communication illuminate both opportunities and constraints on our downlink. Our interest here is only in theory that applies to an aperture, which is where the coverage and the SBR are determined. Our aperture is assumed to be a diffraction-limited optical aperture with a single optical detector, which is essentially a single-pixel optical telescope. Our receive aperture as a whole is *not* diffraction-limited (it has multiple detectors, and radiation adds incoherently), so the following principles do not apply. However, the coverage and SBR determined at the aperture level are preserved in the scale-out to N apertures (see §5.2.1).

B.1. Principles

As a consequence of Maxwell's model of electromagnetism, the *reciprocity theorem* states that when one antenna is used for transmission and another for reception, their roles can be reversed without any change to the outcome (see Appendix D of (Wilson et al. 2009)). It is often easier to analyze an antenna in transmit mode, even if it is to be used in receive mode, or *vice versa*.

Suppose a plane wave at wavelength λ and equivalent frequency ν has specific intensity \mathcal{I}_ν as a function of frequency ν , defined as the flux (power per cross-sectional area) per frequency interval (Burke & Graham-Smith 2009). The corresponding intensity in frequency interval $d\nu$ is $\mathcal{I}_\nu \cdot d\nu$. Since the bandwidths of interest are very small for interstellar communication (to eliminate most noise and interference), it is convenient to use ν and recognize that any variation in λ can usually be neglected. Thus we assume a fixed wavelength $\lambda = \lambda_R$, and simultaneously (and somewhat inconsistently) allow ν to vary over a bandwidth W_e .

For astronomical sources, which can often be considered as isotropic emitters (at least over a finite range of directions of interest) it is often more convenient to use the specific brightness \mathcal{B}_ν , which is the power per unit solid angle per frequency interval. At great distances a spherically expanding wave (as from a point source) can be considered a plane wave at the antenna (as long as the difference between a plane and a sphere is a small fraction of a wavelength). In that case, for a spherical wave at a distance D from the source, the conversion from specific brightness to specific intensity is $\mathcal{I}_\nu = \mathcal{B}_\nu / D^2$.

B.2. Effective area and gain

When a plane wave with specific intensity \mathcal{I}_ν impinges on an antenna, we can measure the specific total power P_ν delivered to an impedance-matched termination (at radio wavelengths) or an ideal optical detector (at optical wavelengths). The *effective area* of the antenna is defined as $A_e = P_\nu/\mathcal{I}_\nu$, which has the units of area. A_e usually depends strongly on the angle of incidence, and any dependence on ν can often be neglected over a small bandwidth W_e .

Often we are interested in the maximum value of A_e for the antenna's preferred direction (its "pointing" or "main beam"). For an aperture with geometric area A_g , in general $A_e \leq A_g$ with equality when the aperture is diffraction-limited and the direction of propagation of the plane wave is aligned with the pointing.

An isotropic radiator does not favor one direction over another. Its specific brightness \mathcal{B}_ν is constant in all directions. For a lossless isotropic radiator and lossless (free-space) propagation, by conservation of energy $4\pi\mathcal{B}_\nu = P_\nu$.

The radiation pattern of an antenna of interest is conveniently specified by the ratio of its specific brightness in a particular direction to that of an isotropic radiator with the same power input. This value $G = 4\pi\mathcal{B}_\nu/P_\nu$ is the *directivity* or *gain* of the antenna in that direction.³⁷ For a lossless diffraction-limited antenna, P_ν equals \mathcal{B}_ν integrated over all directions, so

$$P_\nu = \iint \mathcal{B}_\nu \cdot d\Omega \quad \text{or} \quad \frac{1}{4\pi} \iint G \cdot d\Omega = 1. \quad (\text{B4})$$

In words, the gain of any antenna averaged over all solid angles is unity, and identical to the gain of an isotropic radiator in any direction.

It follows from the laws of thermodynamics (Wilson et al. 2009) that for some particular direction, for an antenna with gain G and effective area A_e in that direction,

$$G = \frac{4\pi A_e}{\lambda_R^2} \quad (\text{B5})$$

Thus the gain of an antenna (a mostly transmission characteristic) is proportional to effective area (a mostly reception characteristic) expressed in wavelengths. It follows that for an isotropic radiator $A_e = \lambda_R^2/4\pi$ in all directions.

B.3. Highly directive antennas

For optical communications and astronomy we are interested in highly directive antennas. Consider an ideal directive antenna that in transmit mode concentrates all its flux uniformly across solid angle Ω_A (called its main

beam), and there is zero flux outside this solid angle of coverage. Such an antenna is diffraction-limited when the phase shift from optical source to free-space is fixed for all angles within Ω_A . Such an antenna used in receive mode has a fixed effective area A_e for any direction within the main beam. Note that the main beam area need not be circular for this to hold (this is important in our aperture application).

Then based on (B4) the gain of this antenna is $G = 4\pi/\Omega_A$, and substituting into (B5)

$$A_e \Omega_A = \lambda_R^2. \quad (\text{B6})$$

The solid angle covered by this ideal main beam is inversely proportional to effective area, the latter expressed in units of wavelength. As expected, directive antennas with a larger effective area are more directive. This idealized result can be approximated for a practical directive antenna, which introduces sidelobes due to diffraction.

B.4. Aperture response to different sources

The specific power P_ν delivered to a matched termination or absorbent surface by a lossless diffraction-limited aperture is now evaluated for the types of radiation sources of interest in interstellar communication.

B.4.1. Interference

Interference from the target star can be approximated as an isotropic point source with constant specific brightness \mathcal{B}_ν at all angles. To a receive antenna at great distance D_0 from the target star this will appear as a plane wave with specific intensity $\mathcal{I}_\nu = \mathcal{B}_\nu/D^2$ and thus

$$P_\nu = A_e \mathcal{I}_\nu = A_e \cdot \frac{\mathcal{B}_\nu}{D^2} \quad (\text{B7})$$

for a receive antenna with effective area A_e in the direction of the interferer.

B.4.2. Probe transmitter

For communications, the optical bandwidth W_e will always be at least as large as the signal bandwidth. Thus it is more appropriate to leave out the 'specific' in intensity, brightness, and power, and model the total power over all frequencies. At distance D the average receive power P_A^S in a lossless antenna (aperture) with effective area A_e^S is

$$P_A^S = \frac{P_A^T}{4\pi} \cdot \frac{4\pi A_e^T}{\lambda_T^2} \cdot \frac{1}{D^2} \cdot A_e^S = \frac{A_e^T A_e^S P_A^T}{\lambda_T^2 D^2} \quad (\text{B8})$$

for transmit antenna with average transmit power P_A^T and effective area A_e^T , confirming (5). The four product terms in (B8) are (1) the brightness of the transmitter if its radiation were isotropic, (2) the transmit antenna gain, (3) the translation from brightness to intensity at the receiver, and (4) the receive aperture equivalent area

³⁷ Directivity refers to an ideal antenna, while gain takes any losses in the antenna structure into account. Here we assume an ideal lossless antenna so there is no distinction.

(which converts intensity to power). This is the well-known Friis transmission equation (Schelkunoff & Friis 1952).

Although the transmit and receive wavelengths λ_T and λ_R differ substantially due to Doppler shift (see §A.1), P_R in (B8) is not dependent on λ_R .

B.4.3. Noise

Finally consider noise due to unresolved sources of radiation. From the perspective of the receive antenna, we can consider this to be an isotropic source of radiation. In practice the radiation is never fully isotropic, because it is limited in extent (like Zodiacal radiation in a distant solar system) or is not fully visible to a terrestrial antenna (due to occlusion by the ground). However, if the antenna is highly directional, and its coverage coincides with radiation that is well approximated as uniform with direction, then the isotropic model should be accurate.

Isotropic radiation has constant specific brightness \mathcal{B}_ν . For an antenna with gain G as a function of direction, the received power is

$$P_\nu = \iint G \mathcal{B}_\nu \cdot d\Omega = \mathcal{B}_\nu \cdot \iint G \cdot d\Omega = 4\pi \mathcal{B}_\nu \quad (\text{B9})$$

making use of (B4). The received specific power is independent of the antenna effective area. This is why we can meaningfully speak of a CMB ‘noise temperature’ at microwave frequencies without referring to A_e^S .

A couple of special cases are of interest. First, if the isotropic specific brightness \mathcal{B}_ν were actually generated by an isotropic radiator with power P_ν , then we know that $G \equiv 1$ and $\mathcal{B}_\nu = P_\nu/4\pi$ consistent with (B9). Second, if a highly directive antenna receives isotropic radiation, then (B9) becomes

$$P_\nu = \iint_{\Omega_A} \frac{4\pi}{\Omega_A} \cdot \mathcal{B}_\nu \cdot d\Omega = 4\pi \mathcal{B}_\nu. \quad (\text{B10})$$

In this case P_ν is independent of Ω_A (and hence effective area A_e) because the total noise power due to the size of the main beam and the gain within that main beam precisely offset.

An alternative interpretation of this last observation is that the received power is proportional to A_e^S (the conversion factor of input flux to power at the detector) and also Ω_A (the fraction of total isotropic power reaching the detector) (see Eq. (8.76) of (Biswas & Piazzolla 2006)). This product $A_e^S \Omega_A$ is constant for a diffraction-limited highly directive antenna (based on (B6)).

C. DATA VOLUME VS. LATENCY

Let D_0 be the distance to the target star and $D > D_0$ the distance to the probe. The total latency (elapsed time since launch) for data transmitted from distance D is

$$T_L = D \left(\frac{1}{u_0} + \frac{1}{c} \right) \quad (\text{C11})$$

for fixed probe speed u_0 . The terms in (C11) are respectively the elapsed time t for the probe to reach distance D , and a photon emitted at distance D to return to the receiver, both measured relative to the rest frame of the receiver.

The appropriate data rate \mathcal{R} for purposes of data volume is the transmitted data rate (11). The total data volume transmitted between distance D_0 and D is

$$\mathcal{V} = \int_{D_0/u}^{D/u} \mathcal{R}(\zeta, u_0 t) dt = \frac{\mathcal{R}_0 D_0}{u_0} \cdot \left(1 - \frac{D_0}{D} \right). \quad (\text{C12})$$

This entire \mathcal{V} is decoded at the receiver during time duration T_L . Eliminating D from (C11) and (C12), the latency can be expressed directly in terms of the volume,

$$T_L = \frac{D_0}{u_0} + \frac{D_0 \mathcal{V}}{D_0 \mathcal{R}_0 - u_0 \mathcal{V}} + \frac{D_0^2 \mathcal{R}_0}{c(D_0 \mathcal{R}_0 - u_0 \mathcal{V})} \quad (\text{C13})$$

where the three terms are the transit time, the transmission time, and the return propagation time all expressed in terms of an earth-based clock. After substituting for \mathcal{R}_0 and u_0 in terms of ζ (see §7), this latency can be minimized over the choice of ζ .

For any \mathcal{R}_0 , \mathcal{V} approaches a finite asymptote $\mathcal{V} \rightarrow \mathcal{R}_0 D_0 / u_0$ as $D \rightarrow \infty$. This ultimate limit on volume with infinite latency is due to the decreasing data rate with distance. Larger \mathcal{R}_0 and a smaller u_0 help to increase \mathcal{V} , the latter effect due to the slower D -related falloff in \mathcal{R} .

There will also be a small reduction in available electrical power during transmission (due for example the half life of a radioactive source), and this is not taken into account in (C12).

D. QUANTUM LIMIT ON DATA RELIABILITY

The actual design of a concrete ECC for the photon-counting channel will not be pursued here, because ECC design is itself an extensive and sophisticated project. Nevertheless it is important to determine how large a BPP consistent with reliable data recovery might be expected, and also quantify how larger BPP relates to larger PAR and bandwidth W_e because those two parameters interact strongly with other aspects of the downlink design.

D.1. Channel model

A given physical configuration is not generally associated with a theoretical limit on the data rate \mathcal{R} , because we must also specify other details of the physical layer such as aperture sizes and detection method before such a limit can be established. Any theoretical limit is associated with a specific *statistical channel model*, which specifies, for each possible input (typically a continuous-time or discrete time signal), a probability distribution of the output. Here we find it useful to address three such models: the quantum limit (see §D.3),

direct-detection of light (see §E), and direct-detection in conjunction with a PPM modulation layer (see §F).

D.2. Channel capacity

Communication theory offers a way to establish a theoretical limit on the photon efficiency BPP which can be achieved consistent with reliable data recovery through the concept of *channel capacity* \mathcal{C} . Channel capacity can be calculated (using statistical techniques beyond our scope) for any specific channel model. A channel model can be discrete-time or continuous time, with any combination of discrete or continuous inputs or outputs. Channel capacity does *not* place a limit on the data rates that can be achieved (see §14.1). What it does reveal is a theoretical limit on what data rate \mathcal{R} can be achieved with arbitrarily high reliability, applying to the specific channel model in question. The associated photon efficiency is easily inferred from $\text{BPP} = \mathcal{C} / \Lambda_A^R$. In particular, capacity reveals that:

- For any $\mathcal{R} < \mathcal{C}$, a modulation code and ECC is guaranteed to exist that can achieve data rate R in conjunction with any arbitrarily stringent reliability requirement. Channel capacity does not reveal any concrete way to achieve $\mathcal{R} \rightarrow \mathcal{C}$, as that is an entirely separate issue.³⁸
- The existence of capacity does not preclude $\mathcal{R} \geq \mathcal{C}$ for some concrete implementation, for arbitrarily large \mathcal{R} . However it asserts that high reliability cannot be achieved at such data rates. Generally the highest achievable reliability will deteriorate as \mathcal{R} increases.

Capacity is very useful as a tool in the preliminary design of a communication link because it represents an ideal to shoot for; that is, what BPP is possible for reliable data transmission. Also it tells us, for any concrete implementation, how much further improvement may be possible with the application of additional effort and resources.

D.3. Holevo capacity

For optical communications, the most general channel model assumes that the transmitter and receiver can manipulate an arbitrarily large number of quantum states directly and simultaneously. The resulting *Holevo capacity* establishes a technology-independent theoretical limit on the data rate that can be achieved with reliable data recovery (Holevo 1998). Since we cannot avoid the randomness inherent in quantum mechanics in any physically meaningful way, Holevo capacity represents an ultimate and theoretical limit to aspire to, and

³⁸ Based on decades of research it is generally possible to narrow the gap between \mathcal{R} and \mathcal{C} , although attempting to do so may be impractical (due to complexity, storage and processing overhead, PAR, bandwidth, etc.)

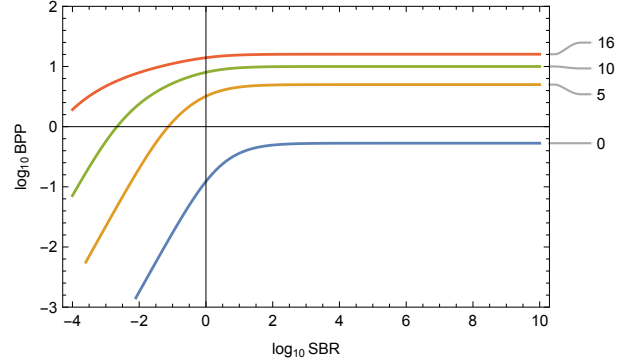


Figure 29. For a continuous-time photon-counting channel, a log-log plot of BPP vs SBR with the different curves corresponding to different values of PAR. The curves are labeled by $\log_2 \text{PAR}$, so for example 16 corresponds to $\text{PAR} = 2^{16} = 65,536$. The axis $\log_{10} \text{BPP} = 0$ corresponds to a photon efficiency of 1 b/ph. The axis $\log_{10} \text{SBR} = 0$ corresponds to equal average signal and background power.

reveals what future progress may be feasible with new technologies not available to us today. Recent research is making some inroads in approaching the Holevo limit (Guha 2011).

PPM makes use of a repeated transmission of PPM frames, each composed of M timeslots of duration T_s . Thus it uses temporal modes only (avoiding the use of wavelength, spatial, and polarization modes to convey information). For a fair comparison with Holevo capacity we also limit the Holevo capacity to temporal quantum modes making use of timeslots with the same duration T_s . Then for average power Λ_A^R the average photon count per timeslot is $\text{PPD} = T_s \Lambda_A^R$. The photon efficiency BPP at the Holevo quantum limit is then (Dolinar et al. 2012a)

$$\text{BPP} = (1 + 1/\text{PPD}) \cdot \log_2(\text{PPD} + 1) - \log_2(\text{PPD}). \quad (\text{D14})$$

Of course this must be greater than either the BPP achievable by a direct-detection receiver (see §E) or PPM (see §F). This applies in the absence of background radiation, which suffices for our purposes.

E. THEORETICAL LIMITS ON DIRECT DETECTION

A practical channel model for today’s technology is modulation of optical intensity in the transmitter and direct detection of photons in the receiver.

E.1. Constraints

If we allow infinite transmit power, any data rate \mathcal{R} can be achieved reliably. To get practically meaningful results, we must place constraints on the received power. Assume that the intensity (average photons per second) over a finite interval T_c is $\Lambda_n(t)$, which we can think of as a codeword. These are the peak power Λ_P^R and

average power Λ_A^R constraints

$$0 \leq \Lambda_n(t) \leq \Lambda_P^R, \quad 0 \leq t \leq T_c$$

$$\frac{1}{T_c} \int_0^{T_c} \Lambda_n(t) \cdot dt = \Lambda_A^R, \quad 1 \leq n \leq N_c.$$

We make two simplifying assumptions which have no effect on the capacity \mathcal{C} . First, each and every codeword is constrained to have the same energy $T_c \Lambda_A^R$. Also, every codeword has an ON-OFF character ($\Lambda_n(t) = \Lambda_P^R$ or $\Lambda_n(t) = 0$ for $0 \leq t \leq T_c$). Photon rates $\{\Lambda_A^R, \Lambda_P^R\}$ are referenced to the detector output, taking account of everything that happens in the physical layer (including quantum efficiency). Also assume that there is a fixed background rate Λ_B , and define $\text{PAR} = \Lambda_P^R / \Lambda_A^R$ and $\text{SBR} = \Lambda_A^R / \Lambda_B$.

E.2. Capacity result

The direct-detection channel is modeled by photon detection events governed by Poisson arrival statistics. This is the most random arrival process, in which inter-arrival times are statistically independent and obey an exponential distribution. The capacity has been determined for this statistical model under the peak and average power constraints described in §E.1. Define two parameters

$$s = \frac{1}{\text{PAR} \cdot \text{SBR}}, \quad q = \min \left\{ \frac{1}{\text{PAR}}, \frac{(1+s)^{1+s}}{e s^s} - s \right\},$$

and then (Wyner 1988)

$$\frac{\mathcal{C}}{\Lambda_A^R} = \text{BPP} = \text{PAR} \cdot \log_2 \frac{(1+s)^{q(1+s)} s^{(1-q)s}}{(q+s)^{q+s}}. \quad (\text{E15})$$

In the limit as $\text{SBR} \rightarrow \infty$ (or equivalently $s \rightarrow 0$), (E15) simplifies to (yielding (3) for $\text{PAR} > e$)

$$\begin{aligned} \text{BPP} &\rightarrow -\text{PAR} \cdot q \log_2 q \\ q &\rightarrow \min \{1/\text{PAR}, 1/e\}. \end{aligned} \quad (\text{E16})$$

E.3. BPP is unbounded

Notably the capacity \mathcal{C} is unbounded even for finite average power,

$$\text{BPP} \rightarrow \infty \text{ as } \text{PAR} \rightarrow \infty \text{ for any } \text{SBR} < \infty. \quad (\text{E17})$$

This confirms that a PAR constraint is necessary to prevent infinite BPP, and more importantly indicates that increasing Λ_P^R increases BPP and \mathcal{C} even as Λ_A^R is held constant. The uncertainty principle will intervene at very high PAR (Butman et al. 1982; Hippke 2018) to render our channel model physically unrealizable.

E.4. Effect of background radiation

A log-log plot of BPP vs SBR is shown in Fig.29 over a wide range (14 orders of magnitude) of SBR. The value

of BPP is nearly constant with the value (3) for large SBR. In the region of low SBR, the highest achievable BPP falls off rapidly. This is clearly a region to be avoided by choosing a sufficiently large transmit power P_A^T . Notably even in the regime of low SBR, the background can still be overcome by choosing a sufficiently large PAR.

F. THEORETICAL LIMITS ON PULSE-POSITION MODULATION

Constraining the implementation to the concrete architecture of Fig.25 must necessarily reduce the capacity relative to the direct detection model of §E, which does not constrain the modulation code in any way. We can ascertain the adverse effect of choosing a particular modulation code by associating a new bits-in to bits-out channel model with the modulation code-in to modulation code-out. In the case of PPM this new channel model has bits-in and bits-plus-erasures-out, with an erasure probability e^{-K_s} . The resulting theoretical limit on reliable data recovery is well known to be (18) (Butman et al. 1982).

One distinction between PPM and the assumptions behind the Holevo capacity is that the K_s average photons are all isolated in a single timeslot per frame rather than allowed to fall in the available dimensions in any pattern. The other distinction is the direct manipulation of quantum states allowed in Holevo, which lacks a practical realization in today's technology.

F.1. Effect of outages

The idea of using a de-interleaver to randomize the temporal statistics of outages was introduced in Fig.28a, and for theoretical convenience assumes that erasures occur at the bit level (although in practice they may well occur at the PPM frame level). An ideal *erasure channel* is pictured in Fig.28b. It models a statistical relationship between input bits $\{0, 1\}$ and output symbols $\{0, 1, E\}$ in terms of a set of transition probabilities, where P_E is the probability of a single bit-level erasure (which equals the probability of a PPM frame erasure). Further, it is assumed that the individual symbols in Fig.28b are statistically independent, a condition that is strongly violated with PPM frame erasures or outages, but that a well-designed interleaver can approximate.

The capacity C_u of the ideal erasure channel of Fig.28b is well known to be $C_u = (1 - P_E)$ per channel use, or

$$C_u = (1 - P_E) = (1 - e^{-K_s}) \cdot (1 - P_W) \cdot (1 - P_D)$$

where K_s is the average detected photons per PPM frame. This assumes that the three sources of erasures (shot noise, weather, and daylight) are statistically independent. Weather outages and daylight may be correlated, in which case C_u can be adjusted accordingly.

The rate of channel uses in Fig.28b as a model for Fig.28a is m/T_I , and thus the capacity of the modulation coding layer is mC_u/T_I . Relative to the case

of no outages, this capacity is reduced by a factor of $(1 - P_W)(1 - P_D)$, and thus the data rate \mathcal{R}_0 has to be reduced by the same factor to ensure that reliable data recovery remains possible. Since the average photon detection rate is K_s/T_I , the upper bound on BPP is changed to

$$\text{BPP} < m \cdot (1 - P_W) \cdot (1 - P_D) \cdot \frac{1 - e^{-K_s}}{K_s}. \quad (\text{F18})$$

This is consistent with (18) for the case $P_W = P_D = 0$. As in the outage-free case, for a fixed value of m the

greatest photon efficiency is obtained as $K_s \rightarrow 0$, and there is no motivation to modify K_s to account for outages.

The foregoing is a theoretical limit on C_u and BPP. For any specific choice of a class of error-correction codes (such as the Reed-Solomon codes), it is appropriate to minimize the error rate by the choice of K_s and T_I taking into account the characteristics of this particular code. In this context there may be some dependence of K_s on P_W and P_D .

REFERENCES

- Abramson, N. 1994, Proceedings of the IEEE, 82, 1360
- Atwater, H., Davoyan, A., Ilic, O., et al. 2018, Nature Materials, 1, doi: [10.1038/s41563-018-0075-8](https://doi.org/10.1038/s41563-018-0075-8)
- Banaszek, K., & Jachura, M. 2017, in 2017 IEEE International Conference on Space Optical Systems and Applications (ICSOS) (IEEE), 34–37, doi: [10.1109/ICSOS.2017.8357208](https://doi.org/10.1109/ICSOS.2017.8357208)
- Banaszek, K., Jachura, M., & Wasilewski, W. 2019a, in International Conference on Space Optics, Vol. 11180, International Society for Optics and Photonics, 111805X, doi: [10.1117/12.2289653](https://doi.org/10.1117/12.2289653)
- Banaszek, K., Kunz, L., Jarzyna, M., & Jachura, M. 2019b, in Free-Space Laser Communications XXXI, Vol. 10910 (International Society for Optics and Photonics), 109100A, doi: [10.1117/12.2506963](https://doi.org/10.1117/12.2506963)
- Biswas, A., & Piazzolla, S. 2006, The atmospheric channel, ed. H. Hemmati (John Wiley and Sons)
- Burke, B., & Graham-Smith, F. 2009, An introduction to radio astronomy (Cambridge University Press), doi: [10.1017/CBO9780511801310](https://doi.org/10.1017/CBO9780511801310)
- Butman, S., Katz, J., & Lesh, J. 1982, IEEE Transactions on Communications, 30, 1262, doi: [10.1109/TCOM.1982.1095577](https://doi.org/10.1109/TCOM.1982.1095577)
- Cash, W. 2011, The Astrophysical Journal, 738, 76, doi: [10.1088/0004-637X/738/1/76](https://doi.org/10.1088/0004-637X/738/1/76)
- Cover, T., & Thomas, J. 1991, Elements of Information Theory (New York: John Wiley and Sons), doi: [10.1002/047174882X](https://doi.org/10.1002/047174882X)
- Dolinar, S., Erkmen, B., Moision, B., Birnbaum, K., & Divsalar, D. 2012a, in IEEE International Symposium on Information Theory Proceedings (IEEE), 541–545, doi: [10.1109/ISIT.2012.6284249](https://doi.org/10.1109/ISIT.2012.6284249)
- Dolinar, S., Moision, B., & Erkmen, B. 2012b, Fundamentals of free-space optical communication, Jet Propulsion Laboratory, <http://hdl.handle.net/2014/42559>
- Farr, W. H., Choi, J. M., & Moision, B. 2013, in Free-Space Laser Communication and Atmospheric Propagation XXV, Vol. 8610 (International Society for Optics and Photonics), 861006, doi: [10.1117/12.2007000](https://doi.org/10.1117/12.2007000)
- Forgan, D., Heller, R., & Hippke, M. 2017, Monthly Notices of the Royal Astronomical Society, 474, 3212, doi: [10.1093/mnras/stx2834](https://doi.org/10.1093/mnras/stx2834)
- Forward, R. 1962, Missiles and Rockets, 10, 26
- Fountain, G., Kusnierkiewicz, D., Hersman, C., et al. 2009, The New Horizons spacecraft, New Horizons (Springer), 23–47, doi: [10.1007/s11214-008-9374-8](https://doi.org/10.1007/s11214-008-9374-8)
- Gallager, R. G. 2008, Principles of digital communication (Cambridge, UK: Cambridge University Press), doi: [10.1017/CBO9780511813498](https://doi.org/10.1017/CBO9780511813498)
- Gordon, J. 1962, Proceedings of the IRE, 50, 1898, doi: [10.1109/JRPROC.1962.288169](https://doi.org/10.1109/JRPROC.1962.288169)
- Gros, C. 2017, Journal of Physics Communications, 1, 045007, doi: [10.1088/2399-6528/aa927e](https://doi.org/10.1088/2399-6528/aa927e)
- Guha, S. 2011, Physical Review Letters, 106, 240502, doi: [10.1103/PhysRevLett.106.240502](https://doi.org/10.1103/PhysRevLett.106.240502)
- Hauser, M., Arendt, R. G., Kelsall, T., et al. 1998, The Astrophysical Journal, 508, 25, doi: [10.1086/306379](https://doi.org/10.1086/306379)
- Heller, R. 2017, Monthly Notices of the Royal Astronomical Society, 470, 3664, doi: [10.1093/mnras/stx1493](https://doi.org/10.1093/mnras/stx1493)
- Heller, R., & Hippke, M. 2017, The Astrophysical Journal Letters, 835, L32, doi: [10.3847/2041-8213/835/2/L32](https://doi.org/10.3847/2041-8213/835/2/L32)
- Heller, R., Hippke, M., & Kervella, P. 2017, The Astronomical Journal, 154, 115, doi: [10.3847/1538-3881/aa813f](https://doi.org/10.3847/1538-3881/aa813f)
- Hemmati, H. 2009, Near-earth laser communications (CRC press), doi: [10.1201/9781420015447](https://doi.org/10.1201/9781420015447)
- Hippke, M. 2017, arXiv preprint arXiv:1712.05682
- . 2018, arXiv preprint arXiv:1801.06218
- . 2019, International Journal of Astrobiology, 18, 267, doi: [10.1017/S1473550417000507](https://doi.org/10.1017/S1473550417000507)
- Hoang, T. 2017, The Astrophysical Journal, 847, 77, doi: [10.3847/1538-4357/aa88a7](https://doi.org/10.3847/1538-4357/aa88a7)

- Hoang, T., Lazarian, A., Burkhart, B., & Loeb, A. 2017, *The Astrophysical Journal*, 837, 5, doi: [10.3847/1538-4357/aa5da6](https://doi.org/10.3847/1538-4357/aa5da6)
- Hoang, T., & Loeb, A. 2017, *The Astrophysical Journal*, 848, 31, doi: [10.3847/1538-4357/aa8c73](https://doi.org/10.3847/1538-4357/aa8c73)
- Holevo, A. S. 1998, *IEEE Transactions on Information Theory*, 44, 269, doi: [10.1109/18.651037](https://doi.org/10.1109/18.651037)
- Jarzyna, M., Zwolinski, W., & Banaszek, K. 2019, in *International Conference on Space Optics*, Vol. 11180, International Society for Optics and Photonics, doi: [10.1117/12.2536130](https://doi.org/10.1117/12.2536130)
- Jarzyna, M., Zwoliński, W., Jachura, M., & Banaszek, K. 2018, in *Free-Space Laser Communication and Atmospheric Propagation XXX*, Vol. 10524, International Society for Optics and Photonics, 105240A, doi: [10.1117/12.2289653](https://doi.org/10.1117/12.2289653)
- Kafka, J., & Baer, T. 1987, *Optics letters*, 12, 401, doi: [10.1364/OL.12.000401](https://doi.org/10.1364/OL.12.000401)
- Kulkarni, N., Lubin, P., & Zhang, Q. 2018, *The Astronomical Journal*, 155, 155, doi: [10.3847/1538-3881/aaafd2](https://doi.org/10.3847/1538-3881/aaafd2)
- Landis, G. 2019, in *Tennessee Valley Interstellar Symposium*, Wichita, KN. <https://ntrs.nasa.gov/search.jsp?R=20190033432>
- Lewandowski, W., Azoubib, J., & Klepczynski, W. 1999, *Proceedings of the IEEE*, 87, 163, doi: [10.1109/5.736348](https://doi.org/10.1109/5.736348)
- Lubin, P. 2016, *Journal of the British Interplanetary Society*, 69
- . 2020, *The Path* (World Scientific)
- Ludwig, R., & Taylor, J. 2016, *Voyager telecommunications* (John Wiley and Sons, Inc), doi: [10.1002/9781119169079.ch3](https://doi.org/10.1002/9781119169079.ch3)
- Macleod, A. 2004, arXiv preprint arXiv:physics/0407077
- Manchester, Z., & Loeb, A. 2017, *The Astrophysical Journal Letters*, 837, L20
- Messerschmitt, D. 2020, BPPM modeling software, 1.0, Zenodo, doi: [10.5281/zenodo.3831502](https://doi.org/10.5281/zenodo.3831502)
- Messerschmitt, D., Lubin, P., & Morrison, I. 2019, arXiv preprint arXiv:2001.09987
- Messerschmitt, D. G. 2008, *Some Digital Communication Fundamentals for Physicists and Others*, Tech. Rep. UCB/EECS-2008-78, EECS Department, University of California, Berkeley. www2.eecs.berkeley.edu/Pubs/TechRpts/2008/EECS-2008-78.pdf
- . 2013, arXiv preprint arXiv:1305.4684
- . 2015, *Acta Astronautica*, 107, 20, doi: [10.1016/j.actaastro.2014.11.007](https://doi.org/10.1016/j.actaastro.2014.11.007)
- . 2017, *Proc. IEEE*, 105, 1511, doi: [10.1109/JPROC.2017.2717980](https://doi.org/10.1109/JPROC.2017.2717980)
- Moision, B., & Farr, W. 2014, *Range dependence of the optical communications channel*, Tech. Rep. 42-199, NASA IPN. tmo.jpl.nasa.gov/progress_report/42-199/199B.pdf
- Parkin, K. 2018, *Acta Astronautica*, 152, doi: [10.1016/j.actaastro.2018.08.035](https://doi.org/10.1016/j.actaastro.2018.08.035)
- . 2019, arXiv preprint arXiv:2005.08940
- Roh, W., Seol, J.-Y., Park, J., et al. 2014, *IEEE Communications Magazine*, 52, 106, doi: [10.1109/MCOM.2014.6736750](https://doi.org/10.1109/MCOM.2014.6736750)
- Schelkunoff, S., & Friis, H. 1952, *Antennas: theory and practice*, Vol. 639 (Wiley)
- Shibata, H., Shimizu, K., Takesue, H., & Tokura, Y. 2015, *Optics Letters*, 40, 3428, doi: [10.1364/OL.40.003428](https://doi.org/10.1364/OL.40.003428)
- Slepian, D., & Pollak, H. 1961, *Bell System Technical Journal*, 40, 43, doi: [10.1002/j.1538-7305.1961.tb03976.x](https://doi.org/10.1002/j.1538-7305.1961.tb03976.x)
- Smith, B. A., Soderblom, L. A., Banfield, D., et al. 1989, *Science*, 246, 1422, doi: [10.1126/science.246.4936.1422](https://doi.org/10.1126/science.246.4936.1422)
- Spencer, D. T., Bauters, J. F., Heck, M. J., & Bowers, J. E. 2014, *Optica*, 1, 153, doi: [10.1364/OPTICA.1.000153](https://doi.org/10.1364/OPTICA.1.000153)
- Spencer, D. T., Tang, Y., Bauters, J. F., Heck, M. J., & Bowers, J. E. 2012, in *Photonics Conference (IPC), 2012 IEEE (IEEE)*, 141–142, doi: [10.1109/IPCon.2012.6358529](https://doi.org/10.1109/IPCon.2012.6358529)
- Toyoshima, M., Leeb, W., Kunimori, H., & Takano, T. 2007, *Optical engineering*, 46, 015003, doi: [10.1117/1.2432881](https://doi.org/10.1117/1.2432881)
- Traub, W. A., & Oppenheimer, B. R. 2010, *Direct imaging of exoplanets*, ed. S. Seager, *Exoplanets* (University of Arizona Press), 111–156
- Treacy, E. 1969, *IEEE Journal of Quantum Electronics*, 5, 454, doi: [10.1109/JQE.1969.1076303](https://doi.org/10.1109/JQE.1969.1076303)
- Wicker, S. B., & Bhargava, V. K. 1999, *Reed-Solomon codes and their applications* (John Wiley and Sons)
- Wikipedia contributors. 2019, *Sunshine duration* — Wikipedia, The Free Encyclopedia. en.wikipedia.org/wiki/Sunshine_duration
- Wilson, T. L., Rohlfs, K., & Huttemeister, S. 2009, *Tools of radio astronomy*, Vol. 5 (Springer), doi: [10.1007/978-3-540-85122-6](https://doi.org/10.1007/978-3-540-85122-6)
- Wyner, A. 1988, *IEEE Transactions on Information Theory*, 34, 1449, doi: [10.1109/18.21284](https://doi.org/10.1109/18.21284)